DESIGN, SYNTHESIS, CHARACTERIZATION AND APPLICATION OF RARE-EARTH DOPED GLASS AND GLASS CERAMIC SCINTILLATORS

A Dissertation
Presented to
The Academic Faculty

by

Christian Struebing

In Partial Fulfillment
of the Requirements for the Degree of
Doctor of Philosophy in the
School of Materials Science & Engineering

Georgia Institute of Technology
December 2019

DESIGN, SYNTHESIS, CHARACTERIZATION AND APPLICATION OF RARE-EARTH DOPED GLASS AND GLASS CERAMIC SCINTILLATORS

Approved by:

Dr. Zhitao Kang, Advisor
Georgia Tech Research Institute
Georgia Institute of Technology

Dr. Zhiqun Lin
School of Materials Science & Engineering
Georgia Institute of Technology

Dr. Christopher Summers
School of Materials Science & Engineering
Georgia Institute of Technology

Dr. Brent Wagner
Georgia Tech Research Institute
Georgia Institute of Technology

Dr. Jason Nadler
Georgia Tech Research Institute
Georgia Institute of Technology

Date Approved: [November 07, 2019]

Dedicated to my supportive parents who have supported me along this way

ACKNOWLEDGEMENTS

First of all I would like to express my deep gratitude to my advisors Dr. Zhitao Kang and Dr. Christopher Summers. Their leadership through my foray into the world of materials science and engineering was exceedingly invaluable and the push they provided to guide me through to the completion of this degree was of great help. In addition I would like to extend this gratitude to my committee members Dr. Jason Nadler, Dr. Brent Wagner, and Dr. Zhiqun Lin for the use of their time through the proposal and defense process and the advice offered throughout.

I am also thankful for the other members of the lab and collaborators of GTRI. Dr. Eric Lee, Dr. Bernd Kahn, Brooke Beckert, and Sarah Lombadro were of great help in getting my footing in my research and fostering curiosity and support in approaching new ideas. I would like to further extend this towards my other collaborators Dr. Henry la Pierre, JooYun Chong, Martin Zavala, Dr. Anna Erickson, Dr. Yong Ding, Dr. Cai-Lin Wang, Dr. Yacouba Diawara, and Dr. Ralf Engels without whose input I would not be where I am today.

Finally I would like to extend my gratitude to my friends and my parents Joan and Jeffrey Struebing without whose support I would not have had the chance to achieve this or the resolve to see it through.

TABLE OF CONTENTS

LIST OF TABLES

LIST OF FIGURES

LIST OF SYMBOLS AND ABBREVIATIONS

PMT	Photomultiplier Tube
CCD	Charge-Coupled Device
e	Euler's Constant
keV	Kiloelectron-Volt
MeV	Megaelectron-Volt
FWHM	Full-Width at Half-Maximum
UV-Vis	Ultraviolet to Visible Spectrum
GS20	Commercial Glass Neutron Scintillator
LED	Light Emitting Device
MCA	Multichannel Analyzer
N	Neutron
n	Refractive Index
λ	Wavelength
kV	Kilovolt

ph	Photon
PL	Photoluminescence
PLE	Photoluminescence Excitation
TEM	Transmission Electron Microscopy
UV	Ultraviolet
W	Watt
Ci	Curie
XRD	X-Ray Diffraction
LSO	$LuSiO_5$
BGO	Bismuth Germanate
SAED	Scanning Area Electron Diffraction
BTG	Bismuth Titanium Germanate
BTGx	BTG with xGe Content
ZBLAN	53Zr-20Ba-4La-3Al-20Na
PSL	Photostimulated Luminescence

HRTEM	High-resolution Transmission Electron Microscopy
HREM	High-resolution Electron Microscopy
FCZ	Fluorochlorozirconate
FFT	Fast Fourier Transform
FBZ	Fluorobromozirconate
CaBZAKS	$CaO-B_2O_3-ZnO-Al_2O_3-K_2O-SiO_2$
LCASOF	Lithium-Calcium Aluminosilicate Oxyfluoride
LLASOF	Lithium-Lanthanum Aluminosilicate Oxyfluoride
IQI-301	Commercial Scintillating Glass
DSC	Differential-Scanning Calorimetry
ms	Millisecond
nm	Nanometer
LBGT	Terbium-doped Lanthanum Borogermanate

GBGT	Terbium-doped Gadolinium Borogermanate
EDS	Energy-Dispersive X-ray Spectroscopy
JACS	Journal of the American Ceramic Society

SUMMARY

Single crystal scintillators have been the premier choice for gamma ray detecting applications due to their high luminescent efficiency and sharp energy resolutions. However, there remain downsides to the use of single crystal scintillators. The production method for such materials is often time-consuming and the precursor materials required can be costly. Additionally, the end product often suffers from vulnerability to mechanical shock, high temperatures, and atmospheric moisture requiring additional sealing and shielding countermeasures which increase expense and add to the bulk of the completed detector. Industries have been searching for lower cost alternatives to single crystal scintillators in order to make more portable devices practical.

Glass and glass-ceramic scintillators have gained attention for their lower production cost, scalability, and ease of shaping to fit complex geometries. By the nature of the glass matrix any crystalline phases within the material are self-encapsulated, which avoids the issue of hygroscopicity and reduces the impact of mechanical shock and high temperature exposure. The main issue holding back glass and glass-ceramic scintillators has been the low luminescent efficiency stemming from the inherent disorder in the non-crystalline glassy matrix. We believe this downside can be mitigated through increases to density, harnessing the innate energy transfer capabilities of constituent materials, and controlled nucleation of crystalline phases within the glass structure.

Glass-ceramics combine the robust resilience of glass with the luminescent capabilities of crystalline nanoparticles by precipitating nano-sized crystals within the glass matrix. This study approaches the field of glass and glass-ceramic based scintillators with

rare-earth rich, high density compositions modeled after known crystal systems in order to produce a glass ceramic scintillator that could compete with single crystals.

CHAPTER 1. INTRODUCTION

1.1 Scintillators

A scintillator is a type of material that has the capability to absorb the energy of incoming ionizing radiation and emit visible light photons in response through the excitation and relaxation of electrons in dopant activator ions. Currently single crystals are the primary choice for scintillators due to their high luminosity, efficiency, and fine energy resolution. Among these NaI:Tl single crystals are among the most widely utilized in gamma ray detection applications as they can operate at ambient temperatures and can be manufactured at relatively large sizes. However, single crystal scintillators are not without drawbacks. Iodide and bromide based single crystals tend to be hygroscopic which requires they be hermetically sealed to protect from atmospheric moisture which increases the size of the detector through the shielding and increases production cost. Many other inorganic single crystals suffer from low production sizes, narrow application viability, and vulnerability to heat, mechanical shock, and electrical shock. Organic polymer scintillators can be produced in much larger sizes and volumes than single crystals and have been employed in applications such as truck portal detectors, but lack the ability to adequately discriminate and identify the detected radioactive source material.

Due to the relatively high cost of these single crystal scintillation materials there has been interest in developing and producing lower cost, but still comparatively efficient scintillators. Glass and glass-ceramic materials can be produced for as little as $\$1/cm^3$ which is a fraction of the cost of single crystals. Glass and glass-ceramic materials do not suffer from the vulnerability to physical and electrical shock as severely as single crystals

and the self-sealing capabilities of the glass matrix protects against hygroscopic issues without additional shielding. The glass and glass-ceramic materials previously developed have fallen short on the luminescent efficiency, light yield, and energy resolution compared to single crystals. It is the goal of this work to utilize materials engineering to improve these features of glass and glass-ceramic scintillators to offer lower cost alternatives for detection applications.

1.1.1 Scintillator Application

The basis of many high energy detection systems begins with scintillator material coupled to a light collection device such as a photomultiplier tube (PMT) or charged-coupled device (CCD) to convert the emitted visible light photons to electrical signals which are used to develop pulse height emission spectra. A basic schematic of such a detection setup is depicted in Figure 1: Coupling of scintillator material to PMT as the basis unit of detection systems. below. Recently, the Department of Homeland Security has had an interest in the improvement of portable and cost-effective nuclear detection capabilities for more effective inspection coverage of shipping containers. In other considerations there is an impending ^{3}He shortage which is the current standard for use in neutron detection arrays as a gas scintillator. This shortage necessitates the development of alternative neutron detection systems which could also assist in the detection of materials such as plutonium. (1) (2) (3) (4) In the field of medical imaging scintillators are used extensively coupled with photodiodes, CCDs, and PMTs in order to detect X-rays for many X-ray imaging methods, which could benefit from the cost reduction of sufficiently powerful glass or glass ceramic scintillators to replace single crystals. (5) (6)

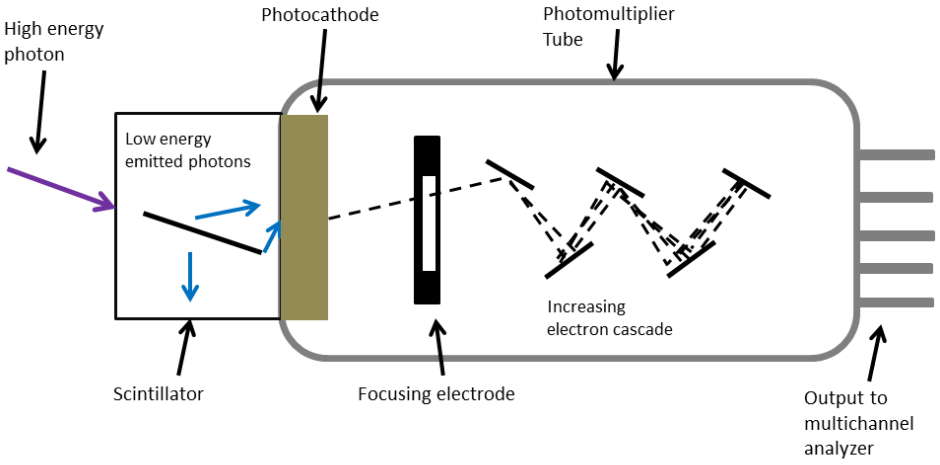

Figure 1: Coupling of scintillator material to PMT as the basis unit of detection systems.

1.1.2 History of Glass and Glass-Ceramic Scintillators

Glass scintillators have been investigated for decades for use in applications such as neutron detectors, glass fiber optics, and large-scale low-cost detectors. (7) (8) (9) (10) (11) Glass scintillators can be prepared in large melt batches that do not require stringent directional control and take a matter of hours to fully finish the synthesis and cooling process which allows for the possibility of high volume production. Glasses can be produced in a variety of shapes through the use of different casting molds as well as allowing for the production of fibers which has kept them in great interest. (12) (13) Finally glass materials boast high thermal and mechanical resistance compared to the crystalline materials which has generated interest in research for applications requiring robust detectors. (12) When compared to plastic scintillators which boast similar volume

production capabilities glass scintillators offer higher densities which leads to better gamma ray detection capabilities. Glass materials can be used as the basis for the production of glass-ceramics through the application of additional heat treatments after the solid transparent glass is obtained. The term glass is used to describe these initial materials as they are prepared in such a manner to capture the structure of the material in the chaotic, amorphous, disordered state that can occur when a molten material is swiftly cooled to a target glass formation temperature. When performed in a short enough time frame the material does not have the time to order itself in more crystalline arrangements as would be energetically preferred and the atoms and molecules of the composition are captured in a random arrangement as the previous high-energy state of heating would cause. As a result, with applied additional energy through heating the atoms within the material gain enough mobility to locally orient within the glassy matrix and form crystalline particles of small size around nucleation sites. The temperature at which this crystallization will occur is dependent on the composition of the glass and the crystalline phase targeted. The temperature of crystallization can be determined directly through analysis techniques such as DSC, or indirectly through visual inspection of the material for development of large scale crystalline phase and then confirmed through XRD analysis. In general for glassy materials analysis through DSC presents an exothermic peak at the temperature of crystallization. As this crystallization action presents as an exothermic process, releasing energy instead of requiring additional energy input, this indicates that the crystallized form of the material is more energetically favourable arrangement and this crystallization will begin spontaneously when the environmental conditions allow. As a result, this crystallization can be easily triggered by raising the temperature of the material to this

critical crystallization temperature or above to provide the necessary atomic mobility for the material to orient as small crystalline regions. This crystallization stands to improve the efficiency of glass scintillators as the probability of radiative recombination is typically larger in more ordered structures than the amorphous structure of the glass matrix. (14) (15) (16)

Glass-ceramics containing nanocrystals of compositions such as PbF_2, LaF_3, GdF_3, BaF_2, $BaCl_2$, and CaF_2 have been well investigated in previous years. (17) (18) (19) (20) (21) (22) (23) However, many of these glass-ceramics were originally investigated through the lens of other applications such as upconversion solid state lasers, optical amplifiers, and white LEDs. (24) (25) (26) (27) As such the use of glass-ceramic scintillators for gamma ray detection applications has not been thoroughly explored. Reported light yields of recent glass ceramics such as 6300 ph/MeV and 7200 ph/MeV from Voronchikhina et al. and Kobayashi et al. respectively still leave much to be desired in the realm of gamma ray detection. (20) (28) In addition, the sizes of these scintillators were not fully disclosed and reports of energy resolution and gamma responses are not included, leaving us with an incomplete picture of the viability of these materials. With further refinement of the performance of glass and glass-ceramic scintillators they could open up an avenue of competition with single crystal scintillators at reduced cost. In addition, the population of light yield, gamma spectra, and energy resolution reports for investigated glass and glass-ceramic scintillators will pave the way for future development of such systems and present value to the wider field of glass and glass-ceramic scintillators.

1.1.3 Scintillator Properties

The objective of this research is to design glass and glass-ceramic compositions for the production of efficient scintillator systems and to iterate on and optimize those compositions for detection applications. In order to markedly improve the performance of glass and glass-ceramic scintillators through the lens of materials science and engineering we must understand the key characteristic features that are desired of scintillators for use in detection applications and the material properties that influence them.

1.1.3.1 Light Yield

Of foremost concern is the light yield of the material. Since the defining characterstic of a scintillator is its ability to emit light in response to incoming radiation it is of utmost concern that the material produces as many photons as possible, as efficiently as possible from the excitation energy provided through the absorption of incoming radiation. Additionally, higher light yields provide larger signals for the PMT to detect and greater peak separation which allows for easier differentiation between the signatures of different radionuclides. The light yield of a scintillator has several complex avenues for improvement which can make definitive composition design difficult. Light yield can be improved directly through the improvement of factors that govern the energy obtained from incoming radiation such as the density and stopping power of the material and the innate efficiency of the chosen dopant ion. Light yield can also be improved through factors that look to improve the efficiency of the conversion of gamma energy to visible light photons such as quantum cutting effects and increased dopant load. These factors of light yield are complex and shall be investigated individually.

1.1.3.2 Energy Resolution

The energy resolution of a scintillator is a performance based characteristic, but is ultimately the most important factor of scintillators for finding use in radiation detection applications. The energy resolution of a scintillator is a measure of the light yield in the full energy photopeak of the scintillator response compared against the width of the produced photopeak. The energy resolution is a key factor in the ability of radiation detection systems to successfully discriminate and identify the signature scintillator responses for different radionuclides. An example gamma radiation response spectrum is provided in Figure 2: Example of spectroscopic properties of the radiation excitation response of scintillators. The identified regions are of particular interest when gauging the radiation excited response of scintillators and include the Compton continuum, the position of the full energy photopeak, and the full-width at half-maximum (FWHM) of the full energy photopeak. For gamma radiation one of the primary methods of interacting with matter is through Compton scattering. Compton Scattering is the phenomenon by which inelastic collisions occur between an incident gamma ray photon and an atomic electron wherein a significant portion of the energy of the gamma ray is transferred causing the ejection of the electron and leading to the emission of a lower energy gamma ray photon in a direction different than the incident ray path. (29) As this occurs the gradual loss of energy of the incident ray and successive rays will eventually reach the proper energy level to allow for the excitation of the atomic electrons without ejection at which point visible light photon production can occur in the scintillator. However, at each of these interaction points there is a possibility that the incident or additional “scattered” rays prematurely escape the material and as such do not contribute their full energy to photon production.

The Compton continuum is the broad range near the lower channel number and lower energy range of the gamma excited pulse height spectrum that indicates these cases of which radiation photons impact the scintillator, but are not fully stopped and the energy of those photons is not fully absorbed. As a result this amount of absorbed energy does not contribute to the full energy photopeak and is in essence wasted as far as the accurate detection of radionuclides is concerned. The main goal of compositional design in regards to the Compton continuum is to minimize the amount of energy wasted in that region. This is typically quantified through the ratio of the full energy photopeak height to the height of the Compton continuum, with the goal being to enhance this ratio. To accomplish this, the density and Z number content of the material should be maximized to generate maximum gamma ray stopping power. The peak position in terms of channel number presents an indirect look at the amount of light emitted in response to gamma excitation. This factor is introduced in the calculation of the energy resolution as an indicator of the total light yield that presents in a useful energy range for detection. The FWHM comes into play as a measure of the homogeneity of the material and its emission of light in response to excitation. The narrower the full energy photopeak is, the more useful it will be for discrimination of different radiation sources. As different radioactive materials each undergo a unique decay mechanism to produce radiation, each source will produce gamma ray photons of different energies. When these gamma ray photons interact with a scintillator they can only transfer as much energy as they initially contain. With a single scintillator, as long as the energy of the absorbed gamma ray exceeds the necessary threshold to induce the excitation of the valence electrons in the dopant ion, the energy of the emitted visible light photon will remain largely the same. As a result, gamma ray

photons of different energies will induce the production of a different number of visible light photons from the scintillator which will result in full energy photopeaks with different peak positions. In order to accurately identify these different radiation sources the scintillator response peaks must remain narrow enough so they do not excessively overlap. The FWHM features in the calculation of the energy resolution of the scintillator as a measure of the sharpness of the photopeak as shown in Equation 1. (30) The energy resolution is determined by dividing the FWHM of the full energy photopeak by the photopeak position, measured either by channel number or energy in keV. The energy resolution for many single crystal materials can be as low as single digit percents, which allows for detection system software to easily discriminate and identify different radiation sources. In order for a glass or glass-ceramic scintillator to compete with single crystals the energy resolution would have to be under 10% to provide a similar level of accuracy when incorporated into a radiation detection system.

$$Energy\ Resolution = \frac{FWHM}{Peak\ Position} \text{x} 100 \quad (1)$$

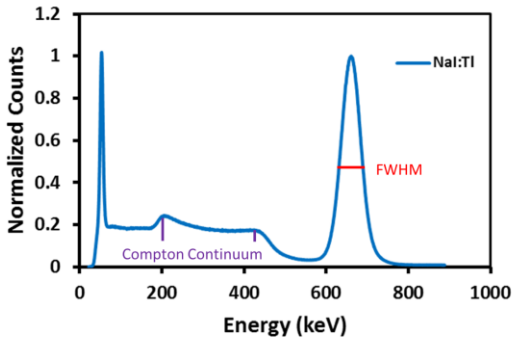

Figure 2: Example of spectroscopic properties of the radiation excitation response of scintillators.

1.1.3.3 Transparency

The transparency of the light emitting scintillator is nearly as important as the light yield itself. Since radiation detection systems ultimately work by detecting the emitted visible light photons from the scintillator the material must be transparent in order to allow the emitted light to escape the scintillator and interact with the PMT. With this in mind we cannot look to improve the light yield of a scintillator at the expense of transparency. The transparency of glass and glass-ceramic materials is a result of several factors such as the chemical composition, volume percentage of nanocrystals, nanocrystal structure, and nanocrystal size. Transparency can be determined qualitatively via visual inspection as well as quantitatively via UV-Vis transmission spectra. To avoid light scattering the nanocrystalline particles nucleated within the glass matrix must remain below the critical size of interest to satisfy two different requirements. The first requirement involves scattering elements that are widely separate which obey the Rayleigh-Gans model. (31) This model depicts the attenuation due to scattering, σ_p, as follows:

$$\sigma p \approx \left(\frac{2}{3}\right) * (NVk^4 * a^3 * [n\Delta n]^2) \quad (2)$$

where N is the particle number density, V is the particle volume, a is the particle radius, $k = 2\pi/\lambda$ where λ is the wavelength, n is the refractive index of the crystalline phase, and Δn is the refractive index difference between the crystalline phase and the host glass matrix. The second requirement concerns scattering elements that are more closely spaced where the separation between them is between the size of the particle radius and up to 6 times that size. A model describing behaviour under these conditions was developed independently by Andreev and Hopper which presents the turbidity of the material as:

$$\sigma c \approx \left[\left(\frac{2}{3} * 10^{-3}\right) k^4 \theta^3\right] (n\Delta n)^2 \quad (3)$$

Where θ is the mean phase width (a+W/2), W is the inter-particle spacing, and the remaining terms as defined previously above. (31) (32) (33) In practical terms these conditions dictate that the incorporated crystalline particles remain roughly 1/5 the size of the wavelength of interest. (34)

As many scintillators make use of rare-earth dopants that emit in the visible light range typically between 300nm and 600nm these conditions require that the crystalline particles remain in the nano-scale region in size. The size of the grown nanocrystalline phase can be controlled through the control of the nucleation temperature and time period of heat treatment processes as well as through incorporation of nucleating agents such as TiO_2 and ZrO_2 which are relatively easy to control directly and offer a straightforward approach. (31) (34) The refractive index and refractive index mismatch of the glass and nanocrystals contributes to the transparency of the material as well as seen above. Crystals that possess an anisotropic crystal structure present difficulty for growth beyond the aforementioned size limitation as the directional dependence of the refractive index will cause the material to scatter in a different manner depending on the relative direction between the crystal and the matrix. However, for crystalline phases that possess an isotropic crystal structure the scattering behaviour will remain the same no matter the relative orientation of the crystal and glass matrix. As a result, the glass matrix system could be designed such that the refractive index of the glass matrix matches the refractive index of the nanocrystals which will minimize the scattering due to refractive index mismatch and could potentially allow for the growth of greater volume fractions and larger

sizes of the crystalline phase without additional scattering. (35) (36) This approach to the minimization of scattering is more difficult to achieve, but can be pursued through design of a composition that will form a stable glass while possessing a similar stoichiometry to that of the desired crystalline phase such as with $Ba_2TiSi_2O_8$ based glasses nucleating a 71% volume fraction of $Ba_2TiSi_2O_8$ nanocrystals and a $KNbGeO_5$ glass obtaining an 80% volume fraction of $K_{3.8}Nb_5Ge_3O_{20.4}$ phase. (35) (36) (37) (38) (39) (40)

1.1.3.4 Stopping Power

In order for the scintillator to emit light it must first absorb energy from the incoming gamma radiation. Due to the incredibly strong matter penetration capabilities of gamma radiation the material must have a high gamma ray stopping power in order to accomplish this. The stopping power of a material is heavily dependent on the thickness of the material and its chemical composition in terms of both material density and the incorporation of high Z number elements. As the thickness of the utilized scintillator can be controlled directly through production of larger batches or through stacking multiple pieces of material together the improvement of stopping power in the material through compositional design is of greater interest. In addition, by improving the innate stopping power of the material and reducing the thickness required to fully absorb the radiation the production cost and size of the overall detection system can be kept lower keeping in line with the lower cost scintillator goals already discussed. By including high levels of rare-earths and heavy metals in the precursor materials such as gadolinium we can contribute to both factors of the stopping power.

For neutron detection applications the goals for stopping power are reversed. As the detection of neutrons relies on specific sensitizer reactions that lead to the internal emission of additional charged ions and photons that excite the material in a similar manner as typical scintillation. As a result a low density material is desired to reduce the sensitivity to extraneous gamma, alpha, and beta sources which can cause noise in the spectrum while having a large neutron sensitivity cross-section through the incorporation of neutron sensitive materials.

1.1.3.5 Emission Wavelength

The wavelength of the visible light emission is important to keep in mind for design decisions in constructing the overall detector. Since the wavelength of the emission is almost entirely dependent on the choice of dopant ion it is much simpler to control directly, but still plays a factor in the design of the planed crystalline phase as some dopant ions cannot substitute into certain crystalline structures. Depending on the application of the detector different wavelengths of emitted light are more desirable. Detection systems utilizing PMTs tend to be more sensitive to UV-blue light emissions, where dopants such as Ce^{3+} and Eu^{2+} perform well. Systems using CCDs are more sensitive to red light around the 600nm wavelength which provide use for dopants such as Eu^{3+}. Dopants with emissions between these ranges such as Tb^{3+} are less useful for these applications, but can still find use for applications like X-ray and MeV imaging. While the emission wavelength primarily depends on the chosen dopant element and valence the coordination of the dopant ion within the glass matrix and crystalline phase can lead to slight shifts in the wavelength of the emission, especially for dopants such as Ce^{3+} that possess weaker electron shielding.

1.1.3.6 Decay Time

The decay time for the luminescent emission of a scintillator is the duration required for the number of excited particles, or the intensity of their emission, to reach a value of 1/e of the initial amount or intensity when first excited by the ionizing radiation. The speed at which the material de-excites impacts its ability to accurately detect frequent pulses of incoming radiation. If the decay time of the scintillator is too slow it runs the risk of multiple incoming radiation pulses overlapping in the resultant PMT signal which then can cause difficulty in identifying the type and amount of the radioactive source material. Scintillators with faster decay times will produce clearer signals and are therefore more desirable. For the detection of gamma radiation a decay time in the nanosecond range is typically required. For X-ray and MeV imaging applications a fast decay time is still desired, but a slower decay time in the low ms range could still find use.

Certain aspects of the material structure can impact the decay time directly, but typically in ways that are less helpful for detection applications. Defect centers in the glass matrix can act as non-radiative recombination sites that will allow the material to de-excite very quickly. However, by de-exciting through non-radiative recombination no light is produced from those electron-hole pairs which leads to a lower light yield overall. In the other direction, additional energy transfer processes from sensitizers to the dopant ions will result in a higher light yield, but the non-direct excitation will result in a slower decay time. While these factors are not as useful for intentional development, they are helpful for the interpretation of observed changes in the decay time of scintillators during composition optimization and heat treatment analysis.

1.1.3.7 Radiation Hardness

The radiation hardness of a material is an indirect measure of how resilient the material is to repeated and chronic exposure to ionizing radiation. Continued exposure to radiation can cause defects in the material such as color centers which will negatively impact the performance of the scintillator through behaviors such as increased internal absorption, loss of transparency, and additional non-radiative recombination. (41) As such it is important that the designed scintillators have high radiation hardness to ensure the repeated replacement of the material does not undermine the initial cost reduction of the production of glass and glass-ceramic materials. Heavy metal oxides have been shown to contribute to high radiation hardness as well as doping with Ce^{3+}. (42) In the case of glass-ceramics it has been shown that materials with stoichiometric compositions matching those of known crystalline phases increases radiation hardness as well.

1.2 Scope of the Research

The motivation of this research was to investigate the improvement of the performance of glass and glass-ceramic scintillators through compositional design and post processing procedures. The controllable parameters of the synthesis experiments include the chemical composition of the scintillators, the heat treatment times, and the heat treatment temperatures that produce the glass ceramics. To this end several compositions were fabricated and then enhanced with the nucleation of crystalline phase nanoparticles where applicable.

As discussed above glass and glass-ceramic scintillators offer a novel approach to the newly developing desire for efficient, low-cost scintillators when compared to single

crystals. To adequately compete with single crystal scintillators the light output and energy resolution of glass and glass-ceramic scintillators must be greatly improved. The target for such an improvement in energy resolution is <10% with a light output as high as possible considering most single crystals output light at a level typically near 50,000 ph/MeV. (43)

The performance of the base glass matrix depends on certain characteristics of its composition. A low phonon energy environment is desirable to allow for greater radiative recombination along the glass matrix pathways while reducing the likelihood of non-radiative recombination. Designing a glass matrix with high density without sacrificing transparency also allows for a greater efficiency of energy absorption from the incoming radiation. The incorporation of fluoride and bromide precursors, which allow for retention of rare earth halides within the glass matrix was a point of focus for the promotion of a low-phonon energy environment, and are materials easily incorporated into many silicate and oxyfluoride glass systems. Incorporation of high density and high Z number rare-earth elements, particularly lanthanides such as La and Gd, has been the main point of interest in increasing the stopping power of these glass scintillator materials. There has also been demonstration of energy transfer capabilities between Gd^{3+} and activator ions within the glass matrix, which makes $GdBr_3$ an incredibly attractive precursor material.

The nucleation and growth of nanocrystals within a glass matrix to produce a glass-ceramic provides an additional axis of performance improvement outside of the raw compositional design. The crystalline structure of the nanocrystals naturally allows for more efficient energy transfer within the material than a purely amorphous glass. With dopant ions incorporated into this crystalline region they can benefit from additional energy exposure through local energy transfer as opposed to glass materials typically only gaining

excitation energy through direct excitation of the relatively low concentration dopant ions in the glass matrix. In order to achieve the greatest possible improvement through the growth of nanocrystals we look towards a glass matrix that can support as high of a volume fraction of nanocrystals as possible without compromising the transparency of the material. This approach can then take two separate paths: homogenous distribution of nanosize crystalline particles that will not induce scattering in the visible light spectrum; or production of a glass matrix with a refractive index that matches that of the crystalline phase thus negating scattering effects. In order for refractive index matching to be achievable both the glass matrix and the crystalline phase must be isotropic which requires a crystalline phase with a cubic crystal structure.

In Chapter 2 I present a review of the available literature regarding glass matrices investigated for use as the hosts of glass and glass-ceramic scintillator systems as well as the available crystalline systems that have been investigated as single crystals and as part of glass-ceramic scintillator systems. The materials reported are reviewed and compared for critical components of scintillator performance and analyzed to determine the most promising systems for development and potential improvement pathways to produce more efficient glass and glass-ceramic scintillators for detection applications.

In Chapter 3 I discuss the compositional design and production of a CaF_2:Eu^{2+}/^{6}LiF based glass-ceramic for potential use in neutron detection applications. This composition is designed in the style of the first approach of attempting to index match a glass matrix to the nucleated crystalline phase in order to allow for the potential growth of large volume fraction of crystalline phase nanoparticles. This chapter will also demonstrate the benefit

of the overall approach of the nucleation and growth of crystalline nanoparticles as a viable path for the improvement of the performance of glass based scintillation materials.

In Chapter 4 I discuss the design, production, and refinement of a $BaGdF_5$ based glass ceramic for use in gamma radiation detection applications. This composition takes into account the confirmation of performance improvement indicated from the results of the CaF_2 based glass ceramic and seeks to nucleate the cubic $BaGdF_5$ crystalline phase within an oxyfluoride glass matrix with high halide content for the encouragement of a low phonon energy environment to enhance the efficiency of the dopant. The $BaGdF_5$ crystal system is known to support Ce^{3+} doping which is of the most promising dopants for gamma applications due to the strong blue emission and fast decay time. This composition is also designed to incorporate a large quantity of the high Z number, high density, rare earth element Gd in order to improve the gamma ray stopping power of the scintillator and take advantage of the sensitizer qualities of Gd^{3+} for further performance improvement.

In Chapter 5 I discuss the design and production of two borogermanate based glasses with heavy lanthanide and rare earth element inclusion. These compositions are the first pass at the secondary compositional design approach discussed through production of glasses with stoichiometric compositions matching those of known crystal phases to harness the possibility of crystalline phase nucleation in addition to the benefit to radiation hardness such a stoichiometric composition provides. Even without the production of the nanocrystalline phase a glass composition based on the composition of a crystalline phase poses the possibility of harnessing some of the same benefits the crystal displays in terms of stopping power and transparency. The first composition investigated in this chapter is based on the $LaBGeO_5$ crystal phase composition which supports the use of the dopant

Tb^{3+}. The second composition investigated in this section is based on the $GdBGeO_5$ crystal phase composition, which offers similar benefits to the La based composition above with an additional benefit of greater density and innate energy transfer capabilities afforded by Gd.

In Chapter 6 I discuss the design and production of the final composition investigated in a $LiAlSiO_4$ based silicate glass. This composition seeks to combine the benefits of the stoichiometric crystal composition providing beneficial radiation hardness, LiF as a fluxing agent as well as a halide source for a low phonon energy environment, and the capability of this crystal phase composition to support Ce^{3+} doping which is one of the best dopant options for gamma ray applications due to its low wavelength emission range and fast decay times. This chapter also investigates the possibility of maximizing the gamma ray stopping power of the material through substitution of the original Al for the high density element Gd which has proven beneficial in the previous compositions. The Gd content is incorporated through a halide based precursor source to potentially benefit from further addition of low phonon energy halides to the glass matrix. Through this substitution we seek to greatly improve the density of the material, harness the energy transfer capabilities of Gd^{3+}, and further promote a low phonon energy environment through the use of $GdBr_3$ as the Gd precursor source. The concentration of the rare-earth dopant is also investigated in this section in order to maximize light output while avoiding concentration quenching.

In Chapter 7 I present a summary of the collective results of this study of the production and optimization of glass and glass-ceramic scintillators of the five compositions identified and investigated as promising scintillator options. The main design and optimization principles are reviewed and evaluated for their effectiveness and the produced

compositions reviewed for possible use in detection systems now or in the future. A look at additional factors to consider for future work in the field of glass and glass-ceramic synthesis of these investigated or similar compositions is also presented in order to assist the further innovation and growth of this field of materials science research.

1.3 Methods & Materials

1.3.1 Glass and Glass-Ceramic Design

Recent developments in glass and glass-ceramic scintillator design have been turing towards the addition of high density rare-earth material and crystalline nanoparticles to improve the light output and luminescent efficiency of the materials. The incorporation of the nanocrystalline phase can be accomplished primarily through two approaches: addition of preconstructed crystalline nanoparticles to the material during the melt phase of the synthesis; or the nucleation and growth of nanocrystals within the glass after the completion of the synthesis of the base glass. The addition of premade nanoparticles to the melt brings with it a variety of potential control issues to the production of the material such as exposure to open air during the high temperature melt phase which could induce oxidation of the dopant ions, thermal shock causing damage to the nanoparticles after being added to the mixture at melt temperature, and potential for inhomogenous distribution of the nanoparticles within the material which could cause loss of transparency and broadening in the FWHM of the full energy photopeaks. For the nucleation and growth of crystalline nanoparticles through post-processing heat treatment the composition of the precursor mixture must be considered more closely to provide adequate crystalline phase material and nucleation centers. However, once these considerations are satisfied it is much

easier to achieve stable, homogenous distribution of the crystalline phase nanoparticles. Due to these considerations it was decided to focus on the in situ nucleation and growth of nanocrystals in post-production. Through this method of inducing the nanocrystalline phase both approaches of maximizing crystalline benefit are undertaken: designing a glass matrix to index match a chosen crystal phase and designing a glass matrix with the same stoichiometric composition as a crystal system and controlling the size of the nucleated nanocrystals.

For applications in gamma ray detection the most important characteristics of scintillator performance are high material density, high light output, and fast luminescent decay time. These three characteristics will provide a glass or glass-ceramic material that can successfully stop high energy gamma rays, produce a detectable response signal with sufficient resolution to differentiate nuclides, and reset quickly enough to prevent signal overlap.

1.3.2 Glass and Glass-Ceramic Synthesis

Transparent glass scintillators of the aforementioned systems are prepared through the melt-quench method, a schematic of which is depicted in Figure 3: Melt-quench synthesis procedure for base glass scintillators. below. In this synthesis method the precursor material powders are combined, mixed to homogeneity, transferred to an alumina crucible, and loaded into a custom made furnace which is purged with inert Ar gas and loaded with additional excess graphite to combat oxidation. The furnace is then brought to the melting temperature and allowed to dwell until the melt stage is complete, typically on the order of 2.5 hours. Once the melt has completed the crucible is removed from the furnace and the

melt is swiftly poured into a graphite mold preheated to 400ºC to quench the molten mixture and obtain a clear glass. Following the quench the cast sample is annealed within a tube furnace for 6 hours at 500ºC in air to relieve internal stress. At this point the production of the glass scintillators is complete.

To reach the final stage of the glass-ceramic production the cast and annealed glass is put through an additional heat treatment to nucleate and grow the nanocrystalline phase by heating the material to just below the full crystallization temperature of the glass and holding it there for 6 hours after which it is allowed to return to room temperature. To confirm that the sought after nanocrystalline phase can successfully nucleate in the chosen base glass composition a preliminary series of heat treatments are performed with excess glass fragments harvested from the initial synthesis. These excess portions of glass are put through heat treatments at successively higher temperatures while observing the transparency of the material. Once the material begins to lose transparency it can be presumed to have produced some nanocrystalline particles that have grown large enough to reduce the transparency of the material. A note is made of the temperature at which transparency loss is observed as any later for-use nucleations will need to be performed below this temperature to maximize improvement while not compromising transparency. The heat treatments of the excess sample are then continued until it has been rendered fully opaque in order to maximize the crystalline volume fraction and increase the size of the XRD peaks so that the crystalline phase may be properly and accurately identified. After confirming the obtained crystalline phase is the desired phase the heat treatment temperature is fine-tuned to allow for maximum crystalline volume while maintaining transparency.

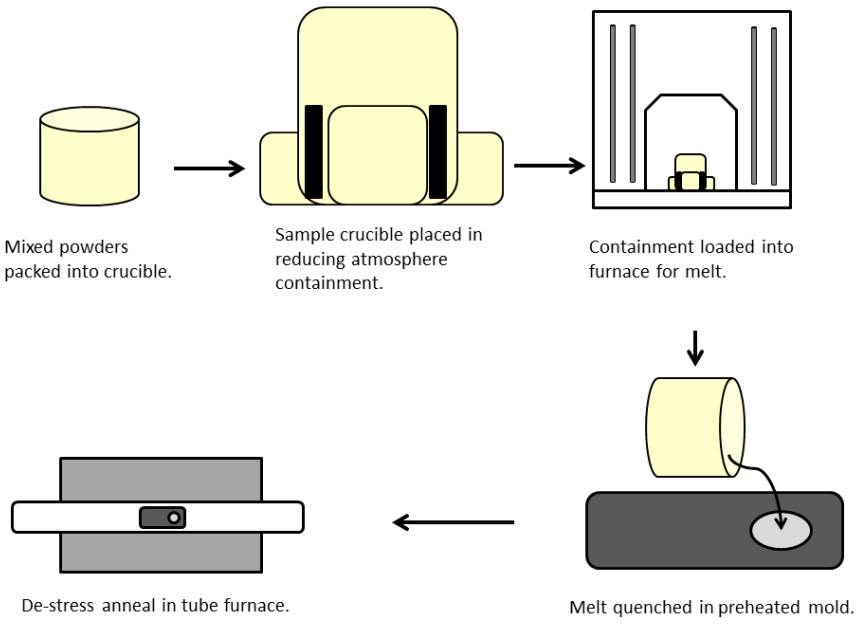

Figure 3: Melt-quench synthesis procedure for base glass scintillators.

1.3.3 Characterization Methods

In order to confirm the production of the desired glasses and glass-ceramics a variety of characterization methods are employed. In this subsection I will detail the methods utilized, the principles under which these methods operate, and the experimental parameters these methods were utilized with. Unless otherwise stated all characterization measurements were performed at room temperature.

1.3.3.1 Archimedes' Principle

The density of the material has been established as a critical feature of scintillators to enhance the stopping power of the material and allow for the successful absorption of

gamma ray energy. However, due to the slightly irregular shape of the produced glass ingots it is difficult to directly measure the volume of the glass and as a result difficult to find the density of the material directly. As such, the density of produced materials is confirmed through the application of Archimedes' principle in water. Archimedes' principle states that the buoyant force applied upwards against a submerged object is equal to the weight of the liquid that was displaced. A schematic of this principle is depicted in Figure 4: Schematic detailing Archimedes' Principle.. By filling a container with water, placing the container onto a scale, zeroing the scale, suspending the prepared glass ingot via near-massless fine string, submerging the suspended glass ingot, and noting the displayed mass we can find the volume of the displaced water due to water possessing a density of 1 g/cm^3. After determining the volume of the ingot the mass can be measured directly and used to calculate the density, ρ, through the typical mass-volume relationship:

$$\rho = \frac{m}{V} \quad (4)$$

Where m is the mass of the sample and V is the volume.

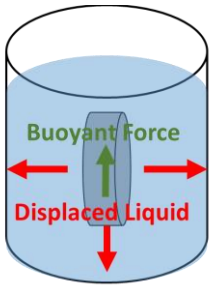

Figure 4: Schematic detailing Archimedes' Principle.

1.3.3.2 Photoluminescence and Photoluminescence Excitation

Light emission from the scintillator is the result of a photoluminescence mechanism. Photoluminescence in general is the emission of light from matter after the absorption of energy from incoming photons. The absorption of energy of the proper minimum energy level will excite the valence electrons of the material to a higher energy level, which will then naturally de-excite to return to its ground state and emit another photon as a result of the potential energy difference between the two energy levels. The wavelength of the emitted light depends on the material used and the available transition bands within said material. A schematic of this process is presented in Figure 5: Schematic of fluorescence photoluminescence response. below. Non-radiative recombination is the result of a transition between two energy levels where the difference in energy is insufficient to allow for the emission of a visible light photon. In the case of scintillators we wish to limit the frequency of non-radiative recombination as much as possible to preserve the amount of available energy for radiative recombination in the form of fluorescence. In order to determine the maximum emission wavelength of the produced glasses and glass-ceramics we employed a PL measurement system. To measure the PL of the materials a 150W Xe lamp/monochromator combination was utilized as the excitation source and the emitted light was collected with a Spex1000M spectrometer. A schematic of the experimental setup is provided in Figure 6: Schematic of utilized photoluminescence setup.. For measurements of the PL spectrum the detection wavelength is swept across a range of values while the excitation source wavelength is held constant to determine the maximum emission wavelength of the material. For measurements of the PLE spectrum the detection wavelength is held constant while the excitation source wavelength is swept across a range

to determine the maximum excitation wavelength. With these PL and PLE spectra we can confirm the luminescent response of the material to check for the desired valence of the incorporated dopant ion and inspect the result of interaction with the dopant ion energy levels from the surround glass matrix.

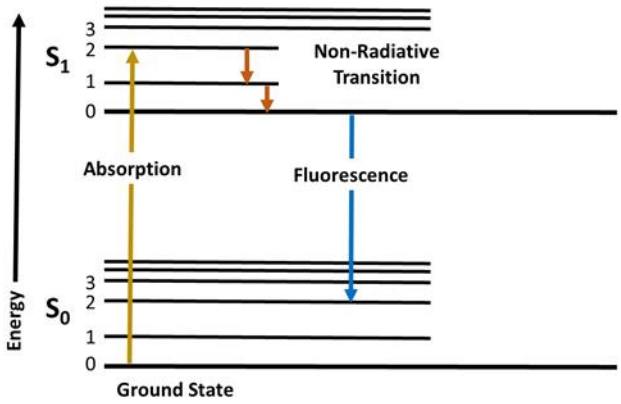

Figure 5: Schematic of fluorescence photoluminescence response.

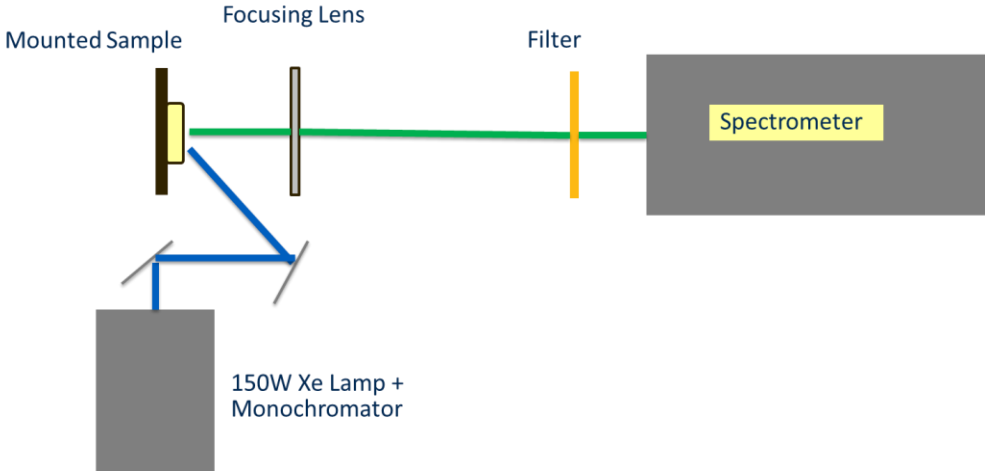

Figure 6: Schematic of utilized photoluminescence setup.

1.3.3.3 Gamma Ray Excited Photoluminescence

Photoluminescence induced through the exposure to gamma radiation behaves in a similar manner to the visible light excited photoluminescence process described above, as the energy produced by the gamma decay reaction is still expelled in the form of photons with the main difference being the energy and wavelength of the incident photons. To obtain the gamma ray excited luminescence spectra a setup was utilized that is composed of a Hammamatsu R669 PMT housed within a large lead-shielded container. The output of the PMT is fed to a multichannel analyzer (MCA) attached to a computer that displays the data as the number of total counts vs the channel number. The glass ingots were polished on one side to allow for full optical coupling to the flat window of the PMT via optical grease. The glass ingots are tented with Teflon tape to reduce the interference of ambient light. Once tented the gamma radiation point source is placed directly onto the coupled glass sample. A schematic of this gamma ray excited PL setup is depicted in Figure 7: Gamma ray excited photoluminescence measurement setup. below. The radioactive isotope point sources used are Cs-137 (0.008mCi), Ba-133 (0.001mCi), Mn-54 (0.005mCi), Zn-65 (0.005mCi), Co-60 (0.001mCi), Na-22 (0.005mCi), and Co-57 (0.001mCi) which emit at energies of 662keV, 356keV, 835keV, 1.1MeV, 1.33MeV, 511keV, and 120keV respectively. Alpha particle pulse height spectra were obtained using an Am-241 (0.00123mCi) alpha source. For alpha particle excitation measurements the tenting of the glass and glass-ceramic materials was removed as it would block much of the incoming alpha particles due to their much lower penetrative power compared to gamma radiation. This measurement setup is also utilized for the case of the gamma source

excited brightness measurements with the output of the PMT being fed directly to a current meter to determine the output level of the emission. These currents are then compared to determine a relative brightness for the samples.

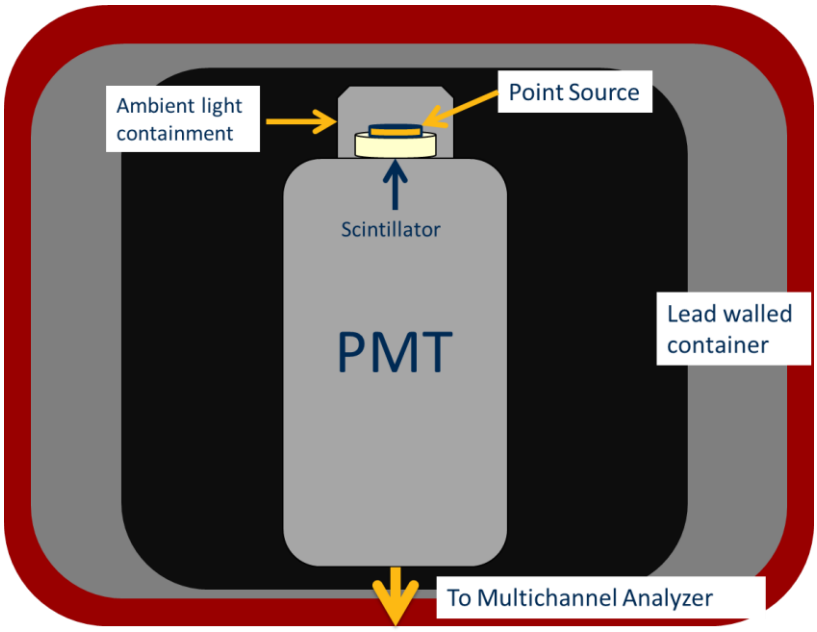

Figure 7: Gamma ray excited photoluminescence measurement setup.

1.3.3.4 Luminescent Decay Time

The decay time of the photoluminescent and radioluminescent responses is valuable to determine the scintillators' ability to quickly reset from the excited state to the ground state in order to not obscure the shape of fast, repeated radiation pulses as discussed previously. To determine the luminescent decay time of the scintillators two measurement systems were employed. For visible light excited decay time measurements a 355nm tripled YAG:Nd 10ns pulsed laser was used as the excitation source with a Tektronix DSA 602A oscilloscope to collect the luminescent decay time signal. A Hamamatsu R943-02 GaAs

PMT was employed as the light detector for this experiment. For the measurement of radioluminescent decay time the same experimental setup as the gamma ray excited pulse height spectra experiments with the display adjusted to provide the luminescent pulse trace. The decay time measurements were performed with Cs-137 and Mn-54 radiation sources. For the analysis of the decay time the pulse traces are inspected for single exponential decay regions that are represented by a straight line when the normalized light intensity is plotted against time. These single exponential regions can be easily fit to a function of the form:

$$I(t) = Io * e^{-\frac{t}{\tau}} \quad (5)$$

Where I(t) is the intensity at time t, Io is the initial intensity of the pulse (in theory this is always 1, but as the fit is not necessarily perfect some deviation can occur), and τ is the decay time. (44) (45) By utilizing trendline fits to the early straight portions of the decay trace we can find the decay time of the luminescence directly.

1.3.3.5 Neutron Pulse Detection

In the case of the compositions containing the ^{6}LiF isotope of lithium fluoride we can take advantage of the thermal neutron cross-section to detect thermal neutrons. The mechanism by which this detection is allowed is the ^{6}Li(N, α) reaction. (46) A neutron absorption event by the ^{6}Li results in the production of a tritium ion, an alpha particle, and kinetic energy which does not play a part in this detection pathway. The energetic tritium ion and the alpha particle that are produced interact with the glass matrix to transfer energy to the embedded activator ion which then excites in a similar manner to the discussed

visible light and radiation induced photoluminescence. The neutron pulse height spectra were obtained with a PuBe source contained within a polyethylene cylinder to limit the neutrons to thermal energies. The neutron pulse response was collected via a Hammamatsu R669 PMT to amplify the signal and an MCA to sort the response intensity.

1.3.3.6 X-Ray Diffraction

To identify the presence and composition of nucleated crystalline nanoparticles X-ray diffraction (XRD) was employed. XRD measurements take advantage of Bragg's law to determine the distance between crystal planes in crystalline materials which is described as follows:

$$n\lambda = 2dsin\theta \quad (6)$$

Where n is the order of relection (an integer, and in most cases for our purposes 1), λ is the wavelength of the incident x-ray, d is the crystal plane separation, and θ is the angle between the incident beam and the normal to the reflecting crystal plane. (47) As the detector aperture rotates the reflection angle changes and peaks will occur when this reflection angle allows for strong constructive interference. With amorphous glass material that possesses no uniform structure there is no unified reflection and no constructive interference, so the reflected x-rays show no strong peaks in the spectra. Since different crystal systems and structures possess different crystal plane spacing values these d values can be used to determine the detected crystalline phase. In the case of glass and glass-ceramics powder XRD is utilized as opposed to solid XRD. This works on the same principles as regular XRD. When the reflection angle matches with the aperture angle a much stronger response will be visible in the spectrum. The complication that occurs with

powder XRD is that due to the random orientation of the nucleated nanocrystals some peaks may be harder to detect as they may appear to overlap with other similar peaks with similar relative dimensions after considering the relative orientation between the nanocrystal and the detector. Once a crystalline phase has been identified by the presence of XRD peaks the size and volume fraction of this phase can be determined through examination of these XRD peaks. The diameter of the crystalline particles can be determined using the Scherrer equation:

$$D = \frac{K\lambda}{cos\theta\sqrt{\beta^2 - \beta o}} \quad (7)$$

Where θ is the angle position of the XRD peak, λ is the utilized x-ray wavelength, β is the FWHM of the XRD peak, βo is the half-width of a known spectrum reference line, and K is a shape factor with a value near 1 (0.94 for cubic nanoparticles). (48) In a similar manner the crystalline volume fraction can be determined by considering all present assigned XRD peaks with the following equation:

$$Vf = \frac{Acryst}{Acryst + Aamor} \quad (8)$$

Where A_{cryst} is the sum of the area covered by all crystallization peaks of the phase of interest and A_{amor} is the area of the amorphous portion of the XRD spectrum. (48) To confirm accurate analysis of the volume fraction the total area of the crystallized glass-ceramic XRD spectrum should be equivalent to the total area of a reference XRD spectrum taken of the fully amorphous glass.

XRD measurements were taken with the X'pert Pro Alpha-1 utilizing CuK_{α} radiation with a scanning speed of 175-190s per step with a 1^{o} anti-scatter slit at a range of $10\text{-}70^{o}$ on annealed samples ground into a fine powder via mortar and pestle to check for crystallization and determine the phases nucleated for the glass ceramic samples.

1.3.3.7 UV-Vis Transmission

Transparency, self-absorption, and expected excitation/absorption bands of the materials can be investigated through the use of UV-Vis transmission spectroscopy. Transmission and absorption measurements operate by shining a beam of light through the material and into a detector. The system then compares the intensity of the exiting light beam to the intensity of the incident light beam and calculates the percentage difference which is denoted as the percent transmittance. The wavelength of the light is then varied across the ultraviolet and visible light ranges. The percent absorbance can then be determined by taking the inverse of the transmittance. In general cases the intensity difference is caused by absorption through color centers and scattering of the incident light. However, it can also trigger the photoluminescence response of the material in cases where the incident light wavelength matches the excitation wavelength of the material, which will appear in the spectrum as a localized sharper peak. In this manner UV-Vis absorption results can be used to confirm PLE results. UV-Vis transmission and absorption measurements were taken using a Cary3000 WinUV spectrometer system.

1.3.3.8 X-ray Imaging

Emission measurements under X-ray excitation were performed in the transmission mode with a 60kV X-ray excitation source. The emitted light was imaged utilizing a CCD camera and a 45º mirror to avoid direct irradiation of the camera.

CHAPTER 2. LITERATURE REVIEW

2.1 Statement of Purpose

The goal of this research is to identify and present a glass or glass-ceramic scintillator that could perform in a similar capacity to currently used single crystal scintillators while offering a reduced production cost for the material. In order to accomplish this goal efficiently the glass systems and crystalline phases cannot be chosen at random. A review of the published literature was conducted at the outset and concurrently with the research in order to identify the most promising combinations of glass matrices and crystalline systems.

2.2 Glass-Ceramic Synthesis Methods

There are multiple ways through which glass and glass-ceramics can be produced which come with their own benefits and complications. These will briefly be reviewed in order to elucidate which procedure will best match up with our goals and available production space.

2.2.1 Melt-Quench Method

This is the most widespread and traditional method reported for the production of glassy materials. Through the melt-quench method a mixture of precursor materials, typically in a powder form, are combined and loaded into a furnace that will bring the mixture to its combined melting point. Once the mixture has melted thoroughly and had time to reach a homogenous molten liquid the mixture is removed from the furnace and

poured into a mold that is heated to the temperature range that will quench the solution down to the glass formation region. (19) (26) (49)Once the glass is obtained it is annealed to relieve internal stresses brought on through the drastic cooling rate that can lead to catastrophic mechanical failure if left unresolved.

For this method of producing the base glass a glass-ceramic can be obtained through two different methods. The crystalline phase can be prepared as nanoparticles in advance and then combined with the melt during synthesis, or in the case of certain more resilient nanoparticles they can be combined with the initial precursor mixture. (50) This method allows for more direct control of the production of the crystalline phase, but does prevent some issues such as the potential for damaging the premade nanocrystals through exposure to high melt temperatures, potential exposure to the open atmosphere at high temperatures which could lead to oxidation, and the possibility of inducing a doping gradient or other inhomogeneity through the lack of adequate mixing once the additional particles are added. The second method of nanocrystal production involves the additional heat treatment of the produced glass at temperatures near the crystallization temperature. If the base glass composition is designed with the necessary elemental supply to support the crystalline phase these heat treatments will encourage the nucleation and growth of nanocrystals, the size of which may be managed through control of the temperature and duration of the heat treatments. While this method of crystalline phase growth is less directly controllable than the above method it requires less engineering considerations for the furnace equipment and as such has a lower associated production cost.

2.2.2 Sol-Gel Synthesis

Another synthesis method for the production of glass-ceramics is known as sol-gel synthesis. In this method a colloidal solution known as a "sol" is generated from a metal alkoxide solution which is allowed to evolve until it approaches a gel-like system. Once the gel state has been achieved the remaining liquid phase is slowly removed. The solid material that is left behind is then sintered to form a glass-ceramic. There have been materials produced through this method reported such as an $SiO_2/RE_2Si_2O_7$:Ce nanocomposite where RE is either Y or Lu as well as a Zn_2SiO_4 based nanocomposite that was reported with an emission intensity comparable to standard bismuth germanate (BGO). (51) (52) The primary downside of this production method is the difficulty that comes with producing large bulk samples due to the nature of the generation of the sol-gel. It can also be difficult to obtain crack-free samples with this production method, which combined with the previous downside can lead to a high production cost.

2.2.3 Containerless Processing

A more recent development is the advent of a procedure that has been dubbed containerless processing. (53) (54) This synthesis procedure involves the sintering of a precursor powder mixture to produce a target that is then placed within an aerodynamic levitation furnace where it is levitated by an O_2 flow and melted by a high power laser. Once the target has melted the laser is shut off to allow the rapid cooling of the material. This synthesis method can allow for the production of glass and glass ceramics from materials with traditionally poor glass-forming capabilities due to the lack of contact with container walls that could induce heterogeneous nucleation. The downside of this

procedure is the severe size constraint that is placed on the possible sample production. It will be difficult to produce large commercial scintillators through this method.

2.3 Scintillating Glass-Ceramic Matrices

2.3.1 Oxide Glass-Ceramics

2.3.1.1 Silicate Glass-Ceramics

Compared to other glass matrices silicate glasses tend to exhibit higher light yields due to short absorption wavelengths. (41) Silicate glasses offer an added benefit with fewer manufacturing requirements than more halide based systems which can reduce the cost of production. Unfortunately, many oxide glasses suffer from densities below 4g/cm^3 which limits the stopping power of the material. There have been efforts to improve the density of silicate based glass scintillators through the incorporation of heavy metal oxides such as Gd_2O_3, Y_2O_3, and Lu_2O_3.

A system based on the $LuSiO_5$ (LSO) composition doped with Ce^{3+} was reported by Bescher et al. in 2000. (55) LSO has long been a promising scintillator composition option due to its impressive performance features in high light output, fast decay time, and reasonable chemical stability, but has not found wide commercial success due to the limitations of single crystal growth. This material was produced through the sol-gel synthesis procedure discussed previously, which presents a quicker production time over the single crystal growth, but still took several days to complete. The performance of the glass-ceramic was compared to an LSO single crystal produced via the Czochralski method. The reported PL and PLE spectra present a broad emission band from 400-430nm

and an excitation peak at ~340nm due to the dopant Ce^{3+}. The LSO glass demonstrates a decay time of 34.7ns which is valuable for detection applications. Crystallization of this system was reported with confirmation through TEM imaging confirming the presence of LSO nanocrystals which is presented in Figure 8: TEM image of LSO nanocrystals in glass-ceramic reported by Bescher et al.. When excited by an Am-241 source as visible in Figure 9: Am-241 gamma excitation comparison of an LSO glass-ceramic and LSO single crystal originally presented by Bescher et al.the LSO glass-ceramic exhibits similar performance to the LSO single crystal, with a light yield of ~70% that of the single crystal coming in at 23,000 ph/MeV; however, both of these materials only demonstrate energy resolutions in the 30% range which leaves a lot of room for improvement before finding use in commercial applications.

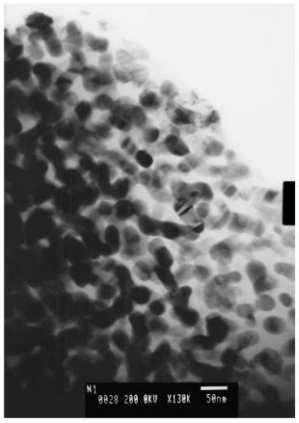

Figure 8: TEM image of LSO nanocrystals in glass-ceramic reported by Bescher et al. (55)

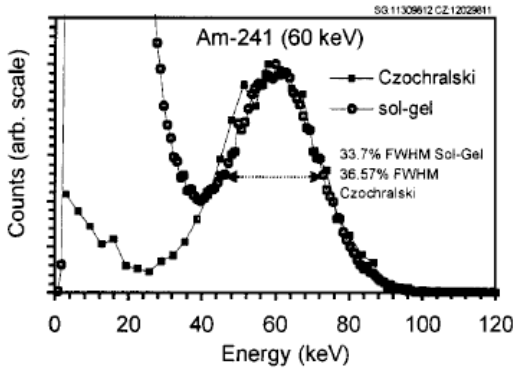

Figure 9: Am-241 gamma excitation comparison of an LSO glass-ceramic and LSO single crystal originally presented by Bescher et al. (55)

Of the other lanthanide oxides that have been investigated Gd_2O_3 has garnered much attention for use in improving the density of silicate based glasses due to the added benefits of the energy transfer capabilities of Gd^{3+} to trivalent activator ions such as Ce^{3+}, Tb^{3+}, and Eu^{3+} leading to greater light yield as well as its high thermal neutron cross-section. (56) (57) (58) (59) In particular, Eu^{3+} finds easy incorporation into Gd_2O_3 based matrices due to its comparable size and electronegativity. A Eu^{3+} doped CaGdSiB based glass was reported by Wantana et al. in 2018 through the melt-quench method. (57) The reported PL spectra show sharper Eu^{3+} features in the glass than those of the broad band of the BGO single crystal which could potentially allow for greater tuning of the detection setup to the scintillator. The primary emission peak at 600nm would be suitable for applications utilizing CCDs for the detector system. The material is reported with a density of 4.08g/cm^3 which is typically sufficient for gamma detection applications, but could stand further improvement. The reported absorption spectrum demonstrates low self-absorption for the 610nm Eu^{3+} emission with an absorption edge setting in strongly at 400nm. Strong energy transfer between Gd^{3+} and Eu^{3+} was reported through the absence of an expected CT band that was superimposed by the transition peaks of Gd^{3+} which is valuable for improving the

efficiency of the scintillator. The reported luminescent decay time remains on the order of ms which is not ideal for gamma applications, but could remain promising for x-ray imaging. The glass-ceramic does show a strong luminescence response under x-ray excitation which is visible in Figure 10: X-ray excited luminescence comparison of Eu doped CaGdSiB based glass and BGO single crystal reported by Watana et al. This reported luminescence shows a peak at a 611nm similar to the PL measurements. The scintillation efficiency of the glass-ceramic was reported at 13% of the BGO single crystal, which is strong but leaves room for further improvement.

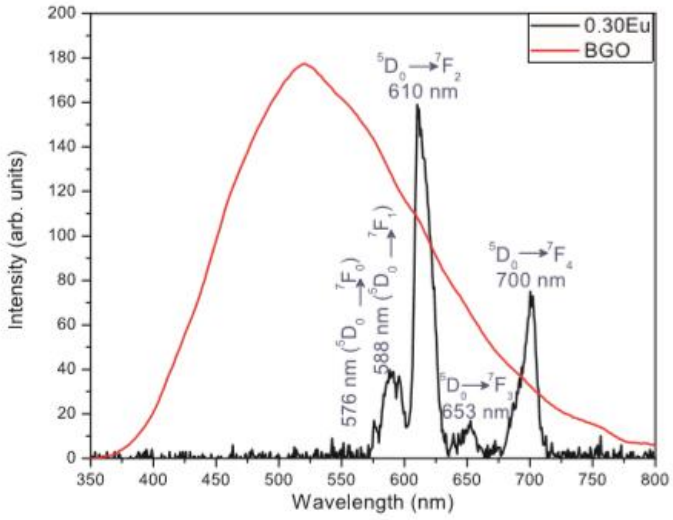

Figure 10: X-ray excited luminescence comparison of Eu doped CaGdSiB based glass and BGO single crystal reported by Watana et al. (57)

2.3.1.2 Germanate Glass-Ceramics

Germanate based glass matrices have an inherently higher density and Z number due to the constituent Ge content which makes these systems potentially attractive for detection applications as these features will provide a naturally high gamma ray stopping power compared to silicate based glasses. Germanate glass systems have also been shown to

possess smaller maximum vibrational frequencies than some other glasses which has the potential to improve the efficiency of incorporated dopant ions. (60) Rare earth borogermanate crystals have been reported as viable hosts for Eu^{3+}, Tb^{3+}, and Tm^{3+} dopants which makes compositions based on these crystal systems a good starting point for investigation. (61) (62) (63) Glass systems can be designed based on these crystal systems that will precipitate the crystalline phase after heat treatments which shows promise for future applications. However, these dopants come with some complications as Eu^{3+} requires carefully controlled production conditions to prevent oxidation and Tb^{3+} luminescence suffers from long decay times that make it non-ideal for gamma detection applications. Despite the long decay time Tb^{3+} can still be of use in X-ray based medical and industrial applications. (56)

Bismuth germanate, $Bi_4Ge_3O_{12}$ (BGO), single crystals already find use as scintillators and possess a cubic crystal structure that allows for potential refractive index matching which positions this composition as an interesting option for producing glass-ceramics. BGO scintillators possess a wide band gap which is beneficial for high energy particle detection. (48) Binary Bi_2O_3 and GeO_2 based glasses have been of interest as both oxides have high optical basicity and large electronic polarizabilities that lead to a high refractive index. (64) A glass of composition similar to typical BGO was reported by Polosan et al. in 2010 and was used to produce a BGO glass-ceramic. (48) The reported glass-ceramics exhibited a density of $6.7 g/cm^3$ which surpasses many other silicate based glass-ceramics. Successful crystallization of the $Bi_4Ge_3O_{12}$ crystalline phase was reported with some additional phases present. After annealing at temperatures above 893K all other phases were dissolved and only the desired $Bi_4Ge_3O_{12}$ phase remained. Crystalline volume

fractions of 44% were reported with glass formation and crystallization onset temperatures depending on the ratio of Bi_2O_3 to GeO_2 in the glass composition. TEM and SAED imaging of the BGO glass-ceramic which are presented in Figure 11:TEM and SAED measurements of BGO based glass ceramic reported by Polosan et al. confirm the presence of cubic structure BGO nanocrystals. The material suffered a loss of transparency up to 20% after annealing for crystallization which could provide difficulties in further improvement through additional crystallization as well as attempts to combine multiple layers of the material to produce larger scintillator elements. The reported glass-ceramics were translucent, but possessed a reddish-brown coloration which could indicate production of color center defects that can behave as non-radiative recombination sites which will negatively impact the performance of the material. Color center formation was also reported after chronic exposure to gamma radiation which is very problematic for gamma detection applications. The reported PL and PLE spectra of both the produced glass-ceramic and a BGO single crystal show similar peaks at 500nm and 300nm respectively. Energy resolution numbers were not reported for this material, but a light yield of 4,000 ph/MeV and a decay time of 30ns were reported. This light yield is notable for a glass-ceramic, but without energy resolution reported it is possible these are still not sufficient for commercial use.

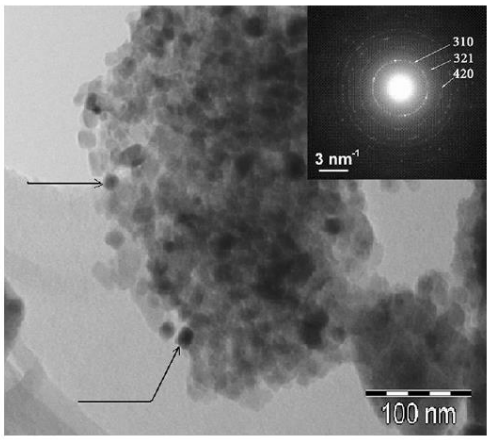

Figure 11:TEM and SAED measurements of BGO based glass ceramic reported by Polosan et al. (48)

Barium titanium germinate (BTG) glasses and glass-ceramics have been long investigated for fiber optics, thermal properties, and optical nonlinearity, but have only recently garnered attention for potential use in scintillation applications. A glass-ceramic based on $Ba_2TiGe_2O_8$ fresnoite crystal system was reported by Yanagida et al. in 2018. (65) XRD spectra reported confirm the presence of the $Ba_2TiGe_2O_8$ crystalline phase. The reported PL and x-ray excited decay times on the order of 10s of ns are sufficient for detection applications. The reported X-ray excited luminescence spectra visible in Figure 12: X-ray induced luminescence of BTGx glass-ceramics reported by Yanagida et al. possess a peak around 500nm which is slightly low for CCD coupling, but still sufficient. The x-ray response demonstrates increased light yield after annealing to produce the crystalline phase of the glass-ceramic with the 1250ºC treated sample showing the greatest improvement. Transmittance measurements reported show a low self-absorption for the doped emission wavelength, but the transmittance spectra of the heat treated samples show a significant loss of transparency. No gamma excitation measurements or energy

resolutions were reported for this material which makes assessment for those detection applications difficult.

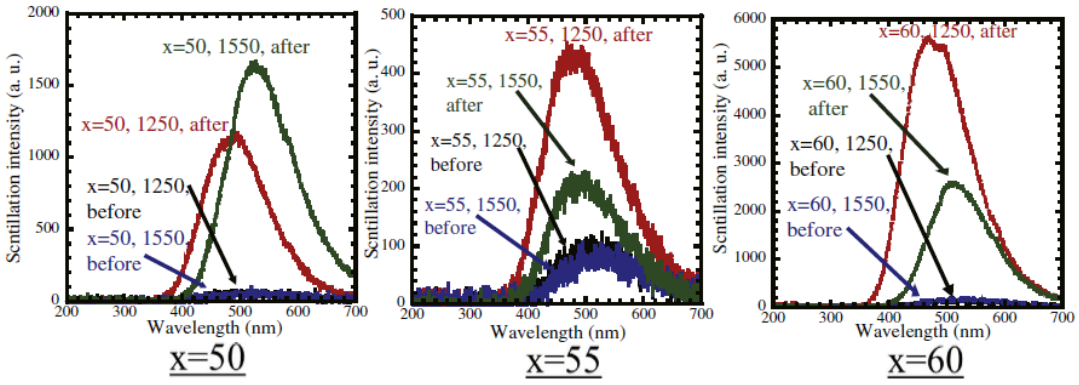

Figure 12: X-ray induced luminescence of BTGx glass-ceramics reported by Yanagida et al. (65)

2.3.2 Oxyfluoride Glass-Ceramics

The branch of glasses known as oxyfluorides look to combine the beneficial properties of silicate glasses with the low phonon energy environment of fluorides. (21) (66) Due to the natural incorporation of large amounts of fluorine content in these types of glasses they typically lend themselves to the nucleation of fluoride-based crystalline systems such as LaF_3 and CaF_2. Oxyfluoride glass-ceramics have primarily been reported as hosts for Tb^{3+} which is not ideal for fast detection applications. These glasses tend to possess low density which negatively impacts their stopping power and tends to be non-ideal for gamma detection applications. However, this lower density allows for the possibility for use in neutron detection applications. As a result, ^{6}LiF becomes a popular option as a precursor material to provide a thermal neutron cross-section. Constituent Al_2O_3 has also found use in oxyfluoride glass-ceramic systems as it reduces the prevalence of nonbridging oxygen defects in the glass matrix which can cause a weakening of the matrix leading to reduced

light output. (21) (66) Rare-earth aluminosilicate oxyfluoride systems doped with Tb^{3+} was reported by Pan et al. in 2008. (21) (66) A LaF_3 containing glass-ceramic was successfully produced through heat treatment anneals and confirmed through XRD. The reported PL spectrum shows peaks at 470, 540, 570, and 620nm characteristic of Tb^{3+} doping. Reported transmittance spectra show an absorption edge beginning near 380nm which matches well with Tb^{3+} doping. Beta excited luminescence spectra were reported that show a strong beta response which is visible in Figure 13: Beta radiation induced luminescence of the LLASOF glass-ceramic under heating conditions of as-cast (a) 460C for 6h (b) 480C for 6h (c) and a commercial glass (d) as reported by Pan et al., but no gamma excitation or energy resolution information is reported for this material.

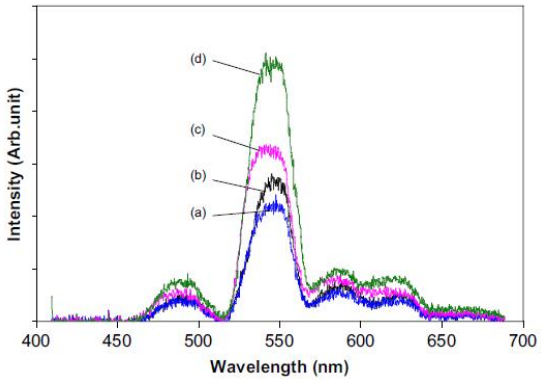

Figure 13: Beta radiation induced luminescence of the LLASOF glass-ceramic under heating conditions of as-cast (a) 460C for 6h (b) 480C for 6h (c) and a commercial glass (d) as reported by Pan et al. (66)

CaF_2 based glass ceramics have also drawn interest for applications such as upconversion materials, white light emitting diodes (LEDs), and scintillators. (67) (68) (69) (70) (71) (72) An oxyfluoride system featuring Eu^{3+}-doped CaF_2 was reported by Secu et al. in 2009. (49) After annealing at 760ºC for 15 minutes the reported XRD spectra exhibit sharp peaks in close agreement with those expected of the CaF_2 crystalline phase. The

reported PL and PLE spectra show characteristic bands for Eu^{3+} doping at 450 and 350nm respectively with an additional minor emission peak at 600nm. This emission spectrum couples well with current typical detector PMTs, but the extraneous emission band in the red light region could result in lower overall quantum efficiency of the scintillator. The absorption spectra reported for this glass-ceramic show an absorption edge beginning at roughly 350nm which matches well with the Eu^{3+} emission wavelength. However, the presented absorption spectra show an increase in absorption, and therefore a decrease in transmittance with increasing crystallinity with this absorption increase bleeding into the emission region which would limit the ability to improve detection performance through additional growth of the crystalline phase. The reported luminescent decay time shows an improvement when transitioning from cast glass to glass-ceramic, but still remains in the ms range which is not ideal for gamma detection. A similar oxyfluoride system containing Eu^{2+} doped CaF_2 was reported by Fu et al. in 2009. (20) After heat treatments at 760C for 4 hours the reported XRD spectra show the successful nucleation of CaF_2 crystalline phase alongside TEM imaging of the nanocrystals within a glass matrix which is visible in Figure 14: TEM image of Eu doped CaF_2 glass-ceramic reported by Fu et al.. The Eu^{2+} luminescence shows a peak near 400nm under both UV and X-ray excitation with a great increase in intensity between the base glass and the glass-ceramic.

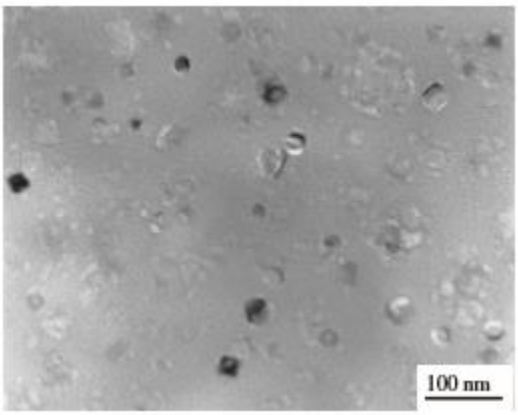

Figure 14: TEM image of Eu doped CaF_2 glass-ceramic reported by Fu et al. (20)

2.3.3 Fluorozirconate Glass-Ceramics

Fluorozirconate glass-ceramics based on the ZBLAN 53Zr-20Ba-4La-3Al-20Na composition have been investigated previously for x-ray storage phosphor and upconversion applications, but many of these have suffered from loss of transparency due to growth of large crystalline particles for their reported investigations. (24) (73) On the other hand, the hosting capabilities of high rare-earth concentrations, low phonon energy, and high transparency (when crystals are kept nanoscale) offer a promising option for glass-ceramic detection applications. (74) A glass ceramic based on a similar composition to ZBLAN was reported in 2015 by Maalej et al. (74) While the material was kept transparent after crystallization this resulted in issues in concretely identifying the present crystalline phase through the reported XRD spectrum, although the pattern was able to be matched to a monoclinic C-centered unit cell or a tetragonal body-centered cell structure.

High resolution transmission electron microscopy images were reported that did confirm the presence of some sort of crystalline nanoparticles. It is of note that fluorozirconate glass-ceramics doped with Eu^{3+} display no luminescence unless bromine is also present in the material, at which point it is reported with emission peaks at 425nm and 570nm under X-ray excitation and peaks at 577nm, 585nm, 595nm, and 620nm under 532nm visible light excitation. (73) (74) The visible light excited transitions are attributed to the $^5D_0$-$^7F_0$, $^5D_1$-$^7F_3$, $^5D_0$-$^7F_1$, and $^5D_0$-$^7F_2$ transitions respectively. The reported PL spectrum presents a highly resolved pair of peaks in the 580-600nm range, but these are not attributed to any known transition in the dopant. These additional emissions could potentially cause efficiency issues for scintillators made of this material. The visible light excited emission is reported with a decay time of 5.5ms which is quite slow for many detection applications. A decay measurement performed on the direct narrowed excitation of the $^5D_0$-$^7F_0$ transition reports a shorter decay time of 0.6ms which is an improvement over the 5.5ms, but still slower than typically desired.

Similar to fluorozirconate, fluorochlorozirconate glass is derived from the same ZBLAN base composition with a portion of the BaF_2 replaced with $BaCl_2$. These have been investigated in X-ray storage applications in order to reduce the scattering of light through the use of nanoscale crystallites within glass matrices. A fluorochlorozirconate glass-ceramic was reported by Schweizer et al. in 2006. (75) After anneals at 260ºC and 280ºC the precipitation of hexagonal and orthorhombic $BaCl_2$ nanocrystals are reported respectively; past 290ºC the hexagonal phase is completely replaced by the orthorhombic phase. The Eu^{2+} doped material is reported with PSL efficiency increasing with increasing volume fraction of the orthorhombic phase, up to 80% efficiency. However, with the

volume fraction required to reach this efficiency the material suffers greatly in terms of transparency loss. This glass matrix is also reported to suffer from oxidation issues which could compromise the valence of the dopant Eu^{2+} ion. In 2013 another Eu^{2+} doped fluorochlorozirconate glass-ceramic was reported by Alvarez et al. (25) This material shows no luminescence as-cast, but after anneals to form nanocrystals a broad emission band is reported at 403nm and attributed to either the 5d-4f or 5d-5f transition in Eu^{2+} in orthorhombic $BaCl_2$ nanocrystals. The wavelength of this emission could couple well with PMT based detector systems which is promising. In situ TEM heating and HRTEM images were taken to confirm the crystalline phases and are visible in Figure 15: HREM imaging and associated FFTs and diffraction patterns of several nanocrystalline phases formed in situ in FCZ glass-ceramic reported by Alvarez et al.. These phases were identified as hexagonal $BaCl_2$ after treatment at 265ºC and orthorhombic $BaCl_2$ after treatment at 300ºC. In addition to these targeted phases orthorhombic and face-centered cubic BaF_2 phases were also present in all reported samples regardless of composition or treatment parameters. This report also appears to be one of the first mentions of BaF_2 nanocrystal formation in FCZ glass compositions which offers another tuning path for the material. However, the reported BaF_2 nanocrystals were shown to form large clusters within the glass-ceramic which could limit their use for direct improvement of glass-ceramic scintillator performance. There were no gamma excitation spectra or energy resolutions reported for these compositions.

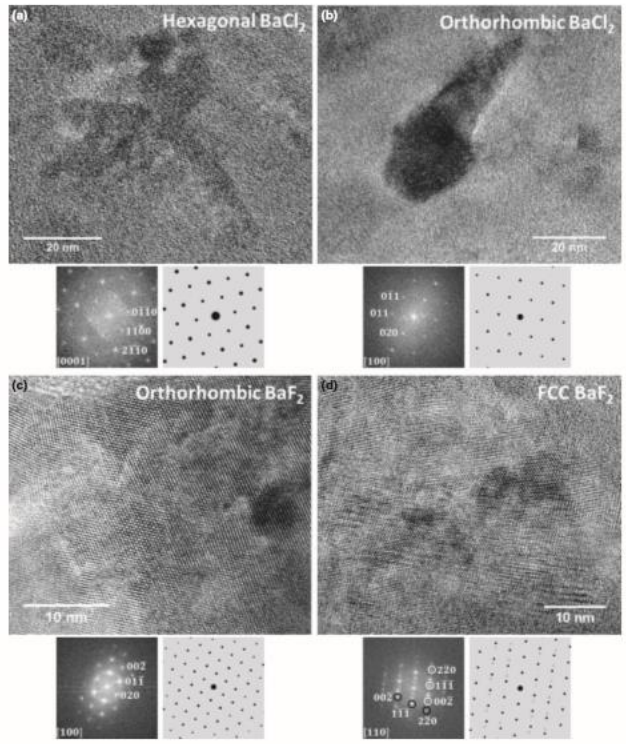

Figure 15: HREM imaging and associated FFTs and diffraction patterns of several nanocrystalline phases formed in situ in FCZ glass-ceramic reported by Alvarez et al. (25)

Fluorobromozirconate glass-ceramics are also produced in much the same way as the previous flurorzirconate based glasses with a portion of the Na content provided via NaBr. The bromide substitution was pursued after similar substitutions led to increased PSL and one of the first FBZ glass-ceramics was reported by Edgar et al. in 1999 with a composition of $53ZrF_4$-$20BaF_2$-5NaF-15NaBr-$3AlF_3$-$1.5LaF_3$-$1.5YF_3$-$1EuF_2$ with a follow-up study performed in 2003 by Secu et al. on a FBZ glass-ceramic with composition of $53ZrF_4$-$20BaF_2$-5NaF-15NaBr-$3AlF_3$-$1.5LaF_3$-$1.5YF_3$-$1CeF_3$. (76) (77) While materials of the original ZBLAN composition have a tendency to show relatively broad XRD peaks this Br added FBZ composition is reported with sharp XRD peaks corresponding to the hexagonal $BaBr_2$ phase after annealing at 260ºC and peaks corresponding to the orthorhombic $BaBr_2$

phase appearing after anneals at 290ºC. The Ce doped series shows doping dependence on the nucleated crystal structure with 1% Ce doping producing hexagonal $BaBr_2$ and NaBr while 0.01% Ce doping produced orthorhombic $BaBr_2$. The reported material prepared without the bromine substitution in this study shows no luminescence from either the doped Eu^{2+} or Ce^{3+} which is attributed to competing non-radiative charge transfers in the glass matrix. With the addition of the Br substitution broad luminescence bands are reported at 413nm and 485m attributed to Eu^{2+} and 380nm attributed to 5d-4f transitions in Ce^{3+}. The downside of this reported composition comes from the loss of transparency in the annealed glass-ceramic and the long reported decay time of the luminescence. The group has continued efforts in optimizing this composition since the first report, but their primary goal has been for use as an X-ray storage phosphor, so there is still a lack of reporting on the gamma detection capabilities. (73) (77) Their FBZ composition was reported to suffer from devitrification at Ce doping levels of 1%, which could prove problematic in our efforts to increase light yield.

2.4 Crystal Compositions to Embed

2.4.1 Oxide Crystals

2.4.1.1 ZnO

The ZnO system has been investigated for emission material and transparent conductive device applications, but had not been investigated for use in glass ceramics until

recently. One of the earliest reports of glass-ceramics containing ZnO nanocrystals was by G. Chen et al. in 2004. (78) The basis of the glass ceramic was a ternary SiO_2-B_2O_3-ZnO composition that was then heat treated to nucleate ZnO nanocrystals. The undoped glass-ceramic is reported with emission peaks at 400nm for both visible light excitation and X-ray excitation with the response reaching a maximum after heat treatments at 350ºC which are shown in Figure 16: PL (a) and X-ray induced RL (b) spectra of the ZnO containing borosilicate glass-ceramic reported by Chen et al.. Once heat treatment temperatures reach 700ºC the glass-ceramic becomes fully opaque. The reported decay times of the X-ray excited emission remain in the ns range with two mechanisms presenting decay times of 7ns and 170ns which are compatible with detection applications.

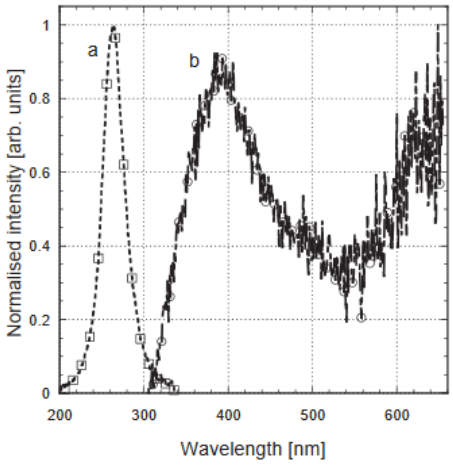

Figure 16: PL (a) and X-ray induced RL (b) spectra of the ZnO containing borosilicate glass-ceramic reported by Chen et al. (78)

The material presented by Masai et al. in 2014 was based on a CaO-B_2O_3-ZnO-Al_2O_3-K_2O-SiO_2 (CaBZAKS) composition that was heat treated to nucleate a ZnO crystalline phase. (79) The reported XRD spectra show increasing intensity of sharp peaks as the treatment temperature is increased, with full proportional matching to the ZnO reference

pattern occurring at 620ºC. The increase in crystallinity also leads to a decrease in the transparency of the material, with any treatment over 590C resulting in some loss of transparency and samples having undergone treatments at 640ºC nearly fully opaque. The reported decay times of the PL emission decrease with increasing heat treatment temperature and the fast portion of the decay times are reported in the single ns range. The X-ray luminescence spectra, visible in Figure 17: X-ray induced RL spectra of ZnO containing CaBZAKS glass-ceramic reported by Masai et al. show a slight increase in intensity with increasing heat treatment temperature, but the overall change is very slight. The decay times of the X-ray luminescence did not appear to depend on crystallinity and the fast portion is reported at 0.6ns which is very promising. The X-ray response of this nanocrystal system appears promising, but without reported gamma ray excitation measurements it is difficult to gauge how useful it will be for gamma detection applications.

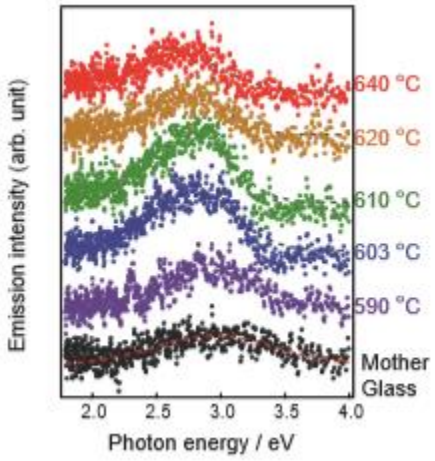

Figure 17: X-ray induced RL spectra of ZnO containing CaBZAKS glass-ceramic reported by Masai et al. (79)

2.4.1.2 $LiAlSi_4O_{10}$

Lithium aluminosilicate crystals have been previously studied for applications as ionic conductive materials and as dosimeters. Due to the presence of Li incorporation of ^{6}Li is possible which also presents interest in neutron detection applications. Nikitin et al. reported on a silicate glass containing $LiAlSi_4O_{10}$ nanocrystals for neutron detection applications in 2013. (50) This glass-ceramic was synthesized by preparing $LiAlSi_4O_{10}$ nanocrystals separately and then mixing those nanocrystals with the other precursor materials that then go into the melt. Thermal neutron excitation measurements were reported of the produced glass-ceramic and a commercial neutron detection glass known as GS20. The thermal neutron spectrum of the reported glass-ceramic is visible in Figure 18: Thermal neutron excitation spectrum of $LiAlSi_4O_{10}$ containing glass-ceramic reported by Nikitin et al.. The $LiAlSi_4O_{10}$ glass-ceramic demonstrated a 1.79 times higher light yield over that commercial glass scintillator which provides much promise for this system as a neutron detection scintillator. Another report on the performance of the undoped crystal of $LiAlSi_4O_{10}$ was provided by Yanagida et al. in 2017. (80) The crystal is reported with an absorption edge near 300nm which would be compatible with most currently used dopants. The reported X-ray excited decay time of 1.9ms is not ideal for detection applications, but as this is the performance of the undoped crystal this could be drastically improved through the incorporation of activator dopant ions.

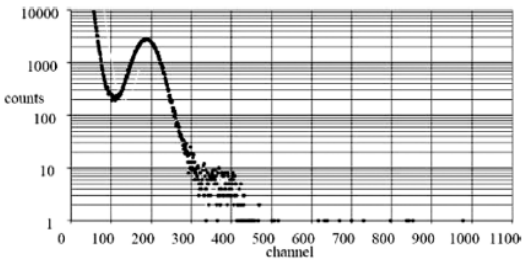

Figure 18: Thermal neutron excitation spectrum of $LiAlSi_4O_{10}$ containing glass-ceramic reported by Nikitin et al. (50)

2.4.1.3 $Lu_2Si_2O_7$

The general optical properties of $Lu_2Si_2O_7$ (LSO) based crystals have been investigated since the 1980s, but it was not until the year 2000 that the scintillation properties of these materials have been pursued for investigation. (81) In more recent years this material has been reported on by Nikl et al. in 2011. (51) The reported silicate based LSO nanocomposite requires relatively high temperatures of 1100ºC to see crystallization, but presents a strong pure XRD spectrum matching the reference for $Lu_2Si_2O_7$. The material is reported to fracture at high anneal temperature in excess of 1250ºC, but retain their stability and crystal formation at 1100ºC. The RL excited emission spectrum shows a broad peak at 440nm that is typical of its Ce^{3+} dopant. The reported decay time for this emission is 34ns which would be sufficient for detection applications. However, the current performance under x-ray excitation requires great improvement for commercial use.

2.4.1.4 $Na_6Ca_3Si_6O_{18}$

Sodium-calcium silicate materials have recently drawn the eye as a host for Nd^{3+} in particular for use in solid state laser applications. A glass-ceramic based on the $Na_6Ca_3Si_6O_{18}$ crystal system was reported by Li et al in 2011. (82) With progressive heat

treatments the nucleation of the $Na_6Ca_3Si_6O_{18}$ crystal phase was confirmed by the reported XRD spectra. One of the heat treated samples was reported with decreased density after heat treatment due to the generation of blowhole defects. This combination of density loss and potential non-uniformity caused by the defect generation poses a strong issue for use in detection applications. The non-uniformity will greatly negatively impact the energy resolution for gamma detection. The reported emission peaks from the Nd^{3+} doping push into the far-red and near-infrared wavelengths at 900nm and 1060nm which don't match well with most currently used PMTs, but could be compensated for with a different rare-earth dopant activator. The ability to maintain 65% transparency after completion of the heat treatments is an attractive feature of this system, but not enough to pursue the use of it in detection applications on its own.

2.4.1.5 Ba_2SiO_5

The Ba_2SiO_5 system was identified as an interesting scintillator crystal system due to the benefits of possessing good optical transparency and high radiation hardness to withstand long periods of high energy irradiation. A glass-ceramic based on the stoichiometric composition of Ba_2SiO_5 with additional Gd^{3+} loading was reported by Novotny et al. in 2015. (83) This adherence to the stoichiometric composition of the desired crystalline phase is reported to suppress the formation of defects at the glass-crystal interface that typically form due to the mass transfer that occurs during the anneal stage. This is currently speculated but difficult to confirm; however, this provides a good potential benefit to the implementation of stoichiometric compositions for the base glass matrix in addition to the enhanced radiation hardness typically associated with these compositions. The reported glass-ceramic is stated to crystallize at temperatures of 800-900ºC when the

anneals are kept to a short time period. But when temperatures are further increased the material suffers from a runaway crystallization reaction that results in a severe loss of transparency through the production of large micro-sized crystalline particles. The reported blue luminescence of these materials matches well with currently employed detection PMTs and exhibits decay times in the 10s to 100s of ns range. While this material was reported with a light yield under gamma excitation, it is still lacking at 100 ph/MeV which leaves much room for improvement. With a doubled Gd loading in the composition the material is reported to produce a photopeak for Cs-137 which is promising for prospects of further improvement, however the light yield for this improved material is reported at still just 300ph/MeV. The predicted high radiation hardness is confirmed through transparency measurements after gamma ray irradiation from a Co-60 source and the Cs-137 photopeak is reported to suffer no shift after this irradiation as well. With improvements to the light yield and investigation of the energy resolution of the material this presents an attractive option for use in detection applications.

2.4.2 Fluoride Crystals

2.4.2.1 $\underline{CaF_2}$

Scintillating glasses and ceramics based on Li content have been investigated as an alternative low cost neutron detection material due to the low density of Li and the oxyfluoride glass matrices supporting it. The ability to incorporate Li in the form of ^{6}Li that naturally supports neutron detection through the ^{6}Li(N, α) reaction. So far for these materials the poor light yield has been the factor holding them back. A CaF_2 based ceramic

was reported by Glodo et al. in 2005 that demonstrates impressive possible light yields of 45,000 ph/neutron. (84) However, the low transmittance of this ceramic leaves room for improvements and the low thickness of the material could lead to further issues when considering the lack of transparency. A glass-ceramic produced of a similar material could be of greater interest to combine the benefits of fluoride and oxyfluoride glasses with the high light yield presented from the ceramics. These glass-ceramics have been suggested to support the incorporation of Eu^{2+}, Ce^{3+}, or Tb^{3+} dopants which present good options for emission capabilities. (85) Currently Eu^{2+} appears to be the activator of choice for use with CaF_2. A glass ceramic based on the CaF_2:Eu^{2+} composition was reported by Fu et al. in 2009 for use as a neutron detector which was mentioned above, but will now be discussed in more focus on the crystalline phase. (85) The reported XRD spectrum indicates the presence of only CaF_2 crystalline phase which bodes well for control of the composition and crystal phase morphology. The reported size of the CaF_2 crystalline particles was 35nm, which satisfies both the desires for large crystalline particles while remaining nanosize to limit scattering. Reported luminescence spectra under UV excitation indicate that the Eu^{2+} ions occupy two different sites in the CaF_2 based matrix of the unannealed glass, but move to primarily a single site in the annealed glass-ceramic and comparison single crystal. This single emission peak located near 420nm matches well with widely used PMTs. The emission intensity of the glass-ceramic greatly exceeds that of the raw glass which confirms the benefits of the nucleation of nanocrystals. However, this glass-ceramic was not reported with luminescence measurements under neutron bombardment which makes it difficult to judge the full performance benefits for the neutron detection applications. RL measurements are reported with a comparison between the glass-ceramic

and single crystal, with the glass-ceramic demonstrating a light yield of 30% that of the single crystal. All of these factors point to a great promise in the use of CaF_2 based glass-ceramics for neutron detection with further improvement in the light yield and investigation of the real neutron scintillating capabilities of the materials.

2.4.2.2 LaF_3

The LaF_3 crystal system has drawn interest previously thanks to its potential for low-cost large volume production and competitive yields. (66) This crystal phase possess an extensive solid solution with rare earth ions making it a good host for rare earth dopant ions. (19) (86) The combination of fluoride based crystals and fluoride based glasses to compose a glass-ceramic provides the added benefit of ease of shaping for various applications such as fibers for large optics. The low phonon energy of LaF_3 sites in glass-ceramics could also increase the probability of radiative recombination of electron-hole pairs in the glass matrix which would result in a higher light yield. (19) (87) Pan et al. reported on a LaF_3:Tb^{3+} based glass-ceramic recently in 2009. (21) The reported compositions include a lithium-cadmium aluminosilicate oxyfluoride composition of $30SiO_2$-$15(AlO_{1.5})$-$22PbF_2$-$29CdF_2$-$4YF_3$ (LCASOF) and a lithium-lanthanum aluminosilicate oxyfluoride composition of $55SiO_2$-$6Al_2O_3$-$28Li_2O$-$11LaF_3$ (LLASOF) which were prepared as glass through the melt-quench technique. The reported DSC investigation shows that the LCASOF glass possesses a glass transition temperature at 400ºC and a temperature of crystallization at 565ºC while the LLASOF glass possesses a glass transition at 406ºC and multiple temperatures of crystallization at 540ºC, 667ºC, and 711ºC. The reported XRD spectra show the production of LaF_3 crystalline phase within the LLASOF glass-ceramic after an anneal performed at a temperature between the glass

transition and the first crystallization temperature. The reported PL spectra show typical emission bands of Tb^{3+} at 489, 542, 585, and 622nm attributed to the $^5D_4$-^7F_i (i = 6, 5, 4, and 3) transitions. The reported PL intensity of the LLASOF glass-ceramic is significantly stronger than that of the LCASOF glass-ceramic, which paints the LaF_3 based sample as the better candidate for improvement in the immediate future. The presence of LaF_3 within the glass matrix is also reported to allow for Tb doping of 4.0at% without visible devitrification in comparison to the much lower threshold of 1.0at% at which point the LCASOF composition shows spontaneous devitrification. This identifies LaF_3 as a great benefit for allowing large doping concentrations for activator ions that do not suffer from concentration quenching such as Tb^{3+}, which the paper reports the PL intensity of the glass-ceramic increasing proportionally with the Tb concentration without signs of concentration quenching. The beta induced luminescence spectra were reported for the LLASOF glass-ceramic and for a commercial neutron scintillating glass known as IQI-301 and are visible in Figure 19: Comparison of beta induced luminescence of LaF_3 containing glass-ceramic (a) and IQI-301 commercial glass as reported by Pan et al.. The glass-ceramic demonstrates light yield comparable to that of the commercial scintillating glass. The performance of this glass-ceramic system could be very promising with further investigation directly into the gamma or neutron detection capabilities.

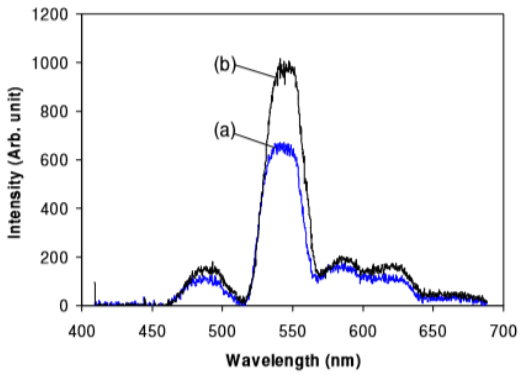

Figure 19: Comparison of beta induced luminescence of LaF_3 containing glass-ceramic (a) and IQI-301 commercial glass as reported by Pan et al. (21)

2.4.2.3 GdF_3

Rare earth halide nanocrystal systems utilizing Gd have shown great promise as scintillator materials due to the many benefits Gd inclusion can provide such as high density, high radiation stopping power, and potential energy transfer capabilities from Gd^{3+} ions to trivalent rare earth activator ions within the glass matrix. Reports of such materials were made by Kang et al. in 2012 and Lee et al. in 2014. (88) (15) The GdF_3 glass-ceramic reported by Lee et al. followed a composition of $40SiO_2$-$26Al_2O_3$-15NaF-$16GdF_3$-$3TbF_3$ in mol ratios. The reported PL spectra show typical emission peaks for Tb^{3+} doping at 491, 543, 586, and 623nm. Absorbance measurements reported on this composition reveal an absorbance edge that is compatible with the utilized Tb^{3+} luminescence as well as other potential dopant candidates like Ce^{3+}. The reported XRD spectra confirms the presence of hexagonal GdF_3 nanocrystals which will be beneficial for improving light output, but the non-cubic crystal structure requires that the crystalline phase particles are kept nanoscale in size to prevent scattering. These crystals were reported at 19.2% volume fraction which is significant as the material retained its transparency, but this still leaves room for

improvement of the material. The decay time of this material remains relatively long at 2.85ms due to the use of Tb^{3+} as the activator ion, but could still stand to find use for X-ray imaging.

Another crystal system of interest has been $GdBr_3$ which was also reported on by Kang et al. and Han et al. for similar reasons as that of GdF_3. (14) These bromide based glass materials look to emulate the success of many bromide based single crystals through the benefit of a greater low phonon energy environment effect compared to that of F. The glass produced by Han et al was tested under Cs-137 excitation and exhibited an energy resolution of 27%. After heat treatment at 750C for 10 hours small $GdBr_3$ nanocrystals were seen in TEM images presented below in Figure 20: TEM images of GdF_3 (a) and $GdBr_3$ (b) containing glass-ceramics as presented by Han et al.. Kang et al. reported on an updated composition glass scintillator with gamma excitation spectra utilizing Cs-137, Na-22, and Ba-133 sources and compared to that of a NaI:Tl single crystal scintillator which is visible below in Figure 21: Gamma excitation spectra of $GdBr_3$ based glass and NaI:Tl single crystal as reported by Kang et al.. The $GdBr_3$ glass scintillator exhibits an energy resolution of 20% under 662keV Cs-137 excitation compared to the 7% of the single crystal. The light output of the glass is also reported at about 5% of the NaI single crystal giving a light output of ~2000 ph/MeV. While these are impressive for a glass material this does still leave room for improvement. This material was also tested with alpha and neutron emitting sources and presents visible photopeaks for both alpha and thermal neutron excitation, which could provide value for a multi-source detecting material. The reported Ce^{3+} doped material demonstrates a decay time of 68ns which is sufficient for most detection applications. With further improvement of the light output and energy resolution

on this matrix/crystal system it could provide a very promising candidate for use in many detection applications.

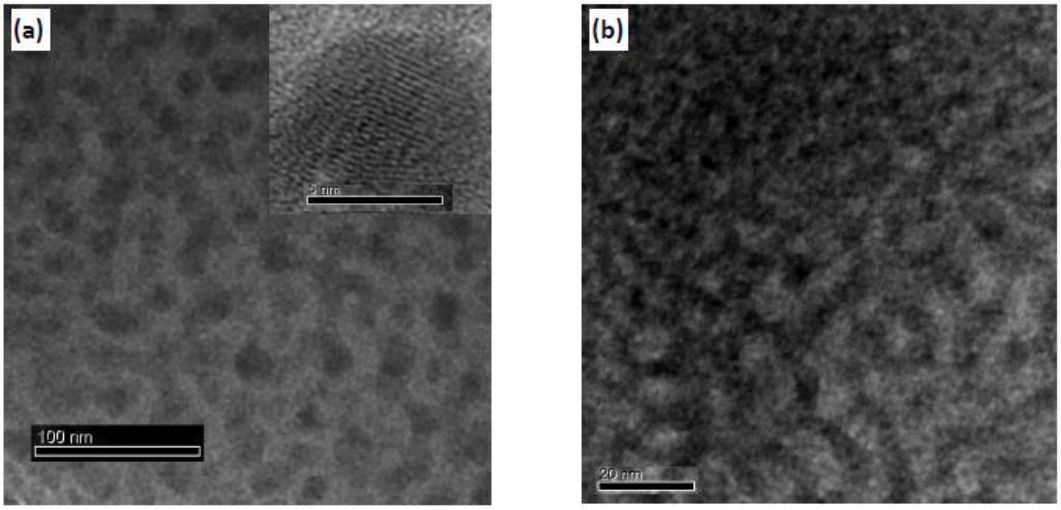

Figure 20: TEM images of GdF_3 (a) and $GdBr_3$ (b) containing glass-ceramics as presented by Han et al. (14)

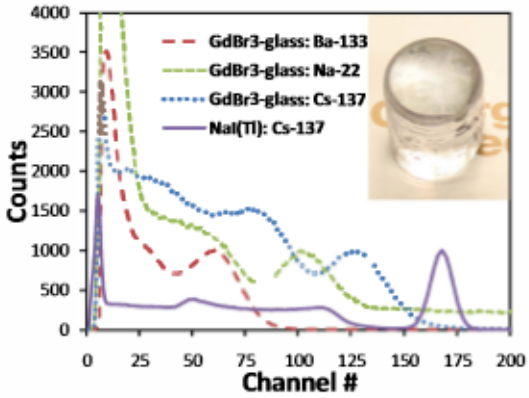

Figure 21: Gamma excitation spectra of $GdBr_3$ based glass and NaI:Tl single crystal as reported by Kang et al. (88)

2.4.2.4 $BaGdF_5$

Many fluoride based crystals have been of interest as host materials for rare earth ions due to their high transparency and low phonon energy environment. $BaGdF_5$ crystals have been proven as viable hosts for Ln^{3+} activator ions and possesses a relatively high density of $5.9g/cm^3$. (89) This high density is valuable for producing a large gamma ray absorption cross section and high gamma ray stopping power. Furthermore, Gd containing crystal systems have drawn attention due to the energy transfer capabilities between Gd^{3+} and trivalent activator ions which stands to improve the efficiency of glass-ceramics based on it. (90) A Tb^{3+} doped $BaGdF_5$ based glass ceramic was reported by Lee et al. in 2016. (34) The $BaGdF_5$ glass ceramic was synthesized from a composition of $45SiO_2$-$5Al_2O_3$-$24BaF_2$-(10-z)NaF-zCsF-$2yTbF_3$-(12-x-y)Gd_2O_3-$2xGdF_3$ where $0<x<5$, $0<y<4$, and $0<z<10$. XRD spectra confirm the nucleation of $BaGdF_5$ crystalline phase after heat treatments. The required heat treatment temperature was found to be lower for the composition where GdF_3 was included, presenting this as a valuable consideration for further investigation into this material. The estimated size of the crystalline particles was ~25-38nm with the composition that required higher annealing temperatures producing larger nanocrystals. TEM imaging presented in Figure 22: TEM image of $BaGdF_5$ nanocrystals in glass-ceramic as reported by Lee et al. confirm the presence and size of these nanocrystals. The volume fraction of the crystalline phase was reported at 33.4% which is significant, but still offers an avenue for improvement. When GdF_3 was included with the composition the produced nanocrystals were smaller in size due to the lower nucleation temperature, but the reported volume fraction was in fact greater at 37.4%, which still leaves room for improvement but further indicates the benefits of incorporating GdF_3 as a nucleating agent in the

composition. DSC measurements performed further reinforce this idea by revealing the temperature of crystallization to be lower when GdF_3 is incorporated with it decreasing from 675C to 644C.The PL spectra reported present typical Tb^{3+} emission peaks at 491, 543, 586, and 623nm under UV excitation with the intensity of these peaks increasing with increasing Tb^{3+} concentration as expected since Tb^{3+} does not tend to suffer from concentration quenching. The absorption spectra reported for this system indicate an initial absorption edge of 380nm which is already compatible with many rare earth dopants including the utilized Tb^{3+}. With the addition of GdF_3 to the constituent materials the absorption edge is reported to blue shift to 300nm indicating an improvement of the transparency further in the UV range which was attributed to either fewer defects in the glass matrix or improved nucleation of the nanocrystal phase and better index matching between the crystal phase and glass matrix. The decay time suffers as expected from the Tb^{3+} luminescence and is reported in the ms range, with a slight increase in decay time when GdF_3 is included. While this further increase in the decay time is not desired it does potentially corroborate the assertion that GdF_3 reduces the amount of defects present in the glass matrix that would cause nonradiative recombination of electron-hole pairs. While gamma ray excited spectra were not reported for this composition a qualitative comparison of the light output for the $BaGdF_5$ scintillators with and without GdF_3 inclusion was reported. When corrected for both mass and volume the GdF_3 containing $BaGdF_5$ scintillator performed better under Cs-137 and Co-60 gamma ray excitation. When compared to a purely GdF_3 based glass-ceramic scintillator the $BaGdF_5$ scintillators still outperform by both mass and volume corrected relative light output. With further investigation into the energy resolution of these materials and optimization of nanocrystal

growth $BaGdF_5$ based glass-ceramics offer a promising option for future glass-ceramic scintillator development.

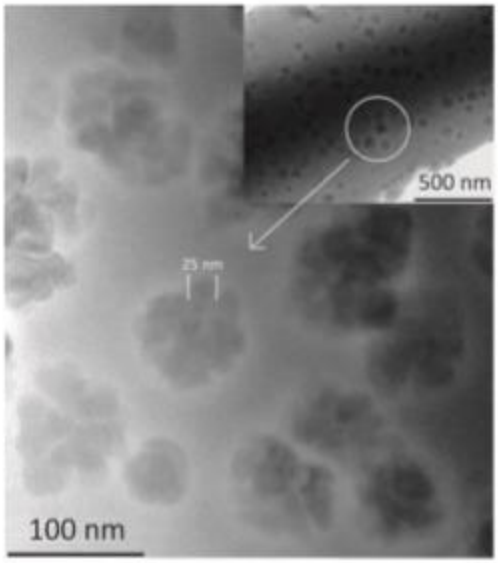

Figure 22: TEM image of $BaGdF_5$ nanocrystals in glass-ceramic as reported by Lee et al. (34)

2.4.3 Chloride Crystals

2.4.3.1 $BaCl_2$

$BaCl_2$ containing glass-ceramics have been investigated as x-ray and thermal neutron radiography phosphors recently. The glass-ceramics have shown a large PSL response due to the inclusion of both ^{10}B and ^{6}Li as neutron sensitizers which each present neutron capture reactions. (91) Such a glass-ceramic was reported by Appleby et al. in 2006 with a composition of $2B_2O_3$-Li_2O-x$BaCl_2$ where x = 0.15 – 0.75 which was doped with Eu^{2+}. (91) With 0.33 mol of $BaCl_2$ the glass was reported as unable to form crystallization through heat treatments, generating small nanocrystals when the $BaCl_2$ inclusion is increased to 0.41 mol of various phases. Increasing the $BaCl_2$ concentration further to 0.75

mol resulted in the production of largely orthorhombic $BaCl_2$ of a size near 60nm. The impact of transparency vs. crystal size and volume fraction was investigated for optimization purposes finding that while strong PSL responses could be gathered with crystallization of the orthorhombic $BaCl_2$ phase the severe loss of transparency still poses a problem for use as a storage phosphor, and would continue to cause issues in other detection applications. With greater investigation into the control of the annealing conditions to maximize PSL efficiency while maintaining transparency could provide a better candidate for X-ray imaging, but little investigation has been conducted into using these materials for scintillator detection applications.

2.5 Conclusions

With the consideration of the evidence collected above on the performance of glass-ceramic scintillators for use in detection spectroscopy applications I venture to draw the following conclusions. Of the glass ceramic systems that have been recently investigated only a select few appear poised to offer a useful alternative for use as a commercial detector material in the immediate future.

LSO glass ceramics have shown high energy spectroscopic performance similar to those of their single crystalline counterparts. However, the raw energy resolution has thus far been lacking. The high temperature of crystallization of the LSO based materials also provides slight issues in increasing production cost. The loss of transparency with increasing crystallization content is another concern for further improvement of this material.

BGO based glass ceramics have been produced with high crystalline volume fractions that possess light yields reaching 10% of that of NaI single crystals. The reported material with Eu^{3+} doping suffered from non-ideal spectral coupling for typical detection system equipment. These materials also suffered from low radiation hardnesses that much be addressed for future development. Other rare earth germanate compositions like the $LaBGeO_5$ and $GdBGeO_5$ could potentially offer options as hosts for a variety of dopant ions including Eu^{3+} and Tb^{3+} which stand to offer potential use as X-ray imaging materials.

$LiAlSi_4O_{10}$ based glass ceramics have proven to show great promise for future endeavors. There have been reports of produced materials of these compositions exhibiting greater light yield than certain commercial neutron detecting glasses. These have also demonstrated low performance dependence on temperature which is valuable for detecting applications where high temperatures are present such as well logging, and is useful in general in reducing the vulnerability of the scintillator to environmental factors. Even the undoped version of the single crystal shows some promising scintillating capabilities which could very well be improved upon through doping and further compositional tuning.

Reports of CaF_2 ceramics have shown high light yields for neutron detection but lack the transparency to be useful for detection applications. The CaF_2 glass ceramics that have been reported offer a wide variety of potential dopants that could prove useful. The cubic crystal structure of CaF_2 also means that it is a strong candidate for refractive index matching to allow for large volume crystallization of the material without harming the transparency of a glass-ceramic containing the phase.

Glass ceramics containing $BaGdF_5$ have shown promising traits as well. The $BaGdF_5$ crystal phase offers a high density system with a large halide content to provide a low phonon energy environment. This crystal system also offers the ability to host a variety of rare-earth dopants that can be tailored for different applications and system setups. The innate Gd inclusion also offers a great potential for facilitating energy transfer to the dopant activator ions which could be harnessed to improve the efficiency and light yield of the scintillator. The cubic crystal structure of this phase lends itself to refractive index matching as well which offers the potential for large volume fraction of crystalline phase without compromising transparency.

There still remain issues that must be overcome in order for us to create materials for use in commercial high energy spectroscopy applications in the near future. Firstly, glass ceramics must be produced with higher light yields in order to effectively find use in high energy spectroscopy applications. Secondly, the nucleation of high volume fractions of crystalline phase must be refined to facilitate greater light output efficiency of the activator ions without compromising the transparency of the glass-ceramic. Thirdly, the successful incorporation of proper dopants for ideal emission wavelength and decay time must be considered for the maximum coupling with detection system hardware. If these considerations are adhered to it is possible that a material could be produced that can compete with current scintillator materials at a reduced production cost.

Considering these conclusions an approach considering a few systems was identified that appears promising for our investigation into the production and optimization of glass and glass-ceramic scintillators. Of the discussed synthesis procedures the melt-quench method appears most suitable for our purposes. The melt-quench method allows for more

stable sample production than that of the sol-gel method as well as allowing for greater volume production than containerless processing. The following systems appear of greatest interest for our development. The CaF_2 crystal system shows great promise as a neutron detection scintillator through the nucleation of CaF_2 crystalline phase within a low-density oxyfluoride glass matrix. With good control of the heat treatment parameters this material could produce rare-earth doped CaF_2 nanocrystals without losing transparency. There has been little report of energy resolution measurements of this system as well which would be beneficial to the field of study. The $BaGdF_5$ crystal system offering high density, Gd^{3+} inclusion, and a cubic crystal system is very promising. With an oxyfluoride glass matrix a glass-ceramic could be designed that has the capacity to host the $BaGdF_5$ crystalline phase while maintaining its transparency. The germanate systems also provide promise through the ability to host a wide variety of rare-earth dopants. Lanthanide based borogermanates could offer a high density glass-ceramic material for good gamma ray stopping power and if designed with the stoichiometery of a crystalline phase high radiation hardness. Finally, the $LiAlSi_4O_{10}$ crystal system offers a wide variety of possibilities for both neutron detection and gamma ray detection, with the potential to provide a material that could possibly allow for the detection, and discrimination, of both simultaneously.

CHAPTER 3. CALCIUM FLUORIDE BASED GLASS CERAMIC FOR NEUTRON DETECTION

3.1 Compositional Design of CaF_2 Based Glass-Ceramic for Neutron Detection

For crystalline compositions that possess a cubic crystal structure it is possible to take advantage of the isotropy of the refractive index to increase the crystalline volume fraction without affecting the transparency of the resulting glass-ceramic. By matching the refractive index of the surrounding glass matrix to that of the precipitated crystalline phase the internal scattering due to refractive index mismatch can be eliminated, allowing for the potential of large volume fraction crystal growth and larger size crystalline precipitates without harming the transparency of the material.

Many neutron detectors still make use of materials that were first discovered in the 1950s-1970s and could benefit from innovations that have taken place more recently in the field of glass scintillators. Hot pressed CaF_2:Eu^{2+}/^{6}LiF ceramics have demonstrated great thermal neutron luminescent light yield on the order of 45,000 ph/neutron which appears incredibly promising for neutron detection. (84) However, this reported ceramic suffers from poor transparency for use as a commercial neutron detection scintillator. The thickness of these ceramics are also limited, which further compounds the issues presented by the poor transparency. The production of a glass-ceramic based on the CaF_2 crystal system could potentially offer the best of both worlds. The CaF_2 crystal possesses a cubic structure that is eligible for refractive index matching which could allow for the nucleation and growth of a large crystalline volume fraction without compromising the transparency

of the material due to scattering from the crystalline particles. For neutron detection applications a low density is more desirable than a high density due to potential noise from other incidental radiation while making neutron measurements. A silicate or oxyfluoride glass matrix could house the CaF_2 crystal phase with the potential for matching the refractive index of the CaF_2 and without increasing the density to the point where errant gamma background radiation causes interference with the detection of neutrons. LiF becomes a valuable precursor material both to contribute neutron sensitivity through the ^6Li isotope as well as having a low material density to allow for matching the refractive indices. (92) These considerations resulted in the composition of $42SiO_2$-$24Al_2O_3$-9LiF-$25CaF_2$-$0.1Eu_2O_3$.

3.2 Synthesis

The low density CaF_2:$^6Li/Eu^{2+}$ based glass ceramic for use as a neutron detection scintillator was prepared from powder precursors of CaF_2, Eu_2O_3, SiO_2, Al_2O_3, and 6LiF. Prepared compositions of $42SiO_2$-$24Al_2O_3$-9LiF-$25CaF_2$-$0.1Eu_2O_3$ were treated as per the description of the melt-quench method provided in the section Glass and Glass-Ceramic Synthesis. The melt was performed at 1400ºC for 2 hours under a purged atmosphere of inert Argon gas to prevent oxidation of the dopant ion. The cast glass samples were then annealed at temperatures between 500ºC and 650ºC in order to precipitate the CaF_2 nanocrystalline phase and obtain the full glass ceramic.

3.3 Crystallization of CaF_2 Glass Ceramic

The as-cast CaF_2 based glass ingots were heat treated at several temperatures up to 650ºC at which point the material began to lose transparency. Samples at each temperature

were ground into powder and investigated through XRD which is displayed in Figure 23: XRD spectra of heat-treated CaF_2 glass ceramic (a) and TEM image of CaF_2 nanocrystals nucleated within the glass matrix (b).a The as-cast glass shows only the amorphous broad curves typical of glassy materials between 20º-35º and 40º-55º. These broad curves remain the only features visible after annealing at 550ºC as well indicating the CaF_2 crystalline phase had not yet been nucleated. The onset of crystallization begins at 600C as demonstrated by the appearance of sharp XRD peaks in the broad glassy curves located at 29º, 46º, 55º, and 68º which are attributed to the [111], [220], [311], and [400] diffractions of CaF_2 respectively. The estimated particle size increases from 20nm to 46nm as the temperature is increased from 600ºC to 650ºC. The cloudiness of the higher anneal temperature sample is the result of increased particle size causing minor light scattering. The size of the nanoparticles is confirmed via TEM imaging of the 600ºC annealed sample which is presented in Figure 23: XRD spectra of heat-treated CaF_2 glass ceramic (a) and TEM image of CaF_2 nanocrystals nucleated within the glass matrix (b).b. The TEM image confirms the presence of spherical nanoparticles with size of 25-30nm which is close to that of the estimation from the XRD data.

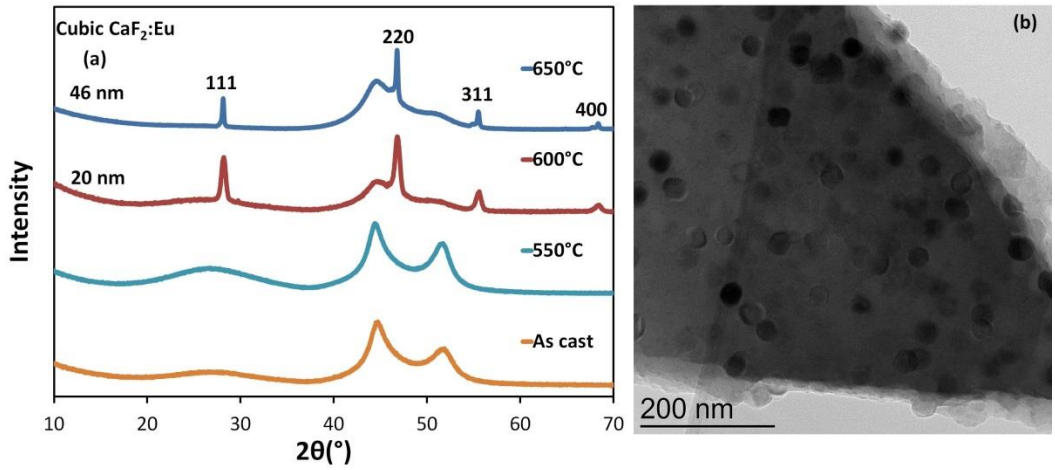

Figure 23: XRD spectra of heat-treated CaF_2 glass ceramic (a) and TEM image of CaF_2 nanocrystals nucleated within the glass matrix (b). (93)

3.4 Photoluminescence of CaF_2 Glass-Ceramic

The Eu^{2+} dopant is expected to produce a blue visible light emission in the 390-400nm range with a decay time on the order of nanoseconds. This emission range is desirable to match with the sensitive range of many PMTs currently in use in detection applications which will maximize the efficiency of the detector as a whole. The nanosecond scale decay time is desirable in order to provide the quickest possible turnaround time for the scintillator sensitivity which will result in clearer detection signals that allow for easier neutron/gamma discrimination.

Tests of the PL and PLE spectra of the produced glass-ceramic are presented in Figure 24: PL and PLE spectra of CaF_2 glass-ceramic with inset image of CaF_2 glass ceramic under 365nm UV excitation. below. The glass-ceramic shows an intense blue emission when excited under 365nm UV light as expected based on similar reports of CaF_2:Eu glass-

ceramics lacking ^{6}Li content. (20) Under excitation by 367nm incident light an emission band is observed with a maximum at 428nm. This emission is attributed to the transition between the 4f-5d bands of Eu^{2+} ions. PLE measurements observed at the 428nm emission wavelength showed an excitation band with a maximum of 377nm. This measurement is also in line with the 4f-5d transition bands of Eu^{2+} ions. The measured Stokes shift of this material is 51nm which indicates a good separation of the absorption wavelength of the material and its emission wavelength. The large Stokes shift and noted lack of PL-PLE spectrum overlap indicates that self-absorption for this glass-ceramic is negligible. Low self-absorption is desirable for scintillators as large self-absorption will greatly diminish the efficiency of the scintillator itself and thus the efficiency of the detector as a whole. Samples were prepared with doping levels greater than 0.1% to investigate the impact of greater dopant presence on the light output of the material. When the Eu_2O_3 content was raised further it resulted in an increase in the self-absorption of the material as well as causing a yellowing of the material. Both of these results indicated that an increased dopant level in this composition was detrimental and was not investigated further.

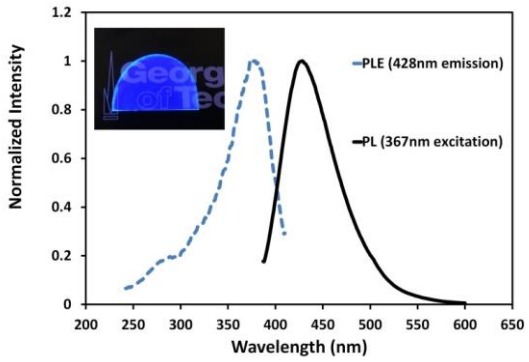

Figure 24: PL and PLE spectra of CaF_2 glass-ceramic with inset image of CaF_2 glass ceramic under 365nm UV excitation. (93)

3.5 Radionuclide Sensitivity of CaF_2 Glass Ceramic

The CaF_2 based glass-ceramic composition investigated in this chapter was designed primarily with the application of neutron detection in mind. However, the gamma detection performance of the scintillator can still provide valuable insight into the nature of the energy transfer pathway efficiency of the material. The radionuclide excitation spectra can also demonstrate how the material improves with increasing crystallinity.

Radionuclide excited photoluminescence measurements were conducted on transparent samples of CaF_2 based glass-ceramic. The samples measured 1.5mm in thickness. Measurements were taken on samples of both the as-cast, non-heat treated glass as well as on samples after post processing heat treatment anneals at 550ºC and 600ºC for four hours. Samples were excited via an Am-241 alpha source as well as a Cs-137 gamma source emitting at 662keV. The radionuclide excited photoluminescence spectra are present in Figure 25: Radionuclide excited pulse height spectra of CaF_2 based glass and glass ceramic using Am-241 alpha source (a) and Cs-137 gamma source (b).below. The as-cast glass represented by the solid black curve shows nearly negligible light output in response to

either radiation source, with the signal remaining buried in the electronic noise in the ~10 channel number region. After annealing at 550ºC the channel number of the response increases drastically and possesses a clear excitation peak. This is believed to be the result of the nucleation of very small size crystalline particles that may not have been detected by the powder XRD measurements. This appears to be confirmed following further improvement in the response of the scintillator to both radiation sources after annealing at 600ºC, where XRD confirms the presence of CaF_2 phase crystalline particles. This result confirms the hypothesis that the nucleation and growth of crystalline phase nanoparticles can be beneficial to the efficiency and overall performance of previously glass scintillators. The pulse height spectra of the annealed glass-ceramics shown in Figure 25: Radionuclide excited pulse height spectra of CaF_2 based glass and glass ceramic using Am-241 alpha source (a) and Cs-137 gamma source (b). demonstrate an increase in the light output of at least 46 times under Am-241 excitation. This factor is obtained by comparing the peak channel number for the two spectra which correlates to the light output directly through the MCA. Taking the peak of the as-cast glass to be 8, and that of the 600ºC annealed sample as 371 and taking the ratio of the two we arrive at an improvement of 46 times. Under excitation by the Cs-137 662keV gamma source we see a similar trend of improvement. There is not a visible full-energy photopeak from the Cs-137 radiation due to the small thickness of the sample as well as the low density of 2.79g/cm^3 not providing the requisite gamma ray stopping power. However, this lack of a full energy photopeak in the gamma range is a benefit for this material's use as a neutron detector. The Compton edge of the Cs-137 radiation is visible and is seen at channel 90 for the 550ºC annealed sample and

channel 170 for the 600ºC annealed sample. The Cs-137 spectrum of the as-cast glass remains in the noise region.

The low scintillation light yield of the as-cast glass is the product of several factors. Foremost, the 0.1% Eu^{2+} doping concentration is very low and as such the direct excitation of the Eu^{2+} ions in the glass matrix is very unlikely which reduces the potential light yield. This means that the light yield is highly dependent on the energy absorption and transfer from the surrounding glass matrix to the Eu^{2+} ions. The fully amorphous nature of the as-cast glass matrix results in a low incidence of energy transfer to the Eu^{2+} ions, instead favoring non-radiative recombination of electron-hole pairs in defect centers and back and forth energy transfer around the matrix. Once the glass has been annealed to form a glass-ceramic the CaF_2:Eu^{2+} nanocrystalline phase contributes to a small increase in the overall order of the glass matrix and a large increase in the order of the matrix directly surrounding the Eu^{2+} dopant ions. This leads to a much greater incidence of the adjacent CaF_2 crystalline phase successfully absorbing energy from incoming radiation and transferring that energy to the emitting Eu^{2+}. This results in a much greater light yield as the radionuclide excited pulse height spectra measurements have demonstrated. The improvement through crystallization continues with the 600ºC annealed sample due to the growth of the size of the individual crystalline nanoparticles as well as the increase in the overall crystal phase volume fraction within the glass matrix. The larger crystal size leads to a smaller surface/volume ratio which allows for a higher light emission efficiency thanks to the reduced presence of surface defects in the crystalline phase. The increased volume fraction of crystals then extends these improvements to greater portions of the material.

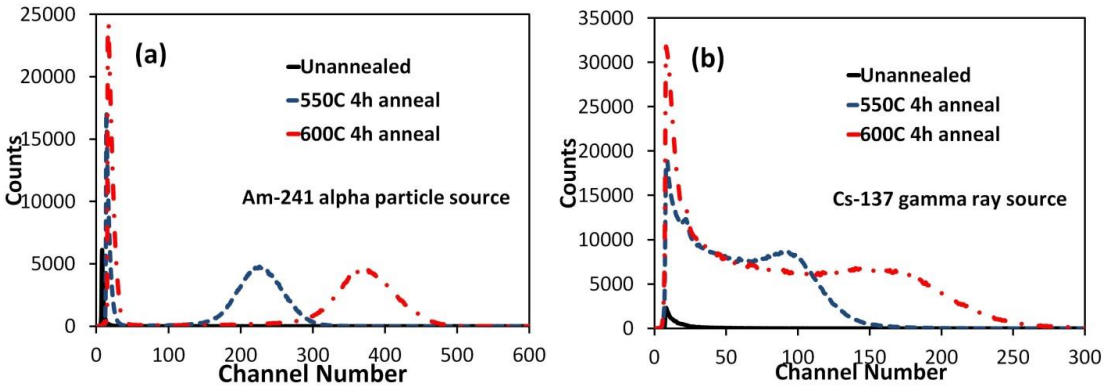

Figure 25: Radionuclide excited pulse height spectra of CaF_2 based glass and glass ceramic using Am-241 alpha source (a) and Cs-137 gamma source (b). (93)

To pursue further performance improvement of the glass-ceramic additional composition adjustments were investigated. To better facilitate a match of the refractive indices of the glass to the crystalline phase a portion of the Al_2O_3 was replaced with an amount of AlF_3 to match the total mols of Al. The resulting composition presents even greater alpha and gamma excitation responses as seen in the comparison in Figure 26: Alpha (left) and gamma (right) excited spectra comparisons of base CaF_2 glass ceramic and that with AlF_3 substitution.. This increase in light output through the composition adjustment is caused by the reduction of the refractive index of the glass to better match that of the highly fluorine based crystalline phase.

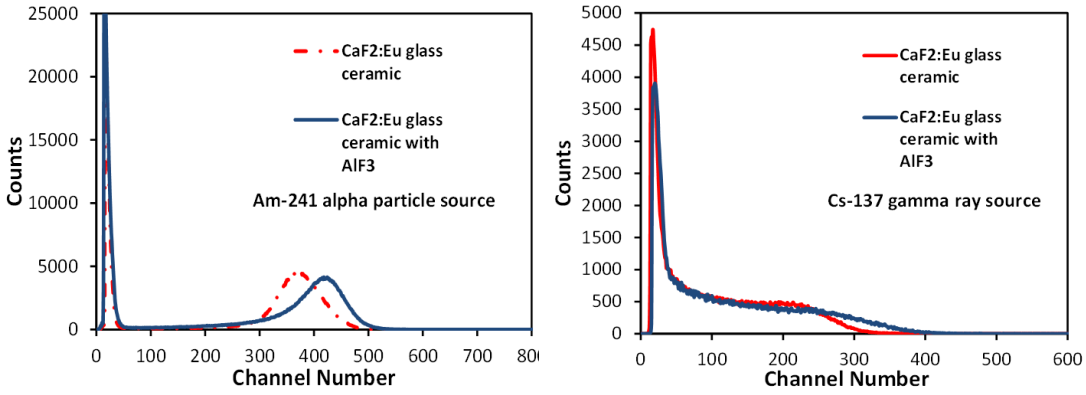

Figure 26: Alpha (left) and gamma (right) excited spectra comparisons of base CaF_2 glass ceramic and that with AlF_3 substitution.

3.6 Neutron Sensitivity of CaF_2 Glass Ceramic

The inclusion of ^6Li in the composition of this glass-ceramic enables the detection of thermal neutrons due to the large neutron sensitivity cross section provided by the ^6Li. The $^6Li(N, \alpha)$ reaction results in the emission of an alpha particle which can then interact with the dopants in the glass matrix as we have already demonstrated with the measurements conducted with the Am-241 point source. This neutron interaction is the basis upon which the $CaF_2:Eu^{2+}$ glass-ceramic may act as a neutron detection scintillator.

Neutron excited pulse height spectrum measurements were conducted with a PuBe neutron source encased in a polyethylene cylinder in order to restrict the emitted neutrons to thermal energies. A typical neutron pulse height spectrum is presented in Figure 27: Typical neutron pulse height spectrum of CaF_2 based glass-ceramic. below. This material presents a clear neutron induced photopeak occurring at channel number 12,250. A Gaussian fit was applied to the photopeak and an energy resolution of 15.9% was calculated. A quantitative comparison was made between the measured spectra of the

produced $CaF_2:Eu^{2+}$ glass ceramic and a known commercial neutron scintillating glass GS20, which is a Ce^{3+} activated glass scintillator. The light output of the 600ºC annealed CaF_2 glass ceramic scintillator is equivalent to 70% of the output of the GS20 scintillator. The known light output of the GS20 scintillator is ~8,000 ph/neutron, which gives a light output of ~5600 ph/neutron for the produced CaF_2 glass-ceramic. This calculated light yield would not be considered a high light yield in the field of neutron or gamma detection applications, but as of yet there are no efficient Eu^{2+} doped glass neutron scintillators on the market.

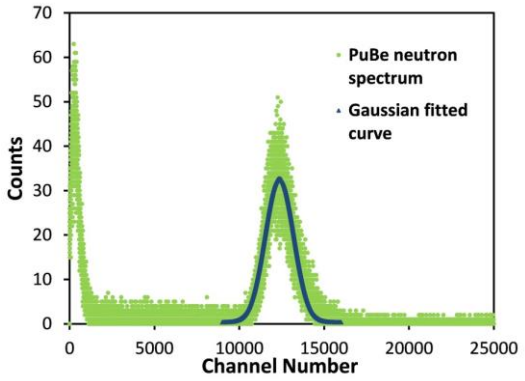

Figure 27: Typical neutron pulse height spectrum of CaF_2 based glass-ceramic. (93)

3.7 Conclusions

The compositional design of the $CaF_2:Eu^{2+}$ glass-ceramic has performed in line with the expectations of the predicted performance of the chosen materials. The low density of the CaF_2 based oxyfluoride glass matrix adequately allowed for minimal interference from gamma radiation as is desired for a neutron detection scintillator. The inclusion of ^6Li in the form of ^6LiF was successful in providing a good neutron sensitivity cross section which reacted to and allowed for the detection of thermal neutrons. The glass matrix allowed for

the nucleation and growth of the CaF_2:Eu^{2+} nanocrystalline phase as predicted in the design of the composition. The choice of dopant in Eu^{2+} was successfully incorporated within the glass matrix in the proper valence without undergoing detrimental oxidation and provided brilliant blue luminescence with an adequate decay time and appropriate emission wavelength for coupling with a PMT to form a detector system.

The investigation of this system gives concrete evidence that the nucleation and growth of crystalline phase nanoparticles is a valid route for increasing the efficiency and light output. By developing a composition in such a way that promotes the growth of the CaF_2:Eu^{2+} crystalline phase in nanoscale particle sizes the scintillation response to both alpha radiation and gamma radiation was greatly improved by a factor of at least 46 times. For base glass matrix compositions that can be successfully cast in stoichiometric compositions representative of known crystal phases this provides a route to scintillation improvement with little additional consideration once the temperature of crystallization onset has been determined. While it was hypothesized that the aluminosilicate based glass matrix would be sufficient to index match the crystalline phase to the glass matrix the heat treatment testing and XRD confirmation of the crystalline phase indicate that this is not the case as the material began suffering transparency loss at larger grown particle sizes and volume fractions. The adjustment of the glass composition to better match with the refractive index of the crystalline phase was also successful in improving the light output of the designed material which falls in line with the expected principles of refractive index matching for crystals with cubic structure.

The current performance of this composition approaches 70% of that of a known commercial glass scintillator already implemented in neutron detection applications. While

the light output is not quite optimal for competition at the commercial scale currently this short development time produced a glass-ceramic scintillator of comparatively small size that already approaches the performance of available commercial products. This is a promising result for future applications. With additional composition and processing optimization this composition could effectively provide an alternative option in neutron detection applications.

CHAPTER 4. BARIUM GADOLINIUM FLUORIDE BASED GLASS-CERAMIC

4.1 Composition Design of $BaGdF_5:Ce^{3+}$ Glass-Ceramic

The $BaGdF_5$ crystal system meets all of the criteria for a promising option as a gamma ray detecting glass-ceramic scintillator: The Gd and Ba content provides high density and high Z number material to facilitate a high gamma ray stopping power. The Gd content also offers energy transfer capabilities to dopant activator ions such as Ce^{3+}, Eu^{2+}, and Tb^{3+} which is valuable for potentially increasing the efficiency of these dopants. A large F content helps promote a low phonon energy environment to improve the efficiency of the incorporated dopant activator ions. The cubic crystal structure that $BaGdF_5$ possesses makes the material isotropic and allows for refractive index matching to minimize scattering caused by nucleated crystalline particles. Finally, the $BaGdF_5$ crystal system supports Ce^{3+} doping which provides the ideal luminescence wavelength to match the high sensitivity region of a typical PMT used in detection systems, as well as a fast luminescent decay time to enable the detection of fast gamma ray events.

In the previous work of my research group at the Georgia Tech Research Institute G. Lee investigated a starting point of a $BaGdF_5$ based glass ceramic doped with Tb^{3+} which was reported in 2016. (34) At that time Tb doping was of interest due to its high quantum efficiency resulting from the quantum cutting effect that could allow for the scintillator to produce a greater number of visible light photons in response to the same energy of gamma ray excitation. While Tb^{3+} does allow for a strong luminescent response, the poor match to

PMT sensitivity regions along with the slow decay time of Tb^{3+} made it a poor match for gamma ray detection applications. Through the previous research a base system of $45SiO_2$-$5Al_2O_3$-$24BaF_2$-$(10-z)NaF$-$zCsF$-$2yTbF_3$-$(12-x-y)Gd_2O_3$-$2xGdF_3$ was produced and investigated for $0<x<5$, $0<y<4$, and $0<z<10$. The main point of interest this studied uncovered comes from the incorporation of GdF_3 into the composition of this glass-ceramic system. For the absorption spectra the incorporation of GdF_3 leads to a blue-shift of the absorption edge, which was interpreted as a reduction in defects in the glass or potentially an improvement in the index match of the glass-ceramic. The incorporation of GdF_3 also led to a slight increase in the decay time of the glass-ceramic, potentially an additional indicator of a decrease in the concentration of defects within the glass-ceramic. However, the point of greatest importance was determined through XRD measurements which found that inclusion of GdF_3 in the glass composition led to a reduction of the temperature required to nucleate the $BaGdF_5$ crystalline phase from 700ºC to 600ºC for equivalent annealing time periods. On top of the temperature reduction allowing easier production of the glass-ceramic it was also found that the composition with added GdF_3 exhibited fewer additional contaminant phases after heat treatment and produced a greater volume fraction of the $BaGdF_5$ phase. These results indicate that the incorporation of GdF_3 into the composition of a $BaGdF_5$ based glass-ceramic is of great interest.

To support the nucleation of the $BaGdF_5$ crystalline phase an aluminosilicate based glass matrix was investigated. Glass matrices that are largely silicate have been shown to support the incorporation of high concentrations of rare earth materials which is critical for the increase of the density of the glass-ceramic. Aluminosilicate glasses can also support the high halide content desired to facilitate the desired crystalline phase and provide a lower

phonon energy environment to improve the efficiency of the dopant activator ions. While at the time of development the index of refraction of $BaGdF_5$ was not yet widely reported in the literature it was expected to be between that of BaF_2 (n=1.48) and GdF_3 (n=1.59) which an aluminosilicate matrix provides a strong starting point in tuning to index match. (32) The incorporation of GdF_3 is also considered as a possible catalyst for easier nucleation of the target crystalline phase. These considerations resulted in a composition of $45SiO_2$-$5Al_2O_3$-$24BaF_2$-$11Gd_2O_3$-10NaF-$4GdF_3$-$2CeF_3$ in mol%.

4.2 Synthesis of $BaGdF_5:Ce^{3+}$ Glass-Ceramic

Powder precursors of SiO_2, Al_2O_3, BaF_2, Gd_2O_3, NaF, GdF_3, and CeF_3 were combined, mixed to homogeneity, and loaded into an Al_2O_3 crucible in accordance with the established melt-quench procedure. The sample crucible was then loaded into a furnace heated to 1500ºC for 2.5 hours under a reducing Ar-CO atmosphere. After the melt stage was completed the crucible was removed from the furnace and the melt quenched in a graphite mold preheated to 400ºC. After casting the samples were annealed at 500ºC for 6 hours to relieve internal stress. Cast samples were heat treated at 600ºC for 6 hours to promote the nucleation and growth of the $BaGdF_5$ crystalline phase.

4.3 Optimization of $BaGdF_5:Ce^{3+}$ Glass-Ceramic Composition

Previous investigation of similar $BaGdF_5$ based glass-ceramics resulted in compositions that showed promise but did not possess ideal detection capabilities for use in gamma ray detection applications. One facet of the previous design which could be improved is the temperature at which the material undergoes nucleation of the $BaGdF_5$ phase. In our literature previously published in *Nanotechnology* we touched on the

possibility of reducing the required nucleation temperature through the addition of GdF_3 to the composition. (34) In this research the optimization of this material was pushed further through a number of tuning approaches.

Analysis began with the composition listed in the design section of this chapter. Samples of this composition were processed and investigated for scintillation characteristics. PL and PLE measurements of this composition are presented in Figure 28: PL and PLE measurements of the base $BaGdF_5$ composition. The photoluminescence response presents peaks at 375nm and 320nm for the PL and PLE spectra respectively. This response is typical of transparent glass materials doped with Ce^{3+} and is attributed to the 4f-5d transition in Ce^{3+}. The samples present little self-absorption which is ideal for detection applications. Luminescent decay measurements for this initial composition are presented in Figure 29: Luminescent decay time measurements of base $BaGdF_5$ composition.. The decay spectrum presents a luminescent decay that appears to operate under two separate mechanisms. The initial fast mechanism which is likely provided from the direct relaxation of the Ce^{3+} ions possesses a decay time of 45ns which is typical of Ce^{3+} luminescence and beneficial for gamma ray detection applications. The second mechanism likely stems from some slight afterglow and a longer relaxation of the surrounding glass matrix results in a decay time of 474ns, but only takes over at 1% of the initial pulse intensity, which minimizes its negative contribution to the luminescence. Absorption measurements of this composition show a strong absorption edge at 370nm. While this is a much longer absorption edge wavelength than the Tb based material it does not quite reach the emission peak position of the luminescence which is positive for minimizing self-absorption. Luminescent brightness was measured between the new Ce

doped composition and the previously investigated Tb doped composition under X-ray excitation energy of 60kVp. The Tb doped composition shows a much greater brightness than the Ce doped composition, but for gamma ray detection purposes Ce is still the preferred dopant for its much faster decay time.

To provide a baseline of gamma detection spectra a series of gamma ray excited pulse height spectra were obtained from Co-57, Ba-133, Na-22, Cs-137, Mn-54, Zn-65, and C0-60 gamma radiation point sources which possess decay energies of 122keV, 356keV, 512keV, 662keV, 835keV, 1.1MeV, and 1.3MeV respectively. The collected spectra for this composition are presented in Figure 30: Gamma ray excited pulse height spectra of the base $BaGdF_5$ composition.. As demonstrated there are no fully resolved full energy photopeaks detected for the utilized nuclide point sources. All source spectra resemble broad unresolved shoulders not fully separated from the Compton continuum. The energy resolution was calculated from the Cs-137 spectrum and found to be 19.5%. As the previous Tb doped composition that was reported only featured relative brightness measurements for two gamma sources this still provides a valuable basis for the judgement of future developments in $BaGdF_5$ glass-ceramic scintillators. However, for commercial applications the gamma detection capabilities and energy resolution of this composition must be drastically improved as the lack of defined photopeaks renders it impossible for detection systems to properly identify the detected sources.

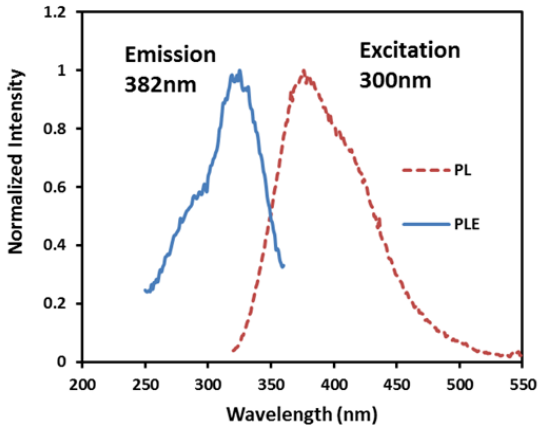

Figure 28: PL and PLE measurements of the base $BaGdF_5$ composition.

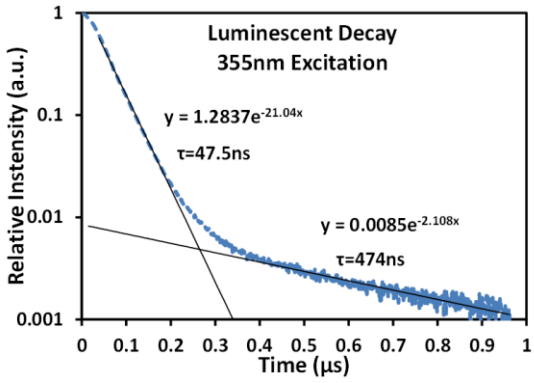

Figure 29: Luminescent decay time measurements of base $BaGdF_5$ composition.

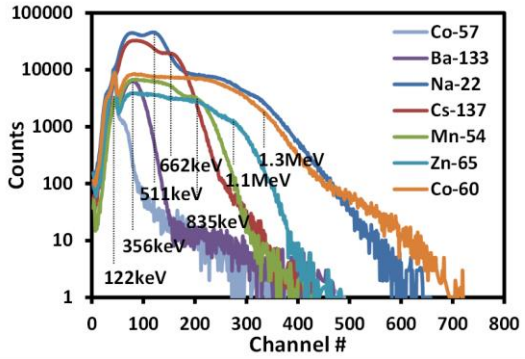

Figure 30: Gamma ray excited pulse height spectra of the base $BaGdF_5$ composition.

4.3.1 Density Tuning of $BaGdF_5:Ce^{3+}$ Glass-Ceramic

To improve the gamma ray detection response of the $BaGdF_5:Ce^{3+}$ glass-ceramic the main direction taken was to improve the density of the material. Through promoting a greater material density the scintillator will gain greater gamma ray stopping power which will allow for the complete discrimination of the full energy photopeaks of the radionuclide point sources. To accomplish this feat a number of precursor material substitutions were made: Al_2O_3 was replaced with Gd_2O_3 to incorporate additional high density Gd while still maintaining adequate oxide precursors to form the supporting glass matrix; NaF was replaced with CsF to increase density while maintaining the fluoride content of the material; and GdF_3 was replaced with $GdBr_3$ to attempt to incorporate Br into the glass matrix which fills a similar role to F in the contribution to a low phonon energy environment but to a greater effect. These changes resulted in a composition of $44SiO_2$-$24BaF_2$-$14Gd_2O_3$-10CsF-$4GdBr_3$-$4CeF_3$.

Samples of this composition were prepared at 1500ºC for 2.5 hours under an N-H atmosphere and were quenched to 400ºC. The samples were then annealed at 500ºC for 6 hours to relieve internal stress. The measured density of the newly prepared composition was determined to be 4.18g/cm^3, roughly equivalent to the density of the initial composition. The incorporation of higher density materials was logically sound, but the small overall content of this higher density material was not significant enough to affect a large change in the overall scintillator density.

PL measurements made on this updated composition shown in Figure 31: PL/PLE of $BaGdF_5$:Ce sample with stopping power adjustments. present a redshifted emission now

residing at 415nm compared to 375nm from the original composition. PLE measurements depict a similar redshift from 320nm to 345nm. This is most likely caused by the alteration of the glass matrix that resulted from the precursor substitutions. In particular, the substitution of Al_2O_3 with Gd_2O_3 could cause both a change in the surrounding matrix for the Ce dopant ions in addition to greater transfer from Gd to Ce altering the emission wavelength.

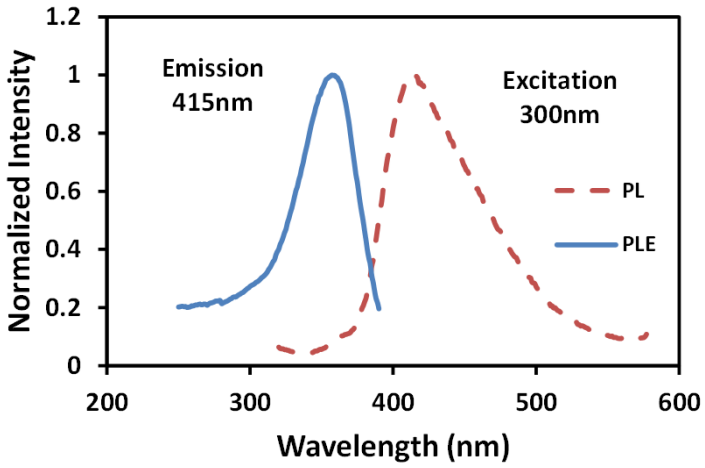

Figure 31: PL/PLE of $BaGdF_5$:Ce sample with stopping power adjustments.

Decay time measurements were conducted on this composition with Cs-137 source 662keV gamma ray excitation which are presented in Figure 32: RL excited decay time measurement of $BaGdF_5$:Ce sample with stopping power adjustments. below. The decay time for gamma excited luminescence shows an increase to 379ns compared to the UV stimulated decay time discussed previously. The excitation pathway for gamma ray induced luminescence appears to utilize more of the secondary decay mechanism than the primary decay mechanism, likely due to a greater reliance on energy transfer from the Gd present within the glass matrix.

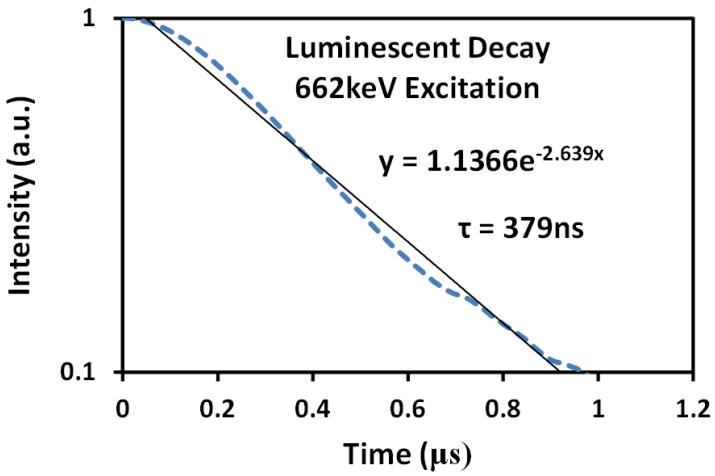

Figure 32: RL excited decay time measurement of $BaGdF_5$:Ce sample with stopping power adjustments.

Gamma excited pulse spectra of this updated composition were collected with Ba-133, Cs-137, and Mn-54 sources and presented in Figure 33: Gamma ray excited pulse height spectra of $BaGdF_5$ based composition tuned for stopping power.. While the compositional adjustments did not significantly alter the density of the material the added high Z number elements in the adjustments were effective at increasing the stopping power of the scintillator as indicated by the more fully resolved full energy photopeaks present in the gamma excited pulse height spectra. Of the three sources used all gamma spectra show fully resolved peaks separated from the Compton continuum which presents an already drastic improvement of the gamma detection quality of this new composition. The energy resolution calculated from the Cs-137 spectrum was determined to be 16.1%. This is still far from the target energy resolution, but it is a significant improvement over the starting composition.

Post processing heat treatments were attempted on this new composition in order to nucleate and grow the crystalline phase. However, it was found that this adjusted composition no longer exhibited XRD peaks after heat treatments as high as 750ºC. It was believed that the substitution of GdF_3 with $GdBr_3$ would improve the stopping power and low phonon energy environment without compromising the nanocrystal nucleation content. However, while the Gd content was held constant the amount of F was diminished through the Br substitution, and despite both of these being halide elements the loss of F content appears to have negatively impacted the $BaGdF_5$ nucleation capabilities of this composition.

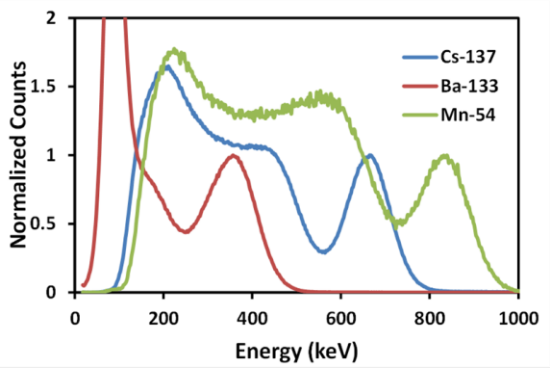

Figure 33: Gamma ray excited pulse height spectra of $BaGdF_5$ based composition tuned for stopping power.

4.3.2 Reintroduction of GdF_3

The gamma detection improvement gained from the substitution of $GdBr_3$ for GdF_3 was promising, but still insufficient on its own. In order to push the performance of the material even further we re-examine the inclusion of GdF_3 by substituting a portion of the Gd_2O_3 with GdF_3. Considering the previous work with this system it is expected that GdF_3 is a nucleation agent of the $BaGdF_5$ crystalline phase in this glass system. This adjustment

results in a composition of $44SiO_2$-$24BaF_2$-$10CsF$-$10Gd_2O_3$-$8GdF_3$-$4GdBr_3$-$4CeF_3$. Samples of this composition were prepared in the same manner as the previous composition.

The density of samples produced by this new composition was measured to be $4.33g/cm^3$. While no major intentional changes were made to this composition for density increases compared to the previous composition there still remains a possible explanation in the substitution of GdF_3 for Gd_2O_3. During the melt phase there is the possibility that a portion of the halide materials burn off and are not incorporated into the final material, but oxides do not tend to demonstrate this level of volatility. It is possible that by replacing a portion of the oxide with fluoride a final product was produced with a higher loading level of high density Gd compared to the lower density glass matrix formers.

PL measurements taken for this updated composition are presented in Figure 34: PL/PLE measurements of $BaGdF_5$:Ce samples with additional GdF_3.. Under 300nm excitation a blue-shifted emission peak is observed compared to the previous composition now appearing at 409nm. The addition of GdF_3 was shown to blue-shift absorption peaks in previously reported Tb doped compositions, but did not affect the PL emission peak position. However, due to the lack of shielding of Ce^{3+} energy levels compared to Tb^{3+} it is possible that the increase in GdF_3 content is the cause of the slight emission peak shift. Luminescent decay time measurements were once again taken with 662keV Cs-137 excitation for this updated composition. The decay time presented in Figure 35: Decay time of $BaGdF_5$:Ce sample with additional GdF_3. was measured to be 430ns for this updated composition, slower than the previously discussed compositions. The increase in the decay time follows the idea that the luminescent emission pathway is relying heavily on the

energy transfer from Gd^{3+} to Ce^{3+}, and is a further indication of the increase in relative Gd loading in the glass matrix.

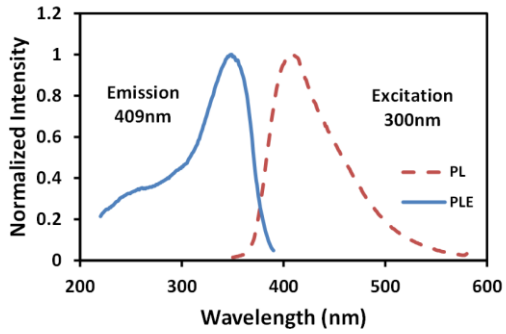

Figure 34: PL/PLE measurements of $BaGdF_5$:Ce samples with additional GdF_3.

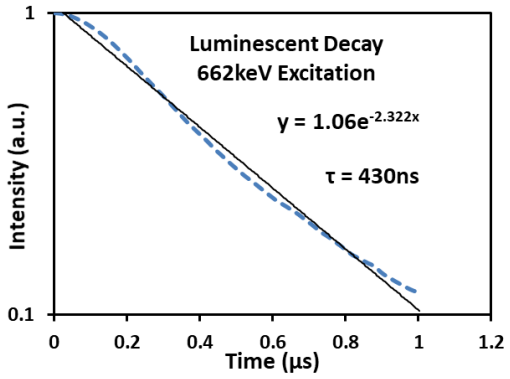

Figure 35: Decay time of $BaGdF_5$:Ce sample with additional GdF_3.

Gamma ray excited pulse height spectra of this composition are presented in Figure 36: Gamma ray excited pulse height spectra of $BaGdF_5$ based glass after GdF_3 reintroduction. below for the full series of Co-60, Ba-133, Na-22, Cs-137, Mn-54, Zn-65, and Co-57 sources. The energy resolution of the Cs-137 peak was calculated to be 15.4%. This is still not an ideal energy resolution for commercial use, but it is a significant improvement from the initial 19.5% with a marked improvement in the ability to fully resolve the full energy photopeaks of the radionuclides. The discrimination of the secondary energy peaks for Na-

22 and Co-60 also becomes possible with this newest composition, indicating a strong improvement in the energy absorption capabilities of the scintillator. The light yield of this final composition was estimated through comparison of the Cs-137 gamma excitation spectrum for the $BaGdF_5$ based glass to a commercial NaI:Tl single crystal scintillator. The light yield of this scintillator was calculated to be 3460 ph/MeV. While this is still short of the values of typical commercial scintillators it is an impressive magnitude for a glass scintillator.

Samples of the final composition were investigated for improved crystallization capabilities after reincorporation of GdF_3. After heat treatment at 750ºC for 6 hours samples were obtained with full opacity caused by crystallization and were investigated via XRD. The XRD spectrum presented in Figure 37: XRD spectrum of final $BaGdF_5$ based composition after heat treatment at 750ºC for 6 hours. below indicates the possible presence of the $BaGdF_5$ crystalline phase, along with some additional unidentified peaks similar to those shown in the original Tb doped composition. Samples prepared with heat treatments retaining the maximum transparency do not show any improvement in scintillation performance for this system. It is possible that at temperatures low enough to retain transparency it is no longer possible to nucleate a significant volume fraction of the $BaGdF_5$ phase. It is also possible that this unidentified crystalline phase is compromising the benefits of forming a glass-ceramic of this system.

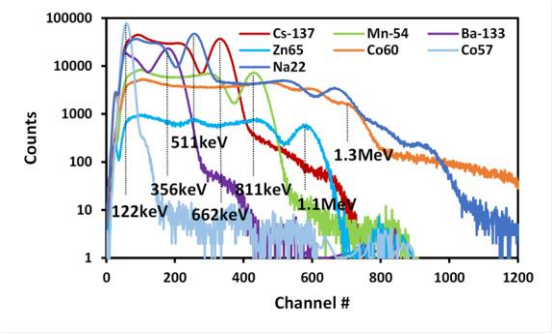

Figure 36: Gamma ray excited pulse height spectra of $BaGdF_5$ based glass after GdF_3 reintroduction.

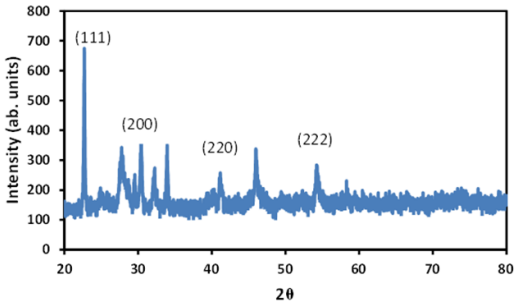

Figure 37: XRD spectrum of final $BaGdF_5$ based composition after heat treatment at 750°C for 6 hours.

4.4 Conclusions

The compositional design principles continue to show expected performance improvement capabilities through the production of a gamma ray detecting glass-ceramic based on the composition of the $BaGdF_5$ crystalline phase. This composition was identified for its cubic crystalline structure that possesses optical isotropy alongside the innate inclusion of high-density, high-Z number element Gd which is attractive for gamma ray detection applications. This composition successfully formed a transparent glass material which supported a nucleated phase of crystalline nanoparticles as was accomplished with the previous composition.

Compositional tuning of the material was proven to be successful for targeting specific facets of the scintillator capabilities in need of improvement. The addition of greater amounts of high stopping power material in the form of Gd_2O_3, GdF_3, $GdBr_3$, and CsF was successful in enhancing the ability of the scintillator to fully absorb incoming gamma radiation to better discriminate the full-energy photopeaks of the radiation sources, thus bolstering its performance. This study also reinforces the potential for the incorporation of GdF_3 in materials where it is a possible constituent to encourage the nucleation of crystalline phases dependent on gadolinium fluoride complexes. The incorporation of greater amounts of halide based precursors over oxides was also shown to improve the energy resolution through improving the homogeneity of the melt by increasing the fluxing agent and decreasing the overall melting temperature of the mixture as well as improved loading of Gd relative to the remaining lower density glass matrix after the melt.

This study also presented a factor to keep in mind for future compositional tuning experiments involving the incorporation of large quantities of rare-earth materials. Due to the nature of the larger size of the rare-earth ions increasing the quantity of these components can have a negative effect on the ability of the glass matrix to support the nucleation of the crystalline phase due to limited locomotion capabilities of these rare-earth ions. In the case of this composition this negative impact was mitigated by the reintroduction of GdF_3, but this still did not bring the crystallization temperature down to its original point. The stoichiometry of the desired crystalline phase must also be considered in tuning to ensure substitutions made do not render crystallization unlikely due to a lack of the supporting elements of the crystalline phase such as F in this case. A balance

must be struck between the incorporation of high performance materials and the ability to nucleate the crystalline phase for maximum performance.

CHAPTER 5. LANTHANUM BOROGERMANATE BASED GLASS

5.1 Composition Design of $LaBGeO_5$ and $GdBGeO_5$ Based Glass

The $LaBGeO_5$ and $GdBGeO_5$ have long been investigated for features such as their wide IR transmittance and high refractive index. (94) These borogermanate glass and glass-ceramic systems present strong promise due to the much higher density offered by the innate Ge content as well as the ability to support large amounts of lanthanide group elements such as La and Gd to further increase the density and gamma ray stopping power of the scintillator as compared to the lower density silicate and fluoride based glasses and glass-ceramics that have been recently investigated. Additionally, heavy metal oxides such as GeO_2 have been shown to possess high radiation hardness which provides a great benefit for the lifetime of the scintillator. (42) Germanate glasses have been reported to benefit from a lower maximum vibrational frequency than silicate, phosphate, and borate glasses which offers the potential to improve the efficiency of the dopant activator ions incorporated into the scintillator. (60) The Gd component offered by $GdBGeO_5$ has also been shown to allow for direct energy transfer to certain trivalent activator ions within glass matrices. Rare earth borogermanates, including the crystalline form of $LaBGeO_5$, have proven to be suitable hosts for many dopant ions such as Eu^{3+}, Tb^{3+}, and Tm^{3+} which provides options for adjusting to application requirements. (61) However, $GdBGeO_5$ has only been confirmed as a suitable host for Eu^{3+} and Tb^{3+}. Scintillators and phosphors doped with Tb^{3+} have already been utilized well in industrial and medical imaging applications where the slower decay time of Tb^{3+} luminescence is not as detrimental to the performance

as it would be in fast gamma detection applications. (56) Efficient Tb^{3+} doped glasses and glass-ceramics could also find use in these applications as well as potentially finding use in MeV portal imaging applications. In addition Tb^{3+} is incredibly resistant to oxidation during synthesis, allowing us to forgo the reducing atmosphere that is required for other more vulnerable dopants and potentially lowering production costs further. A glass produced with the corresponding stoichiometric composition to the $LabGeO_5$ or $GdBGeO_5$ crystal systems could support a high volume fraction of nanocrystals for greater light output improvement and therefore could be a strong candidate as a glass-ceramic scintillator. However, these crystalline phases do not possess a cubic structure and as such any nucleated crystalline particles must be controlled in such a manner to keep the particles in the nanosize region to minimize any potential light scattering. These considerations resulted in two compositions. For the $LaBGeO_5$ composition a formula of $50GeO_2$-$25B_2O_3$-$(25-x)La_2O_3$-$(x)Tb_2O_3$ in mol% was considered where x possesses values of 1, 2, 3, and 4. The changes in Tb concentration are utilized to search for the ideal Tb^{3+} concentration for maximum light output. The composition was designed with Tb_2O_3 in mind, but for production Tb_4O_7 was utilized at half the amount listed for Tb_2O_3. A second composition was developed parallel to the above for $GdBGeO_5$ by substituting Gd_2O_3 for La_2O_3 in order to investigate the impact of the higher density and energy transfer capabilities offered through Gd. The lanthanum borogermanate samples will after this point be referred to as LBGT (1-4) according to the Tb content. Similarly the gadolinium borogermanate glass samples will be referred to as GBGT (1-4).

5.2 Synthesis of Lanthanum and Gadolinium Borogermanate Glass

Powder precursors of the materials listed in the Compositional Design section were combined, mixed to homogeneity, and loaded into the furnace in accordance with the melt-quench synthesis steps detailed in the introduction section of this paper. The purity and source of these powder materials are as follows: GeO_2 (Acros Organics, 99.999%), B_2O_3 (Alfa Aesar, 99.98%), La_2O_3, (Cerao, 99.99%), Gd_2O_3 (Alfa Aesar, 99.9%), and Tb_4O_7 (Alfa Aesar, 99.9%). Samples were melted at 1250ºC for 2.5 hours in an argon atmosphere. Once melted the crucible was removed from the furnace and the melt quenched into a graphite mold preheated to 400ºC and allowed to cool to room temperature. Once cooled the material was then annealed at 500ºC to relieve internal stresses. Additional pieces of the glass samples were annealed at temperatures ranging from 600-900ºC to investigate the crystallization behavior of the glass.

5.3 Characterization and Optimization of Borogermanate Glasses

5.3.1 Photoluminescence and Photoluminescence Excitation

Photoluminescence spectra were collected for the LBGT and GBGT glass compositions under 274nm excitation and are presented in Figure 38: PL measurements of gadolinium borogermanate glass (a) and lanthanum borogermanate glass (b) under 274nm excitation. Inset images show samples of 1-4% Tb doping under 365nm UV lamp excitation.. In both cases the results are typical of the green emission lines associated with the internal orbital transitions of Tb^{3+} doping. The peaks at 489, 543, 585, and 622nm are attributed to the $^5D_4$-^7F_J (J = 6,5,4,3) optical transitions of Tb^{3+}. (66) (95) (96) These Tb^{3+} emissions are seen to increase in intensity with an increase in Tb^{3+} doping concentration

with no indication of concentration quenching as is a concern with other dopants such as Ce^{3+}. The inset graphs depict a magnified view of the 350-450nm sections of the PL spectra depicting a smaller set of peaks corresponding to the $^5D_3$-^7F_J (J = 5,4,3) transitions. These secondary transitions decrease in intensity with additional Tb^{3+} doping which is attributed to cross-relaxation in Tb^{3+}. (97) (98) (99) The $^5D_3$ transition peaks in the GBGT series are initially buried under a broader Gd^{3+} emission band. (15) At low Tb^{3+} concentration the Gd^{3+} band is at its largest intensity, but the drastic decrease in intensity of the Gd^{3+} band with increasing Tb^{3+} concentration indicates the possibility of energy transfer between the Tb^{3+} and Gd^{3+} ions. The $^5D_3$ Tb^{3+} peaks are well defined at 2% Tb^{3+} but lose clarity at higher concentrations likely due to the same quenching that occurs in the LBGT samples.

The relative PL emission intensity for the GBGT and LBGT samples under 365nm excitation are presented and compared in Figure 39: PL emission intensity comparison of the GBGT and LBGT series samples with Tb^{3+} concentration.. Both compositions show increase in emission intensity with increasing Tb^{3+} concentration with no reduction in the rate of increase, further indicating that this composition has not yet reached dopant levels that could cause concentration quenching. Additionally it is seen that at all doping concentrations the GBGT samples produce greater luminescence than their LBGT counterparts. In this experiment the Tb^{3+} emission was directly activated through excitation at 365nm which is identified in the PLE spectra. While we have discussed the potential for energy transfer between Gd^{3+} and Tb^{3+} in the GBGT compositions this is not likely the cause for this difference in PL emission. As a result, this disparity in luminescent emission is more likely the result of the GBGT compositions containing fewer non-radiative

structural defects as compared to the LBGT compositions leading to a greater luminescent efficiency.

The PLE spectra of two of the LBGT and GBGT samples gathered through monitoring the emission wavelength of 544nm are presented in Figure 40: PLE spectra of the borogermanate glasses at 2% Tb^{3+} doping.. Both samples exhibit the highest excitation peak at 372nm which is attributed to the $^7F_6$-$^5D_3$ transition in Tb^{3+}. The lower intensity peaks present at 352nm and 490nm are attributed to the $^7F_6$-$^5L_9$ and $^7F_6$-$^5D_4$ transitions in Tb^{3+} respectively which have been reported from crystalline materials and are consistent with the conducted absorption measurements. (89) (96) (100) (101) The LBGT sample shows an additional peak at 315nm which is attributed to the $^7F_6$-$^5D_1$ transition in Tb^{3+} and is also supported by the absorption measurements of the LBGT series. (89) The GBGT sample shows an additional two distinct peaks not present in the La based series at 274nm and 313nm that are attributed to the $^8S_{7/2}$-^6I_J and $^8S_{7/2}$-$^6P_{7/2}$ transitions in Gd^{3+} which indicates an energy transfer mechanism between the Gd^{3+} and Tb^{3+} ions. (63) (96) (102) (103) The lack of overlap between the PL and PLE spectra demonstrates little self-absorption which is important for scintillation applications.

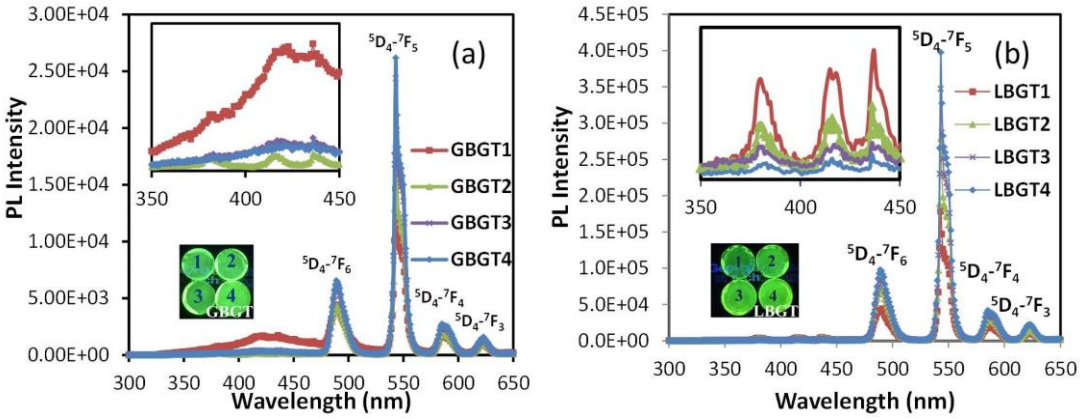

Figure 38: PL measurements of gadolinium borogermanate glass (a) and lanthanum borogermanate glass (b) under 274nm excitation. Inset images show samples of 1-4% Tb doping under 365nm UV lamp excitation. (104)

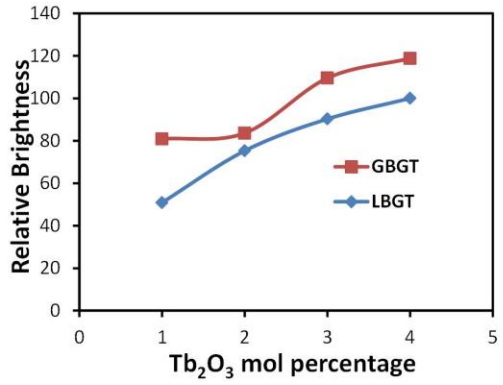

Figure 39: PL emission intensity comparison of the GBGT and LBGT series samples with Tb^{3+} concentration. (104)

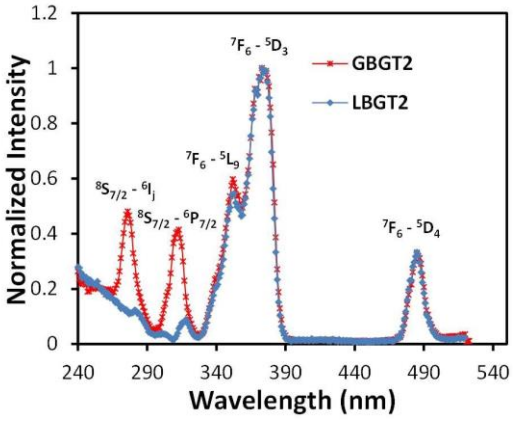

Figure 40: PLE spectra of the borogermanate glasses at 2% Tb^{3+} doping. (104)

5.3.2 Absorption of Borogermanate Glasses

UV-Vis absorption spectra were obtained for both the LBGT and GBGT samples which are presented in Figure 41: UV-Vis absorption spectra of the borogermanate glasses.. Several small absorption peaks are present in both sets of samples. For the LBGT series the peak at 485nm is attributed to the $^7F_6$-$^5D_4$ transition in Tb^{3+} and is seen to increase in intensity with increasing Tb^{3+} concentration. (105) Smaller peaks at 378nm, 371nm, 350nm, 338nm, and 315nm are respectively attributed to $^5G_6$+$^5D_3$, $^5L_{10}$, $^5L_9$, $^5D_0$, and $^5D_3$

transitions from $^{7}F_{6}$ in Tb^{3+}. (96) (89) (103) (105) The same Tb^{3+} attributed peaks are present in the GBGT series at 485, 378, 371, 350, and 338nm. There is an additional peak present in the GBGT samples at 313nm that is attributed to the $^{8}S_{7/2}$-$^{6}P_{7/2}$ transition in Gd^{3+} further indicating the Gd^{3+}-Tb^{3+} energy transfer capability. (96) (15) (103) The spectrum of the undoped borogermanate glass shows no absorption peaks, with only a gradual increase in intensity as the wavelength decreases. (106) This confirms that the observed absorption peaks are due to the Tb^{3+} and Gd^{3+} ions. The low absorbance demonstrated at the emitting wavelength of the glasses is good for the performance of the scintillators.

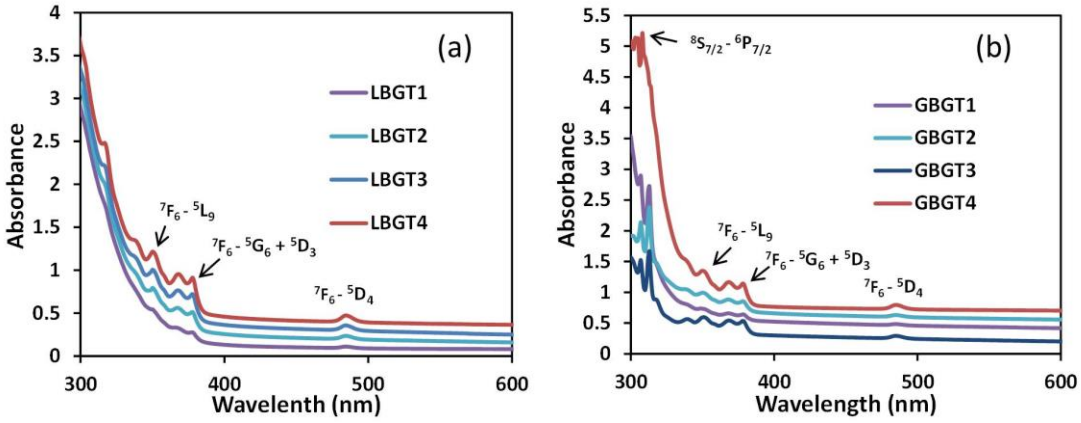

Figure 41: UV-Vis absorption spectra of the borogermanate glasses. (104)

5.3.3 Luminescent Decay Time of Borogermanate Glasses

To investigate the decay time of the produced glass scintillators the pulse height decay measurements of the 543nm Tb^{3+} emission was monitored for the LBGT and GBGT samples and the spectra are presented in Figure 42: Luminescent decay time spectra of the 543nm Tb^{3+} emission of LBGT and GBGT samples.. Trendlines are presented that follow the typical decay form of $y = Ce^{-bx}$ which were utilized to determine the decay times of the straight portions of the decay curves. The lanthanum based glasses show no consistent

trend in the decay times which all fall near 1.9ms. The slight decrease in the decay times of the higher Tb^{3+} concentration LBGT glasses is possibly the result of cross relaxation in the $^5D_3$ and $^5D_4$ states in Tb^{3+}, but there is no concrete trend and the magnitude of the decrease is very slight. (99) The slight increase in the decay time of the GBGT samples with increasing Tb^{3+} concentration could be the result of a higher radiative relaxation rate causing additional afterglow which would support the assumption from the PL magnitude measurements that the Gd based glasses possess fewer structural non-radiative defects. The long decay times of the produced borogermanate glasses is not ideal for gamma detection applications, but could still be sufficient for x-ray imaging applications.

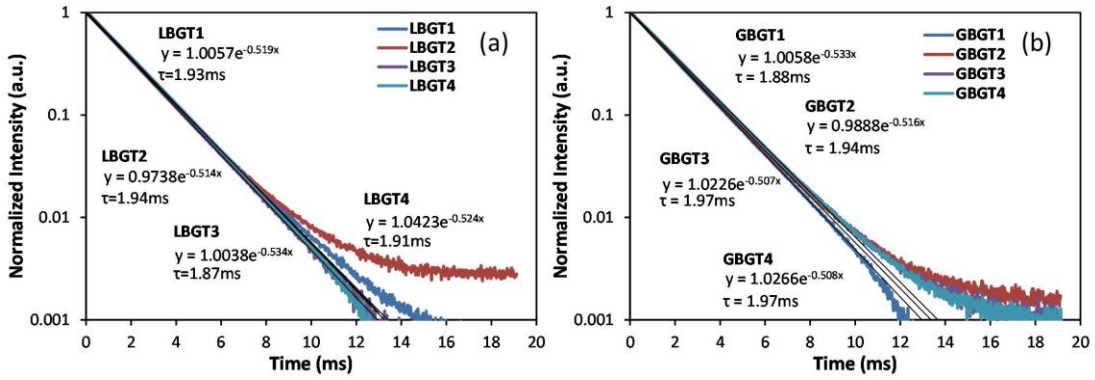

Figure 42: Luminescent decay time spectra of the 543nm Tb^{3+} emission of LBGT and GBGT samples. (104)

5.3.4 Detection Capabilities of Borogermanate Glasses

5.3.4.1 Gamma Ray Detection Measurements

Gamma ray excitation brightness measurements were taken with Co-60 and Mn-54 gamma radiation point sources possessing decay energies of 1.17/1.33 MeV and 0.835MeV respectively to investigate the gamma detection capabilities of the produced borogermanate

glasses. The results of these measurements are presented in Figure 43: Gamma ray excitation brightness measurements with Mn-54 (a) and Co-60 (b) point sources.. The measurements demonstrate the GBGT series outperforming the LBGT series counterparts across the board and nearly every GBGT sample outperforming the highest doped LBGT sample by at least 2-3 times. The greater performance of the GBGT samples is attributable to three possible reasons: fewer non-radiative defects in the GBGT samples as indicated by the high PL efficiency; energy transfer between the Gd^{3+} and Tb^{3+} ions; and the higher density of the gadolinium based glasses compared to the lanthanum based glasses. The energy transfer capabilities of the Gd^{3+} ion are likely the largest factor in this enhanced performance. In more ordered crystalline materials the ordered structure of the material allows for easier transport of energy from the excitation site to the emitting dopant ion. In a disordered glassy environment energy transfer is less likely and as such means that glassy materials rely more on direct excitation of the dopant ion which is much less likely especially at low dopant concentrations. With the inclusion of Gd^{3+} with energy transfer capabilities it is again more likely for energy from absorbed gamma radiation to find its way to the emitting dopant ion thus greatly increasing the light output of the GBGT samples as compared to the LBGT samples. The higher density of the GBGT samples also leads to an increase in the gamma ray stopping power of the material which allows for greater energy absorption and thus more light emission per volume as compared to the LBGT samples. A qualitative comparison to a CsI:Tl single crystal scintillator was conducted to obtain an idea of the light yield per energy of gamma rays absorbed. The relative light output of the single crystal was found to be ~4318 compared to the brightness of the sample

LBGT4 as presented in Table#. This gives us a light output for the GBGT4 sample at 6.9% of that of the single crystal, which comes in at ~300 ph/MeV.

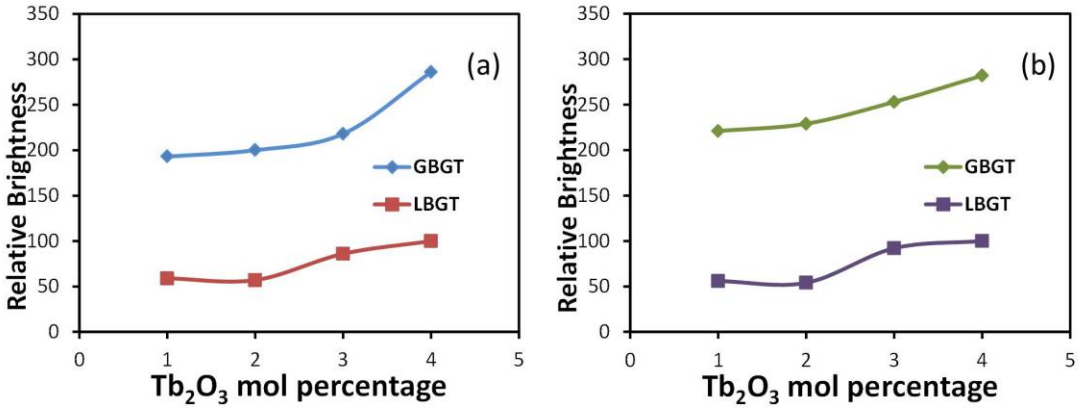

Figure 43: Gamma ray excitation brightness measurements with Mn-54 (a) and Co-60 (b) point sources. (104)

5.3.4.2 X-Ray Imaging Measurements

To investigate the potential X-ray imaging capabilities of the produced borogermanate samples X-ray imaging and light output intensity measurements were conducted and are presented in Figure 44: X-ray imaging and light output intensity profile of the LBGT4 (left) and GBGT4 (right) samples under 60 kVp excitation.. The GBGT sample again outperforms the LBGT sample with a light output intensity of at least 2.5 times greater under 60 kVp X-ray excitation. It is noted that this value is likely higher as the GBGT sample emission saturated the detector. This result is similar to the gamma excitation measurements and further supports the idea that the Gd-Tb energy transfer is highly beneficial for the performance of these glass scintillators along with the possibility of fewer structural defects in the GBGT samples.

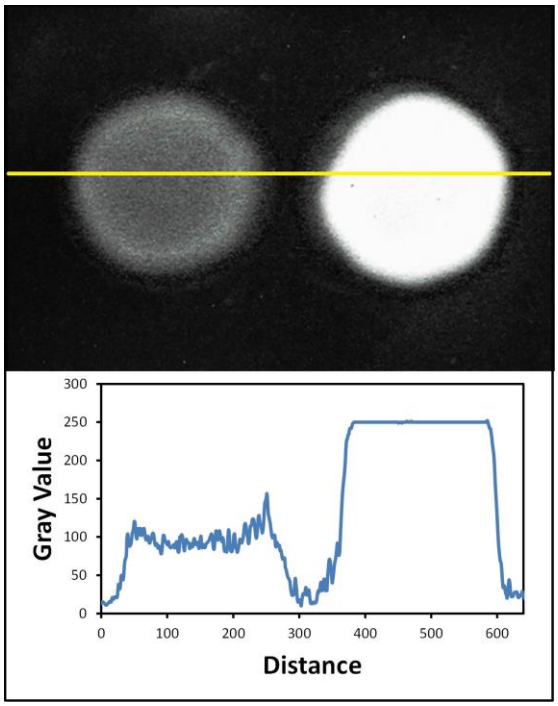

Figure 44: X-ray imaging and light output intensity profile of the LBGT4 (left) and GBGT4 (right) samples under 60 kVp excitation. (104)

5.3.5 Crystallization Capabilities of Borogermanate Glasses

The crystallization capabilities of the produced borogermanate glasses were investigated in an attempt to produce a glass-ceramic from this composition. LBGT samples were annealed at 670ºC for 6 hours, 745ºC for 3 hours, and 765ºC for 6 hours as suggested by work done previously by Gupta et al. in order to nucleate and grow $LaBGeO_5$ nanocrystals within the glass matrix. (107) At 670ºC there is no visible change in the material. At 745ºC the 1%, 2%, and 4% Tb doped samples exhibit visible softening and shape deformation along with slight opaque surface crystallization. At 765ºC all of the LBGT samples show significant surface crystallization and shape deformation. The occurrence of surface crystallization instead of bulk crystallization is not ideal for the production of a glass-ceramic and did not provide the necessary crystalline volume for

accurate identification through powder XRD. After an increase in anneal temperature to 850ºC two crystalline phases could be detected as $LaBGeO_5$ and $LaGe_2O_7$ along with additional impurity phases. It is possible that alumina content from the crucibles may be inhibiting the growth of the target stillwellite $LaBGeO_5$ phase as well as leading to the growth of the pyrogermanate $LaGe_2O_7$ phase and other phases in its place. (108) (109)

Crystallization studies of the GBGT samples were conducted at 800ºC, 850ºC, and 900ºC for 6 hours. At 800ºC surface crystallization was visible on the GBGT samples. At 850ºC the samples are fully opaque from crystalline phase growth and exhibit similar shape deformation as the LBGT samples, but XRD measurements were unable to identify the crystalline phase. At 900ºC the phases are identified as $GdBO_3$ and Gd_2GeO_5 through powder XRD. It is possible that the alumina of the crucibles is affecting this composition in a similar manner to the LBGT samples. For further improvement of these glass systems a change of crucible may be necessary.

5.4 Conclusions

The $LaBGeO_5$ and $GdBGeO_5$ crystalline compositions were identified for their support of large quantities of lanthanide and rare earth materials to support a high radiation hardness and gamma ray stopping power. The lack of cubic structure in these crystalline phases meant that refractive index matching could not be employed. As such a glass composition based on the stoichiometric composition of the crystalline phases was pursued to encourage uniform nanoparticle formation. Glass scintillators were successfully prepared and produced with compositions based off of the $LaBGeO_5$ and $GdBGeO_5$ crystalline phases. The determined characteristics of these scintillator compositions are

summarized in Table 1: Characteristics of the LBGT and GBGT series samples with light output values normalized to a percentage of sample LBGT4. below.

Ideal concentrations of Tb^{3+} doping were investigated for both glass systems. In both cases there was a consistent increase in light output with increasing Tb^{3+} concentration. With no indication of concentration quenching it is possible further loading of Tb^{3+} could continue to benefit the light output until devitrification or clouding of the glass become issues. The $LaBGeO_5$ based glasses showed no definitive trend in decay times with dopant concentration. However, a slight increase in decay times for the $GdBGeO_5$ system with increasing dopant concentration may indicate additional radiative cross-relaxation processes due to the presence of Gd^{3+}. Ultimately, the magnitude of the increase in decay time is of minimal impact to the performance of the $GdBGeO_5$ based glass system.

The $GdBGeO_5$ based samples were seen to outperform their $LaBGeO_5$ counterparts across the board in terms of emission intensity. This is believed to be attributed to three main factors: the higher density of the elemental Gd over La, the energy transfer potential between Gd^{3+} and Tb^{3+} ions within the glass matrix, and the possibility of fewer non-radiative defects in the $GdBGeO_5$ based samples. The energy transfer of the Gd^{3+} ions is of great interest to be utilized in further compositions as a means to more closely emulate the performance of single crystal type scintillators as compared to the unorganized glasses. The resulting best performing glass sample demonstrated a light output of 6.9% that of a CsI single crystal, which is ~300ph/MeV. Crystallization of the glasses was investigated to further improve their performance. Unfortunately this was unsuccessful due to the high required crystallization temperature leading to material deformation. This is suspected to be the result of Al_2O_3 contamination through the used crucibles inhibiting the formation of

the desired $LaBGeO_5$ and $GdBGeO_5$ phases. The high lanthanide concentration of La and Gd may have also factored into this difficulty in bulk crystallization of the material due to the relative immobility of these comparatively large ions. Further improvement on this composition would need to address this through use of different crucibles such as zirconia based crucibles and further investigation into the ideal lanthanide content of the glass composition.

Table 1: Characteristics of the LBGT and GBGT series samples with light output values normalized to a percentage of sample LBGT4.

Sample	Weight (g)	Volume	Density	Mn-54/g	Co-60/g	Mn-54/cm^3	Co-60/cm^3
LBGT1	15.2	3.3	4.61	69	65	66	63
LBGT2	16.9	3.6	4.76	61	57	60	57
LBGT3	17.3	3.6	4.77	89	96	88	95
LBGT4	17.9	3.7	4.81	100	100	100	100
GBGT1	18.7	3.6	5.14	185	211	197	225
GBGT2	17.2	3.3	5.18	208	239	234	257
GBGT3	13.6	2.7	5.06	263	252	277	265
GBGT4	17.8	3.5	5.05	288	284	303	298

CHAPTER 6. LITHIUM GADOLINIUM SILICATE BASED GLASS SCINTILLATOR

6.1 Composition Design of $LiGdSi_4O_{10}$ Based Glass Scintillator

The primarily silicate based crystal system $LiAlSi_4O_{10}$ has shown potential for use in the field of glass and glass-ceramic scintillators. This crystal phase has shown promise in neutron detection applications by presenting a nearly twofold increase to the commercial GS20 scintillating glass. (50) However, we look to harness some of the scintillation capabilities of this system for gamma ray detection through a substitution of Gd^{3+} for the original Al^{3+} in order to promote higher density and take advantage of the natural energy transfer capabilities of Gd^{3+}. (10) (9) Through the previous investigation it was also made clear that while Al is important as a glass matrix modifier to minimize non-radiative defects from nonbridging oxygen it can also be a detriment to the composition as an inhibitor of the nucleation of certain crystalline phases. This substitution should result in a composition based on $LiGdSi_4O_{10}$ with the possibility to allow for nucleation of nanocrystals of the same phase. Trivalent Ce is the dopant of choice for many gamma ray detection applications due to the fast decay time and short wavelength of the resulting luminescence. There are processing precautions to consider with Ce^{3+} due to its propensity to oxidize to Ce^{4+} which not only lacks luminescence but additionally acts to absorb the luminescence of the original Ce^{3+}. As such this requires we consider an inert atmosphere for use during the high temperature melt portion of the synthesis. The most efficient glasses containing Ce^{3+} dopants tend to be silicate based glasses; however, these systems often possess a low density around the order of $4g/cm^3$ or less which is not sufficient in most cases to promote

adequate gamma ray stopping power. (41) (56) This detrimental aspect of the silicate glass will be compensated for through the inclusion of the constituent Gd to promote the $LiGdSi_4O_{10}$ nanocrystal phase. In most other cases of the production of heavy metal containing glasses heavy metal oxide precursor materials are utilized. However, many of the most efficient single crystal scintillators are heavily based on halides such as bromine and iodine which takes advantage of the low phonon energy environment afforded by the high halide content. A large bromine content may also allow for a shift in the Ce^{3+} emission to slightly longer wavelengths to minimize self-absorption and further increasing the efficiency of the material. (14) Furthermore, it has been noted in other literature that the incorporation of large quantities of Gd in glass scintillators can lead to a reduction in the band gap of the material which can cause issues with the generation of luminescence in these materials. (110) (111) With these considerations in mind we turn to $GdBr_3$ as our Gd precursor material for this composition to better emulate similar single crystal compositions and maintain a large enough band gap to produce significant luminescence. For silicate glasses it is also desirable to include a fluxing agent to reduce the high melting point of the SiO_2 to improve both the manufacturing time and the overall homogeneity of the melt. In this case LiF accomplishes both the role of the fluxing agent as well as the Li precursor. If the additional F can be retained in the finished glass this choice of precursor could also help contribute to the desired low phonon energy environment. In the compositional design stage it is important to consider the band gap of the host material conduction band and the 5D emission band level in Ce^{3+} to minimize the non-radiative recombination of electron-hole pairs. (112) (113) It has been shown that increased halide content in glasses can shift the band gap to higher energies, further demonstrating the

importance of both the $GdBr_3$ and LiF precursors. (92) (114) A glass scintillator composition of similar basis on $GdBr_3$ use in a silicate matrix was pursued in the early phases of the initial foray into glass and glass-ceramic scintillators by previous members of our research group. This composition utilized a large amount of low density silicate matrix precursors to house a smaller quantity of bromide-based crystal phase precursors. From the previous investigations of compositions based more on stoichiometric replication of known crystal systems it was determined to apply that same logic to this system to improve the previously poor performance that suffered from poorly discriminated photopeaks and an energy resolution of just 27%. The starting point of the Al_2O_3 content and the subsequent replacement of Al_2O_3 with $GdBr_3$ content looks to bring the glass composition closer in line with the elemental ratios present in the $LiAlSi_4O_{10}$ crystal system and then proceed into the desired $LiGdSi_4O_{10}$ phase. The $LiGdSi_4O_{10}$ based glass was produced with a composition of $33.3SiO_2$-33.3LiF-(x)Al2O_3-(33.3-2x-1.3)$GdBr_3$-1.3$CeBr_3$ in mol% where x = 0, 0.125, 0.25, 0.375, 0.45 in order to study the impact of Al and rare-earth content of the glass matrix. Once an ideal Al/rare-earth content ratio was determined additional compositions were produced to attempt to maximize Gd incorporation.

6.2 Synthesis of Lithium Gadolinium Silicate Glass

Powder precursors in the ratios described above were combined, mixed to homogeneity, and loaded into Al_2O_3 crucibles in accordance with the established melt-quench method procedures. The purity and source of the powder precursor materials in this series study is as follows: SiO_2 (Alfa Aesar, 99.5%), LiF (Alfa Aesar, 99.99%), Al_2O_3 (Alfa Aesar, 99.97%), $GdBr_3$*H_2O (Alfa Aesar, 99.99%), and $CeBr_3$*H_2O (Alfa Aesar,

99.998%). The mixture was loaded into a furnace and heated to 1500ºC for 2.5 hours under a reducing Ar-CO atmosphere. After the melt was complete the crucible was removed and the melt was quenched in a graphite mold preheated to 400ºC. After quenching the glass was annealed at 500ºC for 6 hours to relieve internal stress.

6.3 Characterization of Lithium Gadolinium Silicate Glass

6.3.1 Photoluminescence

The produced lithium gadolinium silicate glasses were investigated under 356nm excitation for PL spectra and monitored at 431nm for PLE spectra which are presented in Figure 45: PL, PLE, and absorption spectra of lithium gadolinium based glass. Inset image of glass sample under 365nm excitation. along with the UV-Vis absorption spectrum. The produced samples display typical broad Ce^{3+} luminescence peaks with the PL peak occurring at 431nm with a FWHM of 90nm at 356nm excitation. When monitoring at 431nm a PLE peak is observed at 356nm with a slight shoulder at 320nm. These peaks are attributed to transitions in the 4f-5d band of Ce^{3+}. (14) The observed absorption spectrum is presented overlaid atop the PLE spectrum. The absorption edge location at ~360nm is consistent with the measured PLE spectrum and depicts very little self-absorption of the Ce^{3+} emission peak. The PL emission for $GdBr_3$:Ce single crystals has been reported as 419nm and in other silicate based glasses Ce^{3+} emission has been reported at 380nm, which puts the emission of this glass scintillator at a slight redshift. (115) It is believed that the glass matrix is contributing to a change in the local field of the incorporated Ce^{3+} ions as well as potentially the result of modification in the glass matrix caused by the significant incorporation of $GdBr_3$. The PL peak of the $BaGdF_5$ based glass in one of the previous

sections of this publication corroborates with the 380nm emission in a silica based glass matrix. As the Gd content in that composition was primarily introduced through Gd_2O_3 and GdF this suggests that the incorporation of Gd through $GdBr_3$ does in fact play into the redshift of the Ce^{3+} emission.

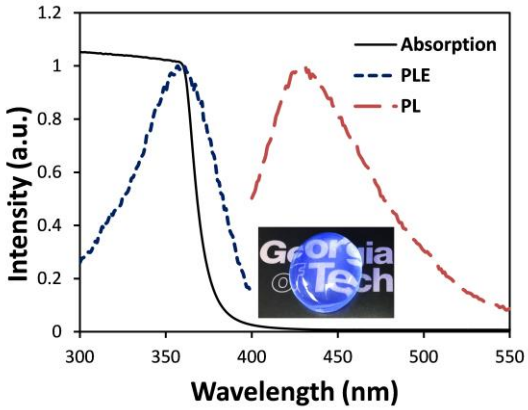

Figure 45: PL, PLE, and absorption spectra of lithium gadolinium based glass. Inset image of glass sample under 365nm excitation. (116)

6.3.2 Gd Content Dependence

The dependence on the amount of rare-earth content, with a focus on the Gd content, of the performance of the lithium gadolinium silicate based glass scintillators was investigated as Gd^{3+} has shown to be a valuable material for glass scintillator compositions. The Cs-137 excited pulse height spectra of the samples with varying rare-earth content are shown in Figure 46: Cs-137 excited pulse height emission spectra of the Gd varied glass samples. and the trends thereof are provided in Figure 47: Trends in the Gd content dependence of the Density & Peak to Compton ratio (a) and Energy Resolution & Peak Channel Number. below. As the Gd content increases the density of the material was seen to increase. This was expected through the replacement of low density Al material with

higher density Gd, but is valuable to empirically confirm. Additionally, as the Gd content is increased the peak to Compton ratio of the Cs-137 662keV excited emission also increases. The peak to Compton ratio was calculated by taking the ratio of the number of counts at the Compton edge and the Cs-137 peak position. As we can see the increase in density has successfully increased the gamma ray stopping power of the scintillator, which then leads to an increase in the fraction of incoming gamma ray photons that are fully absorbed and converted into visible light.

The position of the full energy photopeak is seen to decrease with increasing Gd content, indicating an overall decrease in light output. Similar reports have been found for high Gd content oxide glass systems that suggest this behaviour is likely due to a lowering of the conduction band in the host glass matrix relative to the Ce 5D excited states. (110) In a general sense a loss of light output is typically detrimental for the performance of a scintillator. However, in this case the relative decrease in peak channel position is incredibly small and nearly plateaus after the Al/rare-earth ratio reaches 50%. Looking at the calculated energy resolution trend we see that the energy resolution of these scintillators greatly improves with an increase in the Gd content, outweighing the relatively small loss in light output. This is seen especially well in the comparison of the Cs-137 pulse height spectra shapes. As the rare-earth/Al ratio increases the pulse height spectra progress from a non-fully resolved shoulder to sharper, fully resolved peaks as the ratio approaches 100%. Part of this continued improvement in the energy resolution is attributed to the incorporation of Gd in the form of $GdBr_3$ instead of Gd_2O_3. The large halide content incorporation provides additional benefits to those from the Gd in the form of melting temperature reduction of the allowing for greater homogeneity in the melt which results in

an enhanced uniformity of the emitted light to the PMT, resulting in a sharper full energy photopeak. This improvement results in an energy resolution of 14.0% for the Cs-137 662keV gamma ray excitation. It is worth noting that it is likely that some of the Br, F, and Li components of the powder mixture are lost during the melt phase due to evaporation. There has been notable marked Br loss during the melt, but it is believed that some of the Br was retained within the glass matrix to account for part of the performance improvement. To confirm this hypothesis additional samples were prepared with the 32mol% of $GdBr_3$ replaced with 16mol% Gd_2O_3. For these samples the energy resolution was measured to be 18.4%. This suggests that the incorporation of Gd through $GdBr_3$ is beneficial for the performance of the glass. The performance of the Gd_2O_3 samples is corroborated by Chewpraditkul et al who reported a glass scintillator with an energy resolution of 18.3%. (9)

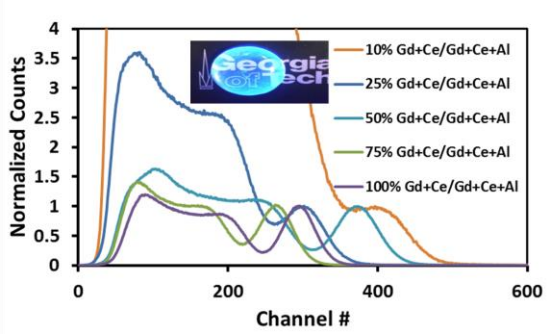

Figure 46: Cs-137 excited pulse height emission spectra of the Gd varied glass samples.

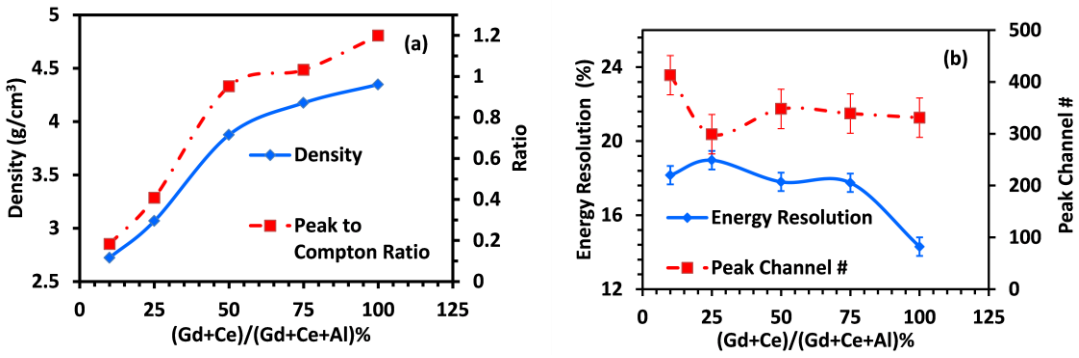

Figure 47: Trends in the Gd content dependence of the Density & Peak to Compton ratio (a) and Energy Resolution & Peak Channel Number. (116)

6.3.3 Ce^{3+} Dependence

To pursue further performance enhancement of the lithium gadolinium silicate based glass scintillator the dependence on Ce^{3+} concentration was investigated beginning with the best performing composition of the Gd dependence series as the base composition. A series of compositions were investigated varying between 0.1mol% Ce to 4.0mol% Ce. The performance trends for the Ce dependence series are presented in Figure 48: Ce dependence trends for the energy resolution and peak position for lithium gadolinium

silicate based glass. below with the Cs-137 excited pulse height spectra presented in Figure 49: Cs-137 excited pulse height spectra for the Ce dependence series samples.. The light output as viewed through the peak position is seen to rise drastically with Ce^{3+} increase up until the Ce^{3+} concentration reaches 1.3mol% at which point the light output plateaus. This view of the light output gives us a direct view of the onset of the concentration quenching effect that is present in Ce^{3+} which limits the total dopant loading possibilities. (8) The energy resolution of the samples is measured to improve with Ce^{3+} concentration approaching 1.3% however, once the Ce^{3+} concentration exceeds 1.3% the energy resolution decreases. The Ce^{3+} concentration was a much smaller magnitude change to the overall composition of the glass than the total rare-earth content comparison. As such, the overall Ce^{3+} content did not affect the density of the material to any significant degree. The peak to Compton ratio shows a slight dependence on the Ce^{3+} concentration, primarily in the 0.1mol% to 0.6mol% range. With the low end of the dopant concentrations the glass has difficulty transferring energy to the luminescent centers presented by the dopant which manifests in the pulse height spectra as a single collapsed peak at 0.1% Ce doping. With the doping increased to 0.6mol% the photopeak begins to separate from the Compton continuum, but the low peak position and the compressed Compton continuum demonstrate that the glass is still not fully converting gamma photons to visible light efficiently. Once the dopant concentration passes 0.6mol% the Compton continuum is now fully resolved alongside the photopeak and further changes are comparatively small. However, there is still a slight trend of the peak to Compton ratio decreasing as the Ce^{3+} concentration exceeds 1.3%. While the Compton continuum is typically indicative of gamma ray photons that are not fully absorbed by the material, it is possible that the relative increase in the

height of the Compton continuum in this case is the result of the detection of the concentration quenched cross-relaxation transitions by the PMT.

In this case it is likely that the energy resolution falling off at higher concentrations is primarily the result of the loss of light output through concentration quenching of the Ce^{3+} emission. While it is possible that a similar additional homogeneity factor is influencing the energy resolution in a similar manner to the rare-earth dependence series, the direct corroboration between the light output and the energy resolution offers a more direct explanation.

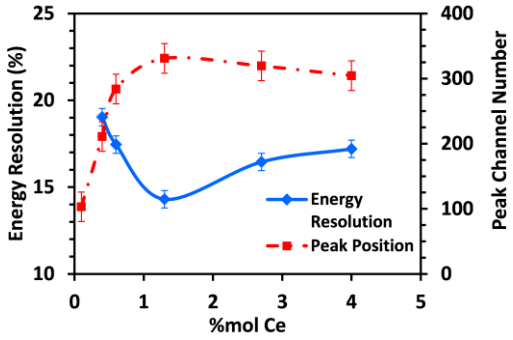

Figure 48: Ce dependence trends for the energy resolution and peak position for lithium gadolinium silicate based glass. (116)

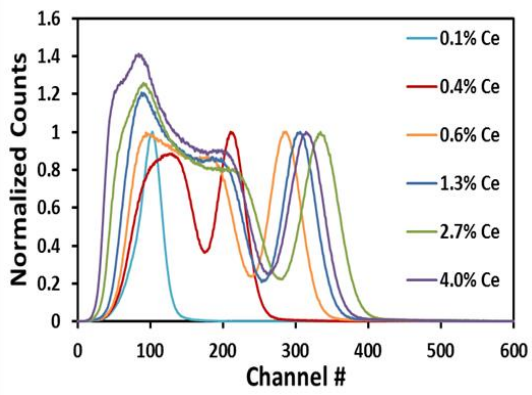

Figure 49: Cs-137 excited pulse height spectra for the Ce dependence series samples.

The Cs-137 spectrum of the best produced glass scintillator was compared to the Cs-137 excited spectrum of a NaI:Tl single crystal scintillator and is presented in Figure 50: Gamma excited pulse height spectra of (a) the best produced glass sample and NaI:Tl single crystal under Cs-137 excitation and (b) multinuclide pulse height spectra for the best glass sample.a. The dimensions of the respective scintillators are 26mm diameter x 8mm height for the produced glass scintillator and 50.8mm diameter x 50.8mm height for the NaI:Tl single crystal. The volume difference contributes to the difference in the viewed spectra which primarily manifests as the much smaller peak to Compton ratio for the smaller glass scintillator. The energy resolutions calculated from this measurement were 14.0% for the produced glass scintillator and 7.8% for the single crystal. A qualitative comparison of the light output was conducted for these two scintillators. It was determined that the light output of the glass scintillator was 8.2% that of the single crystal. With a reported light output of 39,000 ph/MeV for the single crystal the light output for the glass scintillator is calculated to be 3200 ph/MeV.

The glass scintillator was tested with an array of radionuclide point sources in order to investigate its response to a wider field of targets. The gamma ray excited pulse height

spectra of these additional nuclides are presented in Figure 50: Gamma excited pulse height spectra of (a) the best produced glass sample and NaI:Tl single crystal under Cs-137 excitation and (b) multinuclide pulse height spectra for the best glass sample.b. The full energy photopeaks for sources ranging from 122keV to 1332keV are clearly visible, with sufficient energy resolution to identify and discriminate the various sources. With additional improvement to the energy resolution this material could provide serious competition to single crystals.

As the composition of this scintillator prominently features Li to no ill effects the incorporation of ^{6}Li through ^{6}LiF was investigated to explore the neutron detection capabilities of this material. The best performing composition was replicated with the direct substitution of ^{6}LiF for the original LiF. The resulting scintillator was exposed to Cs-137, Am-241, and Cf-252 sources to gather gamma, alpha, and neutron excited pulse height spectra which are depicted in Figure 51: Alpha, gamma, and neutron spectra of $LiGdSiO_4$ based glass with ^{6}LiF inclusion.. Full energy photopeaks are visible for all three sources investigated including the Cf-252 neutron source when a polyethylene spacer is utilized in order to regulate the emitted neutrons to thermal energies. These results indicate that this material could be utilized as either a gamma ray or neutron detector, with the potential to utilize the material as a simultaneous detector for both.

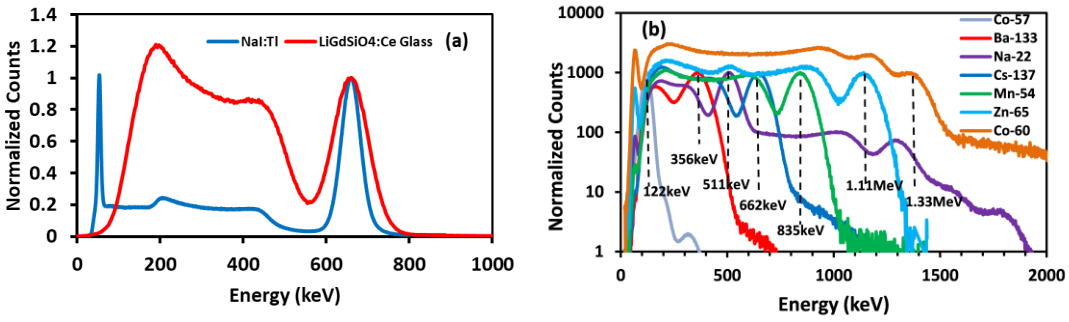

Figure 50: Gamma excited pulse height spectra of (a) the best produced glass sample and NaI:Tl single crystal under Cs-137 excitation and (b) multinuclide pulse height spectra for the best glass sample. (116)

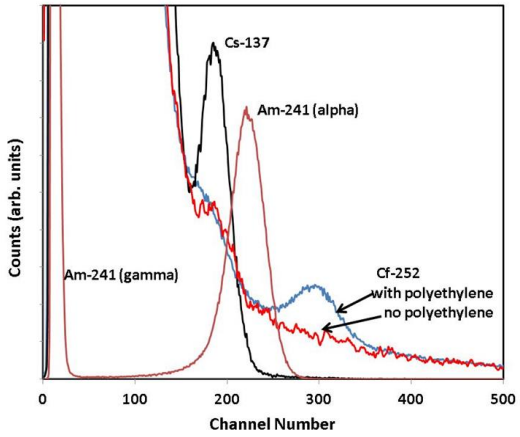

Figure 51: Alpha, gamma, and neutron spectra of $LiGdSiO_4$ based glass with ^6LiF inclusion.

6.3.4 Luminescent Decay

The luminescent decay time of the produced glass scintillators was investigated as a function of both the rare-earth/Al ratio and the Ce^{3+} concentration. These decay time pulse measurements are presented in Figure 52: Luminescent decay time measurements of the lithium gadolinium silicate glass scintillators compared with NaI:Tl single crystal.

alongside the measurement of a NaI:Tl single crystal. With increasing rare-earth content there is a slight increase in decay times. This is attributed to greater radiative recombination and fewer nonradiative recombination defects in the glass matrix as a result of the increased $GdBr_3$ content in the precursor mixture. For the Ce dependent series the linear portions of the decay curve were fit to the typical exponential equation and the decay time calculated thusly. The decay times were found to range from 230ns to 690ns with the decay time increasing with decreasing Ce^{3+} concentration. The measured decay times of these glass scintillators is much greater than that of typical Ce^{3+} doped glasses and crystals, which is on the order of tens of ns. Currently it is unclear what exactly is the cause of this extended luminescent decay time. There have been occasional reports of Ce based scintillators with longer decay times such as 212ns from a $GdBr_3$:Ce scintillator and 221ns from a $Gd_3Al_3Ga_2O_{12}$:Ce scintillator. (115) (117) In comparison, the NaI:Tl single crystal was measured at 240ns which is consistent with reported values for this material. The decay time of the 2.7% and 4.0% Ce-doped samples does manage to undercut that of the single crystal; however, this is likely due to the onset of concentration quenching leading to nonradiative energy transfer which reduces afterglow.

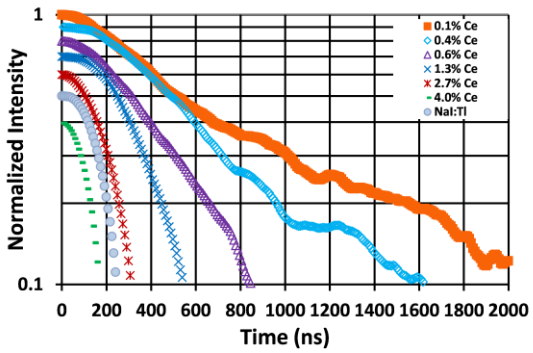

Figure 52: Luminescent decay time measurements of the lithium gadolinium silicate glass scintillators compared with NaI:Tl single crystal. (116)

6.3.5 Crystallization Attempts

The production of this glass system was heavily based on two crystal systems, the silicate $LiAl(Gd)Si_4O_{10}$ that has shown promise for neutron detection and the $GdBr_3$ system which has shown promise in its single crystalline form for gamma detection. After assessing the performance of the base scintillating glass the production of a glass-ceramic was attempted in the same manner as the previously discussed glass-ceramic systems. Heat treatments were performed at temperatures starting at 600ºC and increasing to 900ºC+ for time periods of 6 hours. At lower temperatures little change was visible in treated samples. As temperatures increased softening and deformation of samples was observed with no accompanying visible crystallization. Treatments ceased after higher temperature heat treatments began to induce darkening in the glass indicating the likely formation of color center defects which compromise luminescent performance to a much greater degree than crystallization could improve.

The complete lack of crystallization was an interesting development for this composition. Even when previous crystalline phases could not be adequately identified

they still demonstrated visible signs of crystallization such as increasing opacity and surface crystallization. Additional causes of crystal phase inhibitors were considered that could be mitigated. Of primary note was the use of alumina crucibles. During compositional tuning of this glass system it was noted that as precursor Al_2O_3 content was removed the alumina crucibles began to demonstrate the appearance of grooves at the level of the precursor powder mixture. Al content has been associated previously with difficulty in cultivating certain rare-earth intensive crystalline phases as seen with the $LaBGeO_5$ and $GdBGeO_5$ systems reported above. This was one of the primary reasons for investigating the impact of lower Al content in the study of this system from the outset. As such, further measures for limiting the melt's exposure to Al were investigated.

In order to further limit the exposure of the glass melt to incidental Al content the use of alternative crucible materials was investigated. Platinum crucibles are widely used in many glass-ceramic synthesis applications and as such were considered as an option early. However, Pt crucibles are significantly vulnerable to the high halide content that this glass composition has acquired, which would ruin the crucible significantly quicker than is typical and drastically increase the production cost of the glass. Of other materials available zirconia presented the simplest incorporation into the current synthesis procedures as the material behaves in a similar manner to the original alumina without other considerations. Samples of the best performing $LiGdSi_4O_{10}$ composition were prepared under identical conditions as detailed above with the original alumina crucibles exchanged for zirconia crucibles. It was discovered that despite no change to the glass composition the melt could no longer be poured as a molten liquid and instead remained inside the crucible in a form resembling a semisolid puck. Despite the known downsides

of Al_2O_3 content within the previous glass compositions it still does offer value as a glass matrix modifier. While this typically refers to the performance of the material once it has quenched and set it is still the most likely result of the change as no other factors of the synthesis procedure were altered. The etching observed in the alumina crucibles must have been the result of the melt forcibly incorporating a portion of the alumina crucible as Al_2O_3 into the composition, allowing for ease of production of the final molten glass that was poured and quenched.

Further tuning of the composition was pursued by estimating the amount of Al_2O_3 etched from the crucibles and re-incorporating that content into the precursor mixture to be prepared in the zirconia crucibles, which resulted in a composition of $31.25SiO_2$-31.25LiF-$6.25Al_2O_3$-$30GdBr_3$-$1.25CeBr_3$. However, this substitution was ultimately unsuccessful in reproducing the stable melt that was observed with the alumina crucibles. While the original assumption regarding Al_2O_3 etching presented the most evidence, it is also possible that a factor of the zirconia crucibles was inhibiting the melt directly. More direct investigation of the composition of the final product through EDS mapping was not available at this time, but will present great interest for future work with this glass system.

6.3.6 Other Optimization Pathways

The strong success of the development of this composition for the performance of glass based scintillators ended off incredibly close to the desired target for energy resolution of gamma ray responses. As such other additional methods for pushing the performance of this system farther were investigated.

As the performance trends very positively with Gd content additional avenues of increasing Gd loading were investigated as well. The increase in $GdBr_3$ precursor at the expense of SiO_2 was investigated to allow for greater Gd loading in the material. Initial small substitutions of this manner resulted in clear glasses with slightly lower energy resolutions of ~15%. Further SiO_2 replacement led to devitrification of the glass upon casting indicating that the loss of SiO_2 had compromised the stability of the glass matrix. For pure gamma detection the direct content of Li was not as critical as it is for neutron detection, and as such was investigated as a sacrificial element for greater loading of Gd content. The conversion of LiF precursor content into an even split of $GdBr_3$ and SiO_2 to preserve the stability of the matrix resulted in glass samples that retained their transparency, but tended to produce smaller sample pours from the same molar amount of material. This may have been caused by the loss of the fluxing features of the LiF leading to an increase in the melting temperature and producing more viscous melts. Substitution of LiF for other higher density fluorides such as CsF was also investigated to further improve stopping power in a similar manner to the $BaGdF_5$ trials. However in this system the substitution resulted in a drastic increase to the melting temperature of the mixture and prevented successful melting with our current equipment.

While the overall performance trends positively with Gd content it was noted that the light output was higher for samples that still contained some Al_2O_3. This thread was followed slightly through attempts at incorporating AlF_3 in place of the Al_2O_3 for some of these compositions in order to further push the light output. However, full replacement of Al_2O_3 with AlF_3 resulted in a lower energy resolution than the corresponding Al_2O_3

containing compositions, and partial replacement of Al_2O_3 with AlF_3 causing even greater energy resolution loss.

6.4 Conclusions

This final series of produced glass scintillators provides the culmination of the explored compositional design principles previously investigated when applied to a robust silicate based glass. For the base glass composition a crystalline phase was identified that possessed high radiation hardness, the potential for high density, and could support Ce^{3+} doping. A glass composition was formulated based on the stoichiometry of this crystalline phase in order to harness these beneficial aspects in a glassy material. Scintillating glass samples were successfully obtained from this composition and tuning approaches were investigated. The overall characteristics of both sets of compositions are compiled in Tables 2 & 3 below.

Previous compositional studies had identified Al_2O_3 as a potential source of low density in the glasses as well as potentially inhibiting the formation of certain crystalline phases. Through investigating its replacement with additional Gd content in the form of $GdBr_3$ a drastic improvement in performance was observed. This improvement was attributed primarily to an increase in the density of the material initially. With additional investigation a benefit was confirmed through incorporating Gd through $GdBr_3$ specifically over an alternative source such as Gd_2O_3. While it is likely that much of the Br content provided was lost to evaporation during the melt this confirmed impact of utilizing $GdBr_3$ as a constituent suggests some Br retention in the glass matrix. This discovery provides a new pathway for potential future improvements in other materials to come.

Compositional tuning also looked at the optimal Ce dopant concentration for maximum light output. The benefit of additional Ce content was found to reach a plateau at 1.3% before concentration quenching began to limit the additional light output. These two compositional tuning approaches combined to produce a transparent glass scintillator with an energy resolution of 14.0% for the Cs-137 662keV emission. This combination of tuning approaches resulted in a total improvement from 27.0% to 14.0% over the course of this research. While this is still not quite enough to find immediate use in gamma ray detection or neutron detection applications it is a significant result for the field of gamma ray detecting glass scintillators. The incorporation of 6LiF in place of the general LiF allowed for the detection of neutrons in addition to gamma radiation, with a significant separation in the two spectra signatures, which suggests the possibility of use as a multi-signature detector instead of utilizing two different scintillators for such applications.

Further optimization attempts were pursued through the incorporation of additional Gd content at the expense of other precursors, incorporation of other high density halide precursors at the expense of Li, and substitution of current oxide based precursors with additional halide based precursors were ultimately unsuccessful, but could be promising for investigation with furnaces capable of greater melt temperatures.

Formation of a glass-ceramic material from this produced glass was pursued, but unsuccessful, resulting in the likely formation of color center defects instead of nucleating a crystalline phase. Complete elimination of Al_2O_3 content was pursued in an attempt to improve this. It was discovered that while eliminating precursor Al_2O_3 greatly improved performance, some amount of Al_2O_3 appears to be necessary for proper formation of the glass melt to allow for pouring the melt during the quench phase of synthesis. For future

work with this glass system accurate EDS investigation will be of great value to identify the final composition of the synthesized glass.

At the time of the publishing the JACS article this work was featured in it was to our knowledge the best performing fully glass scintillator published with energy resolution measurements to date. With further investigation this composition could provide a basis for a material that can compete with single crystal scintillators at a reduced cost.

Table 2: Properties of the Gd-dependent compositions.

Sample	Density (g/cm^3)	Resolution (%)	Light Yield (Ph/MeV)
10%Gd+Ce:90%Al	2.72	15.6	4317
25%Gd+Ce:75%Al	3.07	18.0	3125
50%Gd+Ce:50%Al	3.88	15.9	3638
75%Gd+Ce:25%Al	4.18	16.8	3544
100%Gd+Ce:0%Al	4.37	14.0	3460

Table 3: Characteristics of the Ce-dependent compositions.

Sample	Density (g/cm^3)	Resolution (%)	Light Yield (Ph/MeV)	Decay Time (ns)
0.1% Ce	4.15	N/A	1077	697
0.4% Ce	4.52	19.0	2206	694

0.6% Ce	4.23	17.5	2969	659
1.3% Ce	4.37	14.0	3460	522
2.7% Ce	4.40	16.5	3339	317
4.0% Ce	4.42	17.2	3183	230

CHAPTER 7. OVERALL SUMMARY AND RECOMMENDATIONS

7.1 Introduction

This chapter ultimately summarizes the performance of the investigated glass and glass-ceramic scintillator systems which were discussed in the previous chapters. The efficacy of the decided upon glass and glass-ceramic systems are detailed and the efforts to further improve the performance of these systems through nucleation and growth of nanocrystalline particles and large-scale compositional tuning are analyzed and discussed. Due to the broad investigative nature of the work detailed here for the advancement of the frontier of glass and glass-ceramic scintillation systems there remain some threads of further research that with adequate time and resources allocated to them could lead to further innovation of these systems. This section will detail suggestions for the pursuit of these avenues of future research.

7.2 CaF_2 Neutron Detector

The investigation of the CaF_2 based glass-ceramic system provided a strong vision of basic aspects of the design and production of scintillating glass-ceramics. The CaF_2 crystalline phase was brought to attention through reports of a fully ceramic system based on the phase that demonstrated high neutron excited light yields but suffered from low transparency. A low-density aluminosilicate glass matrix was designed to house the material required to produce the CaF_2 crystalline phase as nanoparticles after post-processing heat treatment. Through nucleation and growth of the CaF_2 nanocrystals a

drastic improvement in the scintillation response of gamma and alpha radiation was noted. Through additional refractive index matching pursued with the addition of AlF in place of Al_2O_3 the light yield under gamma and alpha excitation was enhanced further. Incorporation of ^6LiF into the precursor composition provides this material with a thermal neutron detection cross section. The transparency of the material was maintained through nucleation and growth, and the performance enhancing nanocrystalline phase resulted in a neutron excited energy resolution of 15.9% with a light output of 5,600 ph/neutron. This measured performance is 70% that of a known commercial neutron scintillating glass GS20.

For future work performed with this or a similar aluminosilicate based CaF_2 containing glass-ceramics there appears to be two very promising avenues for further development of the scintillator. The brief foray into refractive index matching between the glass matrix and crystalline CaF_2 that was performed yielded positive results with minimal compositional adjustment. An in depth investigation of the refractive index of this glass matrix in relation to that of the produced CaF_2 nanocrystals would be of great interest to the field as a whole. If the refractive index mismatch could be resolved to a great degree it could allow for the growth of nanocrystals of greater size and potentially the full crystallization of the glass matrix into a transparent composite ceramic. The other potentially interesting thread for investigation lies in the further tuning of the composition and heat treatment procedures to allow for production of a greater volume fraction of the CaF_2 crystalline phase. While the generation of nanocrystalline CaF_2 particles in the reported investigation was limited by the loss of transparency at temperatures exceeding 650ºC the TEM measurements and XRD spectra still paint a picture of a relatively low

volume fraction of crystalline phase. Additional time spent at these temperatures is likely to result in larger size crystalline particles, but due to Ostwald ripening principles it is unlikely to increase the number of particles to add crystalline volume fraction without compromising transparency. As such an in depth review of the incorporation of greater crystal phase precursors into the composition of the glass-ceramic could return interesting results. Finally, an investigation into the optimization of heat treatment parameters including both growth temperature and heating rate merits interest. Heat treatments in this study were performed under a single heating rate, investigation into the optimal heating rate could allow for greater control over the size and volume fraction of the crystalline nanoparticles.

7.3 $BaGdF_5$ Gamma Detector

A wide array of compositional adjustments for improved gamma ray stopping power through the use of greater rare-earth precursor content as well as consideration of nucleation agents resulted in a $BaGdF_5$ based oxyfluoride glass-ceramic doped with Ce^{3+} that exhibits a strong gamma radiation excited scintillation response. The final composition showed great improvement in the sharpness of the full energy photopeaks from the initial starting composition and featured an energy resolution of 15.4% under excitation by 662keV Cs-137 gamma radiation. The light yield of this material was calculated through comparison to an NaI:Tl single crystal and found to be 3460 ph/MeV. While these light yield and energy resolution values still leave something to be desired for use in commercial applications they are a major improvement over other glassy scintillators, the literature of which tends to lack energy resolution reports. The nucleation and identification of the $BaGdF_5$ crystalline phase was successful after the culmination of all composition

alterations. However, in the case of this material the heat treatment of samples did not yield a noticeable scintillation performance improvement which is likely related to the increased crystallization temperature of this final composition.

For future work dealing with this and similar $BaGdF_5$ based compositions there still remain some facets of the composition design that merit further investigation. The investigation into increasing the rare-earth loading of this composition was valuable in pushing the performance of the base glass material, but the alterations inhibited the nucleation of the desired crystalline phase. Further investigation into the balance of the performance of the base glass and the inclusion of additional nucleating agent precursors to hone in on the ideal intersection of these potential avenues of improvement could yield valuable insight. There is another possibility, in that crystallization of the glass in this composition did not properly result in the substitution of the Ce^{3+} dopant into the nucleated crystalline particles, in which case the nucleation of the crystalline phase simply may not adequately take advantage of the greater quantum efficiency of the crystalline region if it does not have a direct path to Ce^{3+} luminescence centers. A direct investigation of the coordination of the Ce^{3+} dopant incorporated into the glass may provide valuable insight for the benefit of the field.

7.4 Borogermanate Gamma Detectors

A pair of borogermanate based glass scintillator compositions were developed that included high loading of lanthanide elements in the form of La and Gd that offered a high gamma ray stopping power. Transparent glass scintillators based on these compositions were produced with Tb^{3+} doping as allowed by the crystal system compositions. The Tb

doping allowed for a bright response to gamma radiation and the light yield of the scintillator with the highest Tb doping and brightness was found to be % of that of a CsI:Tl single crystal. The light yield was thus calculated to be roughly 300 ph/MeV. The scintillators exhibited surface crystallization, but did not easily induce bulk crystallization and the target $LaBGeO_5$ and $GdBGeO_5$ phases were inhibited by formation of other phases Despite these relatively minor results this investigation was valuable in the comparison of the performance of the similar lanthanide elements. The possibility of energy transfer from Gd^{3+} to trivalent activator ions resulted in an improvement in performance of up to 3x from simply substituting Gd for La in the precursor compositions. The evidence of this energy transfer mechanism persisting in non-crystallized glass scintillators offers valuable compositional design consideration for future development of glass and glass-ceramic scintillators. . X-ray imaging tests also proved promising with the Gd based borogermanate exhibiting sufficient brightness to saturate the available imaging detector.

While these systems did not provide ideal performance, there is still room for further improvement. Production of samples with these borogermanate based compositions in alternate crucible materials to circumvent the crystal phase inhibition of Al_2O_3 would provide further improvement in the formation of a bulk crystallized glass-ceramic for greater scintillation efficiency. Another potential avenue of improvement lies in the incorporation of alternative dopant activator ions for faster decay times and better emission wavelength match to the detection system hardware for detection applications outside X-ray imaging. However, this method of improvement will not produce strong results until the light yield of the base glass is greatly improved.

7.5 $LiGdSi_4O_{10}$ Based Gamma Detector

The most promising results by far come from this final composition of a silicate based glass matrix designed around a permutation of the $LiAlSi_4O_{10}$ crystalline phase. As Al content has presented conflicting benefits across the history of glass-ceramics through benefits in maintaining the stability of the glass matrix as well as detriments in inhibiting the formation of some targeted crystalline phases a study was conducted investigating the relationship between Al content, increasing rare earth loading, and overall scintillation performance. After finding the strong benefits to scintillation performance through the incorporation of Gd in the previous studies the possibility of replacing the lower density Al with higher density and higher Z number Gd was investigated. Through systematic adjustment of the Al to rare-earth ratio it was discovered that the more Al was replaced with Gd precursors the greater the benefit to the scintillation performance was had while maintaining the ability to produce a transparent, stable glass. The result was found that full replacement of Al precursors with Gd precursors yielded the best scintillation performance with all factors considered. Additional trials were then performed to determine the ideal level of Ce concentration to allow for the greatest light yield while avoiding detrimental concentration quenching that Ce doped materials are prone to. The resultant composition with 1.3% Ce doping yielded a silicate glass with a density of 4.4g/cm3 with an energy resolution of 14.0% under 662keV Cs-137 excitation and showed strong resolved photopeaks for many varieties of gamma radiation sources. Through a comparison to a NaI:Tl single crystal the light yield was determined to be 3200 ph/MeV. At the time of first report of these findings this was the best performing fully glass gamma detection scintillator to date in terms of energy resolution.

While the above result for this composition presents a strong advancement in the field of scintillating glasses there still remains room for improvement with future developments. Of the most immediately notable is the production of a glass-ceramic from this composition. Attempts to form a glass-ceramic from this base scintillating glass were believed to be inhibited by Al contamination which has been shown to suppress the formation of certain crystalline phases and encourage the formation of additional undesired phases. While the Al precursor material content was completely replaced during the study of this composition there remains the possibility that the utilized alumina crucibles may have contaminated the samples during the melt period of the glass synthesis. Preliminary attempts to address this possibility through the use of zirconia crucibles illuminated a new difficulty in producing a melt that could be poured from the crucible to obtain a transparent glass. A full investigation into the necessary quantity of Al_2O_3 precursor content for the successful production of a clear, transparent glass within a non-alumina crucible would offer great benefit to the further understanding of the system and add a further stepping stone to further investigation of the capabilities of a $LiGdSi_4O_{10}$ based glass-ceramic. Other potential avenues for future improvement lie in rigorous investigation of the final composition of these produced glasses through techniques such as EDS. The incorporation of Gd content through GdBr3 instead of an oxide precursor presented obvious benefit to the scintillating performance of the material as seen through the comparison of the final 14.0% energy resolution glass with a glass produced of the same composition with Gd_2O_3 substituted in for $GdBr_3$ which resulted in a performance of 18.4%. However, much of the nature of this benefit is speculative. An in-depth investigation of the final compositional

make-up and the presence of Br in the final material could illuminate additional avenues for further optimizing the composition of this scintillator.

7.6 Engineering Considerations for Future Work

After the previous work there still remains one main engineering consideration that did not have the available time to be fully pursued in the addition of a stirring mechanism for the synthesis process. While the small samples produced in this study experienced sufficient homogenization during the melt phase through the incorporation of fluxing agents and halides a direct additional method of stirring the mixture would allow for potentially greater homogenization, and is likely a necessity for the production of larger size batches of these glass and glass-ceramic compositions. A schematic of the proposed mechanism is provided below in Figure 53: Example of proposed stir rod setup for future endeavors.. Additional considerations come with the use of such a stirring mechanism for the compositions and setup that have been explored in this study. Firstly, many of the Ce^{3+} based compositions are incredibly susceptible to oxidation with different levels of exposure leading to various impacts on the performance from mild performance decreases to full discoloration of the glass. This risk of oxidation required the use of both a reducing atmosphere and excess graphite during the melt phase with an acutely small enclosure protecting the precursor mixture. In order to introduce a stir bar mechanism without resulting the oxidation of the dopant either the use of a much greater reducing atmosphere must be employed or the stir bar must be incorporated into the containment housing for the precursor mixture. Additionally, the composition of the bar itself would need careful consideration. Alumina was the leading candidate initially due to its robust tolerance of the required melt temperatures and resistance to spontaneous fracturing from heat shock;

however, the revealed impact on the crystallization capabilities of certain glass compositions after Al_2O_3 exposure has rendered it less desirable. Other oxide based ceramic materials such as zirconia may be usable, but the vulnerability to heat shock for zirconia has been noted when removing zirconia crucibles from the furnace, leading to spontaneous shattering shortly after pouring the melt. Metals such as Pt that have already found some use as crucibles in other considerations may be useful, but have been known to suffer degradation and corrosion when exposed to high levels of halides such as the $GdBr_3$ that was crucial for this study's best composition. A specially designed ceramic material may be required for the successful use of such a stir bar mechanism for these compositions.

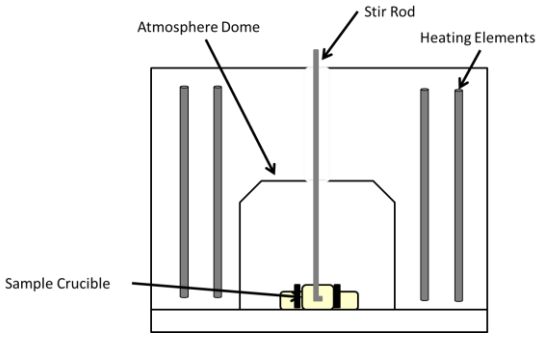

Figure 53: Example of proposed stir rod setup for future endeavors.

REFERENCES

1. *Neutron detection alternatives to 3He for national security applications.* **R. Kouzes, J. Ely, L. Erikson, et al.** 2010, Nuclear Instruments and Methods in Physics Research A, Vol. 623, pp. 1035-1045.

2. *Inorganic thermal-neutron scintillators.* **C.W.E. van Eijk, A. Bessiere, and P. Dorenbos.** 2004, Nuclear Instruments and Methods in Physics Research A, Vol. 529, p. 260.

3. *A comparison of fast inorganic scintillators for thermal neutron analysis landmine detection.* **Faust, J.E. McFee and A.a.** 2009, IEEE Transmission on Nuclear Science, Vol. 56, p. 1584.

4. *Inorganic scintillators for thermal neutron detection.* **Eijk, C.W.E. van.** 2012, IEEE Transmissions on Nuclear Science, Vol. 59, p. 2242.

5. *Scintillator Phosphors for Medical Imaging.* **Duclos, S.J.** 1998, Electrochemical Society Interface, Vol. 7, pp. 34-39.

6. *Inorganic Scintillators: Today and Tomorrow.* **Weber, M.** 2002, Journal of Luminescence, Vol. 100, pp. 35-45.

7. *Luminescent glasses for use in the detection of nuclear radiation.* **D.G. Anderson, J. Dracass, T.P. Flanagan.** 1959, Journal of Electronics and Control, Vol. 7, pp. 463-464.

8. *New cerium activated scintillating glasses.* **Ginther, R.J.** 1960, IEEE Transmissions on Nuclear Science, Vol. 2, pp. 28-31.

9. *Luminescence and Scintillation of Ce3+-doped Oxide Glass with High Gd2O3 Concentration.* **W. Chewpraditkul, X. He, D. Chen, et al.** 2011, Phys Status Solidi A, Vol. 208, pp. 2830-2832.

10. *Compositional Dependence of Scintillation Yield of Glasses with High Gd2O3 Concentrations.* **J. Fu, J.M. Parker, R.M. Brown, et al.** 2003, Journal of non-Crystalline Solids, Vol. 326, pp. 335-338.

11. *Glass scintillators for neutron detection.* **L.M. Bollinger, G.E. Thomas, R.G. Ginther.** 1959, Review of Scientific Instruments, Vol. 30, p. 1135.

12. *Scintillating glass for the detection of slow neutrons.* **V.K. Voitovetskii, N.S. Tolmacheva, M.I. Arsaev.** 1960, Soviet Journal of Atomic Energy, Vol. 6, pp. 203-207.

13. *Radioluminescence of Ce3+-doped dense scintillating glasses.* **C. Jiang, P. Deng, J. Zhang, et al.** 2013, Journal of Alloys and Compounds , Vol. 581, pp. 801-804.

14. *Transparent Oxyhalide Glass and Glass Ceramics for Gamma Ray Detection.* **C. Han, M. Barta, M. Dorn, et al.** 2011, Proceedings, Hard X-Ray, Gamma Ray, and Neutron Detector Physics XIII, p. CASPIE:8142.

15. *Synthesis and luminescence properties of transparent nanocrystalline GdF3:Tb glass-ceramic scintillator.* **G. Lee, N. Savage, B. Wagner et al.** 2014, Journal of Luminescence, Vol. 147, pp. 363-366.

16. *Energy-dependent scintillation intensity of fluorozirconate-based glass-ceramic x-ray detectors.* **S. Schweizer, B. Henke, S. Koneke, et al.** 2006, Proceedings of SPIE, Vol. 6142.

17. *Microstructure and luminescence of transparent glass ceramic containing Er3+:BaF2 nano-.* **D. Chen, Y. Wang, Y. Yu, et al.** 2006, Journal of Solid State Chemistry, Vol. 179, p. 532.

18. *Structure and Optical Spectroscopy of Eu Doped Glass Ceramics Containing GdF3 Nanocrystals.* **D. Chen, Y. Wang, Y. Yu, et al.** 2008, Journal of Physical Chemistry C, Vol. 239, pp. 18943-18947.

19. *The luminescence and structure of novel transparent oxyfluoride glass-ceramics.* **Dejenka, M.J.** 1998, Journal of Non-Crystalline Solids, Vol. 239, p. 149.

20. *Scintillation from Eu2+ in nanocrystallized glass.* **J. Fu, M. Kobayashi, S. Sugimoto, et al.** 2009, Journal of the American Ceramic society, Vol. 92, p. 2119.

21. *Tb-doped Aluminosilicate Oxyfluoride Scintillating Glass and Glass-Ceramic.* **Z. Pan, K. James, Y. Cui, et al.** 2009, Materials Research Society Symposium Proceedings, Vol. 1164.

22. *Efficient radioluminescence of the Ce3+-doped Na-Gd phosphate glasses.* **M. Nikl, I. Nitsch, E. Mihokova, et al.** 2000, Applied Physics Letters, Vol. 77, pp. 2159-2161.

23. *Eu3+-activated heavy scintillating glasses.* **J. Fu, M. Kobayashi, S. Sugimoto, et al.** 2008, Material Research Bulletin, Vol. 43, pp. 1502-1508.

24. *New Transparent Virtoceramics Codoped with Er3+ and Yb3+ for Efficient Frequency Upconversion.* **Ohwaki, Y. Wang and J.** 1993, Applied Physics Letters, Vol. 63, p. 3268.

25. *Nanocrystallization in Fluorochlorozirconate Glass-Ceramics.* **C. Alvarez, Y. Liu, R. Leonard, et al.** 2013, Journal of the American Ceramic Society, Vol. 96, pp. 3617-3621.

26. *Comprehensive Rate Equation Analysis of Upconversion Luminescence Enhancement due to BaCl2 Nanocrystals in Neodymium-Doped Fluorozirconate-Based Glass-Ceramics.* **U. Skrzypczak, G. Pfau, G. Seifert, et al.** 2014, The Journal of Physical Chemistry C, Vol. 118, pp. 13087-13098.

27. *Photoluminescence and Microstructural Properties of SiO2-ZnO-B2O3 System containing TiO2 and V2O5.* **S. Oazyini, Z. Hamnabard, Z. Khalkhali, et al.** 2011, Ceramics International.

28. *Bi2O3-GeO2 Glass and Transparent Glass Ceramic Based on it.* **M. Voronchikhina, N. Goaschenko, V. Tsvetkov, et al.** 2011, Glass and Ceramics, Vol. 68, pp. 47-51.

29. **S. Cherry, J. Sorenson, M. Phelps.** *Physics in nuclear medicine.* 4th. s.l. : Elsevier, 2012.

30. *Detection efficiency of NaI(Tl) detector in 511-1332keV energy range.* **I. Akkurt, K. Gunoglu, S.S. Arda.** 2014, Sience and Technology of Nuclear Installations.

31. *Nanophase glass-ceramics.* **Pinckney., G. Beall and L.** 1999, Journal of the American Ceramic Society, Vol. 82, pp. 5-16.

32. *Scattering of visible light by glasses undergoing phase separation and homogenization.* **Andreev., N.** 1978, Journal of Non-Crystalline solids, Vol. 30, pp. 99-126.

33. *Stochastic theory of scattering from idealized spinodal structures: II scattering in general and for the basic late stage model.* **Hopper., R.** 1985, Journal of Non-Crystalline Solids, Vol. 70, pp. 111-142.

34. *Synthesis and Characterization of a BaGdF5:Tb Glass Ceramic as a Nanocomposite Scintillator for X-ray Imaging.* **G. Lee, C. Struebing, B. Wagner, et al.** 2016, Nanotechnology, Vol. 27, p. 8.

35. *New Large Grain, Highly Crystalline, Transparent Glass-Ceramics.* **T. Berthier, V. Fokin, E. Zanotto.** Journal of Non-Crystalline Solids : s.n., Vol. 354, pp. 1721-1730.

36. *Enhanced Quantum Yield of Yellow Photoluminescence of Dy3+ Ions in Nonlinear Optical Ba2TiSi2O8 Nanocrystals Formed in Glass.* **N. Maruyama, T. Honma, T. Komatsu.** 2009, Journal of Solid State Chemistry, Vol. 182, pp. 246-252.

37. *Effect of heat-treatment temperature on optical properties of Ba2TiSi2O8 nanocrystallized glasses."*. **Y. Takahashi, K. Kitamura, S. Inoue, et al.** 2005, Journal of the Ceramic Society of Japan, Vol. 113, pp. 419-423.

38. *Morphology and dispersion state of Ba2TiSi2O8 nanocrystals in transparent glass-ceramics and their nano-indentation behavior.* **K. Shinozaki, T. Honma, T. Komatsu.** 2012, Journal of Non-Crystalline Solids, Vol. 358, pp. 1863-1869.

39. *Elastic properties and and Vickers hardness of optically transparent glass-ceramics with fresnoite Ba2TiSi2O8 nanocrystals.* **K. Shinozaki, T. Honma, T. Komatsu.** 2011, Material Research Bulletin, Vol. 46, pp. 922-928.

40. *Elastic and mechanical properties of transparent nanocrystallized KNbGeO5 glass.* **F. Torres, K. Narita, Y. Benino, et al.** 2003, Journal of Applied Physics, Vol. 94, pp. 5265-5272.

41. *Radiation Hardness of Ce3+-doped Heavy Geramanate Glasses.* **S. Wang. G. Chen, S. Baccaro, et al.** 2003, Nuclear Instruments and Methods in Physics Research B, Vol. 486, pp. 475-479.

42. *Transmission Properties of Heavy-Germanate Glasses as Hosts for Scintillating Rare Earths.* **S. Baccaro, A. Cecilia, G. Chen, et al.** 2002, Nuclear Instruments and Methods in Physics Research A, Vol. 486, pp. 321-324.

43. *Photoluminescence decay curves: and analysis of the effects of flash duration and linear instrumental distortions.* **J.N. Demas, G.A. Crosby.** 1970, Analytical Chemistry, Vol. 42, pp. 1010-1017.

44. *Ceramic Scintillators.* **C. Greskovich, S. Duclos.** 1997, Annual Review of Materials Science, Vol. 27, pp. 69-88.

45. *Glass Scintillators for Prompt Detection of Intermediate Energy Neutrons.* **Egelstaff, P.A.** 4, 1957, Nuclear Instruments, Vol. 1, pp. 197-199.

46. **Chatterjee, A.K.** Handbook of Analytical Techniques in Concrete Science and Technology. 2001.

47. *Band-gap correlations in Bi4Ge3O12 amorphous and glass-ceramic materials.* **S. Polosan, A.C. Galca, and M. Secu.** 2011, Solid State Sciences, Vol. 13, pp. 49-53.

48. *Crystallization and spectroscopic properties of Eu-doped CaF2 nanocrystals in transparent oxyfluoride glass-ceramics.* **M. Secu, C.E. Secu, S. Polosan, et al.** 2009, Journal of Non-Crystalline Solids, Vol. 355, pp. 1869-1872.

49. *Novel Glass Ceramic Scintillator for Detection of Slow Neutrons in Well Logging Applications.* **A. Nikitin, A. Fedorov, M. Korjik.** 2013, IEEE Transactions on Nuclear Science, Vol. 60, p. 2.

50. *Silicate glass-based nanocomposite scintillators.* **M. Nikl, D. Niznansky, J. Ruzicka, et al.** 2011, Advances in Nanocomposite Technology.

51. *Nanoparticle-doped radioluminescent silica optical fibers.* **J. Mrazek, M. Nikl, I. Kasik, et al.** 2014, Proceedings of SPIE, Vol. 9228, p. 922805.

52. *Glass formation of rare earth aluminates by containerless processing.* **Y. Watanabe, A. Masuno, and H. Inoue.** 2012, Journal of Non-Crystalline Solids, Vol. 358, pp. 3563-3566.

53. *Structure of glassy and metastable crystalline BaTi2O5 fabricated using containerless processing.* **J. Yu, S. Yoda, A. Masuno, et al.** 2010, Ferroelectrics, Vol. 402, pp. 130-136.

54. *New lutetium silicate scintillators.* **E. Bescher, S.R. Robson, and J.D. Mackenzie.** 2000, Journal of Sol-Gel Science and Technology, Vol. 19, pp. 325-328.

55. *Terbium Activated Heavy Scintillating Glasses.* **J. Fu, M. Kobayashi, J. Parker.** 2008, Journal of Luminescence, Vol. 128, pp. 99-104.

56. *Energy transfer based emission analysis of Eu3+ doped Gd2O3-CaO-SiO2-B2O3 glasses for laser and X-rays detection material applications.* **N. Wantana, E. Kaewnuam, B. Damdee, et al.** 2018, Journal of Luminescence, Vol. 194, pp. 75-81.

57. *Luminescence properties of Gd3+-doped borosilicate scintillating glass.* **C. Tang, S. Liu, L. Liu, et al.** 2015, Journal of Luminescence, Vol. 160, pp. 317-320.

58. *Temperature-dependent non-radiative energy transfer from Gd3+ to Ce3+ ions in co-doped LuAG:Ce, Gd garnet scintillators.* **Z. Onderisinova, M. Kucera, M. Hanus, et al.** 2015, Journal of Luminescence, Vol. 167, pp. 106-113.

59. *Spectroscopic Properties of Sm3+-Doped Lanthanum Borogermanate Glass.* **R. Rajaramakrishna, B. Knorr, V. Dierolf, et al.** 2014, Journal of Luminescence, Vol. 156, pp. 192-198.

60. *Novel Phosphors of Eu3+, Tb3+, or Tm3+ activated LaBGeO5.* **S. Zhang, G.H. Wu, C.J. Duan, et al.** 2011, Journal of Rare Earths, Vol. 29, pp. 737-740.

61. *Luminescence processes in the crystalline and glass modifications of LnBGeO5-type compositions.* **J.W.M. Verwey, D. Van Der Voort, G.J. Dirksen, et al.** 1990, Journal of Solid State Chemistry, Vol. 89, pp. 106-117.

62. *Enhanced Tb3+ luminescence by non-radiative energy transfer from Gd3+ in silicate glass.* **X.Y. Sun, S.M. Huang, M. Gu et al.** 2010, Physics B, Vol. 405, pp. 569-572.

63. *Nano-crystallization and highly oriented crystal line paterning of Sm3+-doped Bi2GeO5 and Bi4Ge3O12 in bismuth germanate-based glasses.* **C. Yang, K. Shinozaki, T. Honma, et al.** 2017, Journal of Non-Crystalline Solids, Vol. 459, pp. 116-122.

64. *Optical and scintillation properties of 30BaO-(70-x)TiO2-xGeO2 (x=50, 55, 60) glass-ceramics.* **T. Yanagida, H. Masai, G. Okada, et al.** 2018, Journal of Non-Crystalline Solids, Vol. 501, pp. 106-110.

65. *Terbium-activated lithium-lanthanum-aluminosilicate oxyfluoride scintillating glass and glass-ceramic.* **Z. Pan, K. James, Y. Cui, et al.** 2008, Nuclear Instruments and Methods in Physics Research A, Vol. 594, pp. 215-219.

66. *Intense ultraviolet emission from Tb3+ and Yb3+ codoped glass ceramic containing CaF2 nanocrystals.* **L. Huang, T. Yamashita, R. Jose, et al.** 2007, Applied Physics Letters, Vol. 90, p. 13116.

67. *Photoluminescence of Sm3+, Dy3+, and Tm3+-doped transparent glass ceramics containing CaF2 nanocrystals.* **G. Lakshminarayana, R. Yang, M. Mao, et al.** 2009, Journal of Non-Crystalline Solids, Vol. 355, pp. 2668-2673.

68. *Eu2+/Dy3+co-doped white light emission glass ceramics under UV light excitation.* **R. Ye, Z. Cui, Y. Hua, et al.** 2011, Journal of Non-Crystalline Solids, Vol. 357, p. 2282.

69. *New transparent glass-ceramics containing large grain Eu3+:CaF2 nanocrystals.* **J. Cheng, W. Deng.** 2012, Materials Letters, Vol. 73, p. 112.

70. *Tb3+-activated SiO2-Al2O3-CaO-CaF2 oxyfluoride scintillating glass ceramics.* **Huang., X. Sun and S.** 2010, Nuclear Instruments and Methods in Physics Research A, Vol. 621, pp. 1-3.

71. *Crystallization and spectroscopic properties investigations of Er3+ doped transparent glass ceramics containing CaF2.* **Z. Hu, Y. Wang, E. Ma, et al.** 2006, Materials Research Bulletin, Vol. 41, p. 217.

72. *Photostimulated luminescence from a fluorobromozirconate glass-ceramic and the effect of crystallite size and phase.* **M. Secu, S. Schweizer, J.M. Spaeth, et al.** 2003, Journal of Physics: Condensed Matter, Vol. 15, p. 1097.

73. *Site selection spectroscopy in Eu3+-doped lanthanum fluorozirconate glass and glass-ceramic.* **O. Maalej, M. El Jouad, N. Gaumer, et al.** 2015, Journal of Non-Crystalline Solids, Vol. 420, pp. 48-54.

74. *Fluorozirconate-based glass ceramic X-ray detectors for digital radiography.* **Johnson., S. Schweizer and J.** 2007, Radiation Measurements, Vol. 42, pp. 632-637.

75. *Photostimulated luminescence in a rare earth-doped fluorobromozirconate glass ceramic.* **A. Edgar, J.M. Spaeth, S. Schweizer, et al.** 1999, Applied Physics Letters, Vol. 75, pp. 2386-2388.

76. *"Radiation defects in Ce3+-activated fluorobromozirconate glass-ceramic X-ray storage phosphors."*. **M. Secu, S. Schweizer, U. Rogulis, et al.** 2003, Radiation Measurements, Vol. 38, pp. 739-742.

77. *Photoluminescent properties of nanocrystallized zinc borosilicate glasses."*. **G. Chen, M. Nikl, N. Solovieva, et al.** 2004, Radiation Measurements , Vol. 38, pp. 771-774.

78. *Photo- and radioluminescence of ZnO-precipitated glass-ceramics.* **H. Masai, T. Yanagida, and T. Fujiwara.** 2014, Sensors and Materials , Vol. 27, pp. 237-245.

79. *Scintillation and dosimeter properties of LiAlSi2O6 and LiAlSi4O10 crystals.* **T. Yanagida, Y. Fujimoto, M. Koshizumi, et al.** 2017, Sensors and Materials , Vol. 29, pp. 1399-1406.

80. *A Novel Inorganic Scintillator: Lu2Si2Oy:Ce3+ (LPS).* **D. Pauwels, N. Le Masson, B. Viana, et al.** 2000, IEEE Transactions on Nuclear Science, Vol. 47, pp. 1787-1790.

81. *Variation of luminescence properties of Na2O-CaO-SiO2:Nd3+ glass with crystallinity.* **J. Li, Y.Z. Mei, C. Gao, et al.** 2011, Journal of Non-crystalline Solids, Vol. 357, pp. 1736-1740.

82. *Study of the glass and glass-ceramic stoichiometric and Gd3+ heavy loade BaO*2SiO2:Ce (DSB:Ce) scintillation materials for calorimetry application.* **R. Novotny, K.T. Brinkmann, a. Borisevich, et al.** 2015.

83. *A New Ceramic Scintillator for Neutron Detection: CaF2:Eu2+/6LiF.* **J. Glodo, H. Lingertat, C. Brecher, et al.** 2005, IEEE Nuclear Science Symposium Conference Record, Vols. N6-4, p. 112.

84. *Scintillation from Eu2+ in nanocrystallized glass.* **M. Kobayashi, S. Sugimoto.** 2009, Journal of the American Ceramic Society, Vol. 92.

85. *On the solubility of LnF3 in lanthanum fluoride.* **O.V. Kudryavteseva, L.S. Garashina, K.K. Rivkina, et al.** 1974, Sov. Phys. Crystallogr., Vol. 48, p. 531.

86. *Spontaneous emission probabilities and quantum efficiencies for excited states of Pr3+ in LaF3.* **Weber, M.J.** 1968, Journal of Chemical Physics, Vol. 48, pp. 4774-4780.

87. *Polymer and glass-matrix nanocomposites for scintillation applications.* **Z. Kang, B. Wagner, C. Summers, et al.** 2012, IEEE Nuclear Science Symposium and Medical Imaging Conference Record, pp. 1688-1691.

88. *Enhanced luminescent properties of Tb3+ ions in transparent glass ceramics containing BaGdF5 nanocrystals.* **S. Huang, M. Gu.** 2012, Journal of Non-Crystalline Solids, Vol. 358, pp. 77-80.

89. *Luminescence and energy transfer in BaGdF5.* **E. Banks, M.T. Sobieraj, S.K. Ruan, et al.** 1988, Journal of Luminescence, Vol. 40, pp. 659-660.

90. *Structure and neutron imaging characteristics of lithium borate-barium chloride glass-ceramics.* **G.A. Appleby, A. Edgar, G.V.M. Williams, et al.** 2006, Nuclear Instruments & Methods in Physics Research A, Vol. 564, pp. 424-430.

91. *Optical Investigation of Ce3+-activated Borogermanate Glass Induced by Substitution of BaF2 for BaO.* **X.Y. Sun, Y. Yuan, Z.H. Xiao, et al.** 2015, Journal of the American Ceramic Society, Vol. 98, pp. 3655-3658.

92. *A neutron scintillator based on transparent nanocrystalline CaF2:Eu glass ceramic.* **C. Struebing, J. Chong, G. Lee, et al.** 2016, Applied Physics Letters, Vol. 108, p. 153106.

93. *Structural and Spectroscopic Properties of Some Neodymium-Borogermanate Glasses and Glass Ceramics Embedded with Silver Nanoparticles.* **L. Bolundut, L. Pop, M. Bosca, et al.** 2017, Ceramics International, Vol. 43, pp. 12232-12238.

94. *Luminescence properties of B2O3-GeO2-Gd2O3 scintillating glass doped with rare-earth and transition-metal ions.* **X.Y. Sun, D.G. Jiang, W.F. Wang, et al.** 2008, Nuclear Instruments and Methods in Physics Research A, Vol. 182, pp. 1721-1730.

95. *Luminescent properties of Tb3+-activated B2O3-GeO2-Gd2O3 scintillating glasses.* **X.Y. Sun, X.G. Yu, W.F. Wang, et al.** 2013, Journal of Non-Crystalline Solids, Vol. 379, pp. 127-130.

96. *5D3-5D4 cross-relaxation of Tb3+ in a cubic host lattice.* **C.K. Duan, C.C. Ko, G. Jia, et al.** 2011, Chemistry and Physics Letters, Vol. 506, pp. 179-182.

97. *Excitation mechanisms of green emission from terbium ions embedded inside the sol-gel films deposited onto nano-porous substrates.* **A. Pohorodecki, N.V. Gaponenko, M. Banski, et al.** 2010, ECS Transmissions, Vol. 28, pp. 81-88.

98. *Concentration dependence of UV and electron-excited Tb3+ luminescence in Y3Al5O12.* **W.F. Weg, J.A. Popna, A.T. Vink.** 1985, Journal of Applied Physics , Vol. 57, pp. 5450-5456.

99. *Luminescence and energy transfer properties of Gd3+ and Tb3+ in LaAlGe2O7.* **Y.C. Li, Y.H. Chang, Y.S. Chang et al.** 2007, Journal of Physical ChemistryC, Vol. 111, pp. 10682-10688.

100. *Photoluminescence of Eu3+, Tb3+, Dy3+, and Tm3+-doped transparent GeO2-TiO2-K2O glass ceramics.* **G. Lakshminarayana, J. Qiu, M.G. Brik et al.** 2008, Journal of Physics Condensed Matter, Vol. 20, pp. 1-11.

101. *Novel phosphors of Eu3+, Tb3+, or Bi3+ activated Gd2GeO5.* **P. Guo, F. Zhao, G. Li et al.** 2003, Journal of Luminescence, Vol. 105, pp. 61-67.

102. *Composition effects on optical properties of Tb3+-doped heavy germanate glasses.* **G. Chen, Y. Yang, D. Zhao et al.** 2005, Journal of the American Ceramic Society, Vol. 88, pp. 293-296.

103. *Synthesis and luminescence properties of Tb doped LaBGeO5 and GdBGeO5 glass scintillators.* **C. Struebing, G. Lee, B. Wagner, Z. Kang.** 2016, Journal of Alloys and Compounds, Vol. 686, pp. 9-14.

104. *Absorption intensities and emission cross-sections of Tb3+ (4F8) in TbAlO3.* **D. Sardar, K. Nash, R.M. Yow et al.** 2006, Journal of Applied Physics, Vol. 100, pp. 1-5.

105. *Local laser induced crystallization of lanthanum boron germanate glass near LaBGeO5 composition.* **S.V. Lotarev, T.O. Gelmenova, Y.S. Priseko et al.** 2011, Proceedings SPIE, pp. 1-9.

106. *Structural evolution of LaBGeO5 transparent ferroelectric nano-composites.* **P. Gupta, H. Jain, D.B. Williams et al.** 2004, Journal of Noncrystalline Solids, Vol. 349, pp. 291-298.

107. *Structure and crystallization specifics of alumina-bearing lanthanide borogermanate glass.* **V.N. Sigaev, E.V. Orlova, S.V. Lotarev et al.** 2006, Glass Ceramics, Vol. 63, pp. 184-189.

108. *Influence of alumina addition on crystallization and texturing behavior of LaBGeO5 glass.* **V.N. Sigaev, P. Pernice, A. Aronne, et al.** 2006, Journal of Noncrystalline solids, Vol. 352, pp. 2123-2128.

109. *High light yield Ce3+-doped dense scintillating glasses.* **Q. Wang, B. Yang, Y. Zhang, et al.** 2013, Journal of Alloys and Compound, Vol. 581, pp. 801-804.

110. *Optical properties of Ce3+ doped fluorophosphates scintillation glasses.* **Y. Yao, L. Liu, Y. Zhang, et al.** 2016, Optical Materials, Vol. 51, pp. 94-97.

111. *Systematic Behavios in Trivalent Lanthanide Charge Transfer Energies.* **Dorenbos, P.** 2003, Journal of Physics: Condensed Matter, Vol. 15, pp. 8417-8434.

112. *Optical-absorption and Photoionization Measurements from the Excited States of Ce3+:Y3Al5O12.* **D.S. Hamilton, S.K. Gayen, G.J. Pogatshnik, et al.** 1989, Physics Review B: Condensed Matter, Vol. 39, pp. 8807-8815.

113. *Doping Effects in Amorphous Oxides.* **F. Funabiki, T. Kamiya, H. Honso.** 2012, Journal of the Ceramic Society of Japan, Vol. 15, pp. 447-457.

114. *Optical and scintillation properties of pure and Ce3+ doped GdBr3.* **EVD van Loef, P. Dorenbos, CWE van Eijik, et al.** 2001, Optical Communications, Vol. 189, pp. 297-304.

115. *Optimization of a gadolinium-rich oxyhalide glass scintillator for gamma ray spectroscopy.* **C. Struebing, B. Beckert, J. Nadler, et al.** 2017, Journal of the American Ceramic Society, pp. 1-6.

116. *Floating zone growth and scintillation characteristics of cerium-doped gadolinium pyrosilicate single crystals.* **S. Kawamura, J.H. Kaneko, M. Higuchi, et al.** 2007, IEEE Transmissions on Nuclear Science, Vol. 54, pp. 1383-1386.

117. *"New transparent vitroceramics codoped with Er3+ and Yb3+ for efficient frequency upconverison.".* **Ohwaki., Y. Wang and J.** 1993, Applied Physics Letters, Vol. 63, p. 3268.

118. *"Terbium-activated lithium-lanthanum-aluminosilicate oxyfluoride scintillating glass and glass-ceramic.".* **Z. Pan, K. James, Y. Cui, et al.** 2008, Nuclear Instruments and Methods in Physics Research A, Vol. 594, pp. 215-219.